2018

MAGNETLESS AND TOPOLOGICAL EDGE MODE-BASED ON-CHIP ISOLATORS AND SPIN-ORBIT COUPLING IN MAGNETO-OPTIC MEDIA

Dolendra Karki
Michigan Technological University, dkarki@mtu.edu

MAGNETLESS AND TOPOLOGICAL EDGE MODE-BASED ON-CHIP ISOLATORS AND SPIN-ORBIT COUPLING IN MAGNETO-OPTIC MEDIA

By

Dolendra Karki

A DISSERTATION

Submitted in partial fulfillment of the requirements for the degree of

DOCTOR OF PHILOSOPHY

In Physics

MICHIGAN TECHNOLOGICAL UNIVERSITY

2018

This dissertation has been approved in partial fulfillment of the requirements for the Degree of DOCTOR OF PHILOSOPHY in Physics.

Department of Physics

Dissertation advisor:	*Dr. Miguel Levy*
Committee Member:	*Dr. Ramy El-Ganainy*
Committee Member:	*Dr. John Jaszczak*
Committee Member:	*Dr. Durdu O. Guney*
Department Chair:	*Dr. Ravindra Pandey*

Dedication

To my mother

Contents

List of Figures

List of Tables

Preface

The present dissertation is based on my PhD research work in Physics conducted during the period of Fall 2012 - Fall 2018 at the Michigan Technological University. This preface serves as an explanation of my contribution to the work that makes the main body of the chapters 2, 3 and 4. The research studies in chapter 2 and 4 include, in part, text and images published in the following peer-reviewed journal articles 1 and 2 where as chapter 3 includes the content from the submitted article 3 which is under review.

1. **D. Karki**, V. Stenger, A. Polick, M. Levy, *"Thin-Film Magnet-less Faraday Rotators For Compact Heterogeneous Integrated Isolator"*, Journal of Applied Physics 121, 233101 (2017).

2. M. Levy, **D. Karki**, *"Nonreciprocal Transverse Photonic Spin and Magnetization-Induced Electromagnetic Spin-Orbit Couplin"*, Scientific Reports 7, 39972 (2017).

3. **D. Karki**, R. El-Gananiny, M. Levy, *"Towards High Performing Edge-State Optical Isolator"*, manuscript submitted- under review.

I (Dolendra Karki) have co-authored all the three articles listed above published or

under review. I have the necessary copyright permission from author/publisher (see appendix for detail) to reproduce, text and images, from the above listed journal articles in the present dissertation titled: "MAGNETLESS AND TOPOLOGICAL EDGE MODE-BASED ON-CHIP ISOLATORS AND SPIN-ORBIT COUPLING IN MAGNETO-OPTIC MEDIA".

The work published in Journal of Applied Physics (Publication 1) on magnetless optical isolator is the result of our collaboration with Srico Inc., Columbus, OH. My contribution was characterization/measurements of all the devices and the fabrication of thin film by lapping. Dr. Vince Stenger and Dr. Andrea Pollick from Srico Inc. carried out the crystal-ion slicing method of fabrication of thin film , transfer to Si substrate, and also adhesive bonding with PolarCor polarizers.

The work in Chapter 3 of the dissertation is based on the experimental results obtained on topological SSH-model based waveguide arrays on LPE grown BiLuIG films on GGG substrates. My contribution was design , fabrication and characterization of the devices that produced the results.

Chapter 4 includes the theoretical study of non-reciprocal spin orbit coupling in magneto-optic media. My contribution was to perform numerical calculations and analysis using the equations derived by Prof. Miguel Levy.

Acknowledgments

I would like to express my utmost sincere gratitude to Professor Miguel Levy for this opportunity to purse my PhD research under his supervision. I am thankful for his continuous support, guidance and encouragement throughout my PhD career. Thank you for always being available to help me whenever i was in need. I will forever be indebted to you for all you have taught and mentored in honing my skills and knowledge in experimental physics world. I would also like to thank Mrs. Anita Levy for treating us like the part of a family.

I can't thank enough to my mother who not only gave birth but also sacrificed a lot to support my education since childhood to this day. Without her dedication, and encouragement, i would not have come this far. I am forever thankful to my mother for everything.

The best thing that happened to me during my PhD study was that i was married with my beautiful, loving and caring wife Jyotshma Dhakal. I should say thank you to my dear wife for understanding me, never complaining when i showed up late from work, and always caring for me.

My work would not have been successful without the collaboration with Dr. Sri Sriram, Dr. Vince Stenger, Dr. Andrea Pollick from SRICO Inc, Columbus, OH. I am grateful to Dr. Sriram for his gracious support and encouragement to present our collaborative work in CLEO conference and being so kind towards me and my wife.

Thank you Dr. Stenger, and Dr. Pollick for this wonderful experience of working with you and learning from you in our joint project on magnet-less optical isolator.

I am also thankful to Prof. Ravindra Pandey, Prof Jacek Borysow, all faculty and staff in Dept. of Physics and MTU for supporting my stay, study and research over the years of my PhD career.

I would take this opportunity to thank my advisory committee members Prof. Ramy El-Ganainy, Prof. John Jaszczak and Prof. Durdu Guney for constructive feedback, criticism, valuable suggestions, and the motivation for my academic growth. Specifically, thanks to Prof. El-Ganainy for fruitful discussions and answers of my questions on theoretical aspect of the topological isolator work and beyond, Prof. Jaszczak for so thoroughly going through my thesis and pointing out the errors and suggesting me corrections from which i also learned some important aspects of the writing, and Prof. Guney for helping me to learn COMSOL. introducing me on magneto-optic metamaterial through our collaborative work and advising on my research and dissertation.

I would also like to thank my senior colleague and friend, Dr. Ashim Chakravarty who introduced and trained me on many experimental methods, tools, and optical measurements. My friend and classmate Dr. Niraj Dhital who helped me learn c-programming that was very useful for my theoretical work and numerical calculations during my research.

I would also like to acknowledge help from Mr. Owen Mills, Dr. Ed Laitila for training and helping me to use SEM,FIB, TEM, XRD, etc., characterization tools. I have benefited from Many fruitful discussions, training and help from Dr. Chito Kendrick during fabrication of the devices for my research work. Without the help from Kevin Roberts of 'Minnesota Nano-Cener' in Univ. of Minnesota, the e-beam lithography fabrication of the SSH edge mode-based waveguide arrays work would not have been possible. I really appreciate for his expertise guidance and friendliness throughout the optimization and fabrication processes of the devices during my visit to Minnensota nano-center facility.

Last but not the least, i would like to thank all of my friends for accompanying me, my relatives and all of my teachers for inspiring and supporting me to achieve this goal of my life.

List of Abbreviations

MO	Magneto-Optic
FR	Faraday Rotation/Rotator
TM	Transverse Magnetic
TE	Transverse Electric
ER	Extinction Ratio
IL	Insertion Loss
YIG	Yttrium Iron Garnet ($Y_3Fe_5O_{12}$)
Bi:YIG	Bismuth-substituted Yttrium Iron Garnet ($Bi_xY_{3-x}Fe_5O_{12}$)
Bi:LuIG	Bismuth-substituted Lutetium Iron Garnet ($Bi_1Lu_2Fe_{4.3}Ga_{0.7}O_{12}$)
Ce:YIG	Cerium-substituted Yttrium Iron Garnet ($Ce_xY_{3-x}Fe_5O_{12}$)
CMZ:GGG	Calcium Magnesium and Zirconium Substituted GGG
	$[Gd_{2.68}Ca_{0.32}][Ga_{1.04}Mg_{0.32}Zr_{0.64}]Ga_3O_{12}$
GGG	Gadolinium Gallium Garnet ($Gd_3Ga_5O_{12}$)
RIG	Rare-Earth Iron Garnets
BCB	Benzocyclobutene
FW	Forward
BW	Backward
NRPS	Nonreciprocal Phase Shift

NRMC	Non-reciprocal Mode Conversion
QPM	Quasi Phase Matching
MZI	Mach-Zehnder Interferometer
SEM	Scanning Electron Microscope
SOI	Silicon-On-Insulator
LPE	Liquid Phase Epitaxy
Eq.	Equation
Fig.	Figure
IR	Infrared
NIR	Near Infrared
MOI	Magneto-Optic Isolator
PLD	Pulsed Laser Deposition
SSH	Su-Schrieffer Heeger
OAM	Orbital Angular Momentum
SAM	Spin Angular Momentum

Abstract

The rapid growth of optical communication networks requires monolithic integration of various optical components such as lasers, modulators, detectors, amplifiers etc. Optical feedback due to reflected light at the interfaces of several components in a photonic circuit has detrimental effects to the normal operation of the lasers by increasing noise, forcing the lasers to oscillate into different lasing modes etc. So optical isolators are crucial components to make complex optical circuits possible by preventing the reflected signal from coupling back to the laser sources. For this purpose, an optical isolator that can produce isolation of the feedback signal by > 30 dB, and at the same time offers very low insertion loss of < 1 dB is desired. Only bulk magneto-optic Faraday rotator-based optical isolators that need biasing magnets deliver such a performance but are not compatible with integrated circuits. Here we present biasing magnet free thin film optical isolator with ≥ 30 dB of isolation and < 0.5 dB insertion loss, and also demonstrate progress towards their integration into semiconductor substrate platforms.

In the quest for on-chip optical isolators, we also discuss the results of experimentation on a novel physical phenomenon of topological edge-mode-based optical isolation and localization of the edge mode in a single waveguide in a device of multiple coupled waveguides. The device is fabricated on liquid-phase-epitaxy-grown bismuth-substituted lutetium iron garnet films (Bi:LuIG) on a gadolinium gallium garnet

(GGG) substrate. The localization of the field in a single channel for forward propagating light and delocalization of the field for reflected light serves the purpose of an optical isolator with predicted isolation as high as -50 dB. Localization of power as high as 29 dB in a single channel as compared to the power in outermost channel and average insertion losses of < 2 dB in the edge channel relative to total output power in the whole array are measured has been found. The challenges and methods for implementation of SSH-topology-based optical isolators have also been analyzed. Moreover, the formulation of electromagnetic spin-orbit coupling in magneto-optic media as an alternative source of spin-orbit coupling to non-paraxial optical vortices is also presented in this dissertation. It shows that magnetization-induced electromagnetic spin-orbit coupling is possible, and that it leads to unequal spin-orbital angular momentum conversion in magneto-optic media evanescent waves in opposite propagation-directions. Generation of free-space helicoidal beams based on this conversion is shown to be spin-helicity- and magnetization-dependent. We show that transverse-spin to orbital angular momentum coupling into magneto-optic waveguide media engenders spin-helicity-dependent unidirectional propagation. This unidirectional effect produces different orbital angular momenta in opposite directions upon excitation-spin-helicity reversals.

Chapter 1

Introduction

Optical fiber communication is an integral part of modern communication system for it not only serves as an interconnection between processed and stored data in electronic system hundreds of kilometers away, but also offers high speed capacity and efficiency in data transport. Many of the components of the interconnect have been successfully developed or integrated to the semiconductor platform such as Ge-lasers [1], Si and Si_3N_4 waveguides [2, 3], Si modulators [4], optical amplifiers [5],optical multiplexers [6],and optical resonator filters [7]. However non-reciprocal device components such as optical isolators and circulators are still posing issues over the successful integration with almost all devices lacking either the isolation ratio below requirement of at least 30 dB or having losses more than desired range of within 1 dB. Non-reciprocal devices use mainly magneto-optic garnets materials

because of their high transparency and Faraday rotation in near-infrared wavelengths that are used in telecommunication. Its non-reciprocal effect enables it to isolate the reflected light from coupling back to the laser source or other components of the optical integrated circuits (OICs). After the first discovery of basic magnetic garnet material YIG ($Y_3Fe_5O_{12}$) in 1957 at Bell labs, considerable research has being conducted over the last couple of decades on both materials advancement and the device designs. In particular, bismuth and cerium substituted YIG material and devices based on these materials, to significantly increase the Faraday rotation and thereby the device length has been widely investigated [8–17]. As a result, remarkable improvement has been achieved on material advancement from Ce-substituted YIG on GGG with the highest reported Faraday rotation of 4800^0 per cm [11] to achieving single-domain bias magnet-free material [18, 19].

Most of the work devoted to the development of compact on-chip isolators has focused on the design and fabrication of optical waveguide structures, such as Faraday rotators [20–22], Mach-Zehnder interferometers [23–25], ring resonators [26, 27] , and other variants [28–30]. However, the remaining issue of reducing the size or eliminating the magnetizing element, be it permanent magnets or electromagnets, has not been addressed extensively [22, 31, 32]. In fact, it is the magnetizing element that accounts for a considerable part of the bulk of these devices at present. Prior work by Levy et al. has addressed the integration of permanent magnet films in Faraday rotator waveguide structures [22, 31], nevertheless, no work has been

reported on the complete elimination of the magnetizing elements in micron-scale magneto-optic devices. Chapter 2 of this dissertation encompasses the fabrication, characterization and wafer bonding techniques to integrate the components of magnetless magneto-optic (MO) material to develop fully functional optical isolator and its integration to Si platform.

Aside from the Faraday-rotation-based optical isolators and wafer-bonding integration for on-chip isolation in optical circuits, the waveguide-structure-based optical isolator is another approach to realize on-chip devices. The issue with the waveguide-geometry-based isolator device is that because of the longitudinal component of the field in waveguide modes, the inevitable coupling of longitudinal and transverse components leads to birefringence between TE and TM modes and prevents full 45^0 polarization as in bulk Farady rotators. The birefringence may arise from different anisotropies in the structure such as geometry, stress and growth related phenomena, and a fine tuning is needed to zero out linear birefringence [20, 21, 33–35]. Since this takes tedious and costly processes and in many cases is not compatible with integrated device operations, researchers have moved to alternatives of utilizing non-reciprocal phase shift (NRPS) effect based devices such as MZIs [23–25, 36], and Bloch oscillators [37]. A new concept of topological-edge-mode based optical isolator has been recently purposed by Ganainy et al. [38] with prediction of about 50 dB of isolation. Topological concept-based devices are particularly

robust against the perturbation that could arise from fabrication tolerances during device making. This new concept-based experimentation on waveguide arrays of liquid-phase-epitaxy (LPE)-grown bismuth-substituted lutetium iron garnet films are presented in chapter 3 of this thesis.

Chapter 4 discusses the generation of optical orbital angular momenta induced through magneto-optic spin-orbit coupling. It analyzes the effect of non-reciprocity on spin-induced transverse optical momenta, as well as magnetization tuning and magnetization reversal effects on unidirectionally spin-induced orbital angular momenta normal to the optical spin. Finally, chapter 5 draws the conclusions of the work and make suggestions for future work.

Chapter 2

Magnetless Faraday rotators for compact integrated optical isolators

2.1 Introduction

[1]The miniaturization of optical isolators and circulators has been actively pursued over the last several decades [39, 40]. This effort has been spurred by a widespread industrial need, particularly in optical telecommunications, to protect laser sources

[1]Part of the material contained in this chapter has been published in *Journal of applied physics*, 121 (2017) [58] and reprinted here with permission. (see appendix B for permission).

from return light and back reflections in optical circuits [39, 40]. Driving factors for this undertaking include the expected robustness of integrated circuits, improved functional reliability, batch fabrication economy, improved optical alignment and immunity to vibrations.

Magneto-optic (MO) methodologies to on-chip isolation have received considerable attention because of the nonreciprocal nature of the Faraday effect and the magneto-optic nonreciprocal phase-shift effect [39, 40]. Both these techniques require the application of a magnetic field to saturate the magnetization in the device. Magneto-optic garnet materials, most notably bismuth- and cerium-substituted iron garnets have been used in on-chip prototypes. These are also the materials of choice and are extensively used in bulk isolators presently sold commercially.

Most of the work devoted to the development of compact on-chip isolators has focused on the design and fabrication of optical waveguide structures, such as Faraday rotators [20–22], Mach-Zehnder interferometers [23–25], ring resonators [26, 27], and other variants [28–30]. But the remaining issue of reducing the size or eliminating the magnetizing element, be it permanent magnets or electromagnets, has not been addressed extensively [22, 31, 32]. In fact, it is the magnetizing element that accounts for a considerable part of the bulk of these devices at present. Prior work by Levy et al. has addressed the integration of permanent magnet films in Faraday rotator waveguide structures [22, 31]. However no work has been reported on the complete

elimination of the magnetizing element in micron-scale magneto-optic devices. It is this question that is investigated in this work starting with magnetless MO bulk film and making thin film planar waveguide structure by lapping to crystal-ion slicing and integrating it with two ultra thin PolarCor polarizers.

2.2 Principle of magneto-optical isolator based on the Faraday effect

2.2.1 Faraday Rotation

The Faraday effect in magneto-optics is the phenomenon of rotation of polarization of linearly polarized light in presence of a static magnetic field applied along the direction of light propagation direction. Any linearly polarized light can be considered as the superposition of two normal modes namely Right Circularly Polarized (RCP) and Left Circularly Polarized (LCP) components with equal amplitudes [41, 42]. In Jones-vector representation, for any linearly polarized light at an angle θ to the horizontal direction [42], and the amplitude components are given as,

$$\begin{bmatrix} \cos\theta \\ \sin\theta \end{bmatrix} = \frac{1}{2}e^{-i\theta}\begin{bmatrix} 1 \\ i \end{bmatrix} + \frac{1}{2}e^{i\theta}\begin{bmatrix} 1 \\ -i \end{bmatrix} \tag{2.1}$$

where column vector on left hand side represents the Jones vector for linearly polarized light at angle θ and two column vectors on right hand sides represent RCP and LCP light respectively. RCP and LCP light propagate with different velocities c/n_+ and c/n_- in magneto-optic materials with different refractive indices n_+ and n_- and different phase shifts ϕ_+ and ϕ_- after passing through the same thickness of the material respectively. For a length of l along the propagation direction, the relative phase shift is given as:

$$\Delta\phi = \phi_+ - \phi_- = \frac{2\pi}{\lambda}\left(n_+ - n_-\right) l \tag{2.2}$$

The resulting Jones vector of the beam emerging out of the magneto-optic material is:

$$\frac{1}{2}e^{-i\theta}e^{i\phi_+}\begin{bmatrix}1\\ i\end{bmatrix} + \frac{1}{2}e^{i\theta}e^{i\phi_-}\begin{bmatrix}1\\ -i\end{bmatrix} = e^{-i\phi_0}\begin{bmatrix}\cos\left(\theta - \Delta\phi/2\right)\\ \sin\left(\theta - \Delta\phi/2\right)\end{bmatrix} \tag{2.3}$$

where $\phi_0 = \left(\phi_+ + \phi_-\right)/2$ is the average of absolute phase gained by RCP and LCP light while passing through the material. The Jones vector of (2.3) clearly indicates that the emerging light is linearly polarized and the polarization vector is further rotated by half of the phase $(\Delta\phi/2)$ shift between two modes. The output light from the material will be linearly polarized provided the refractive indices n_+ and n_- are purely real with no imaginary part. For the material, absorbing RCP and LCP light, the indices of refraction are given as $n_+ \longrightarrow n_+ + ik_+$ and $n_+ \longrightarrow n_- + ik_-$ with k_+ and k_- being the imaginary parts that are related to the absorption. The difference in

absorption coefficient is what is known as circular dichroism. Because of the different amount of absorption for RCP and LCP light, the amplitudes of the two modes is no longer equal resulting in elliptically polarized normal modes. The final output of the beam will be rotated elliptical polarization. Most commonly used magneto-optic iron garnet materials are highly transparent at infra-red (IR) wavelength range with negligible effect due to loss. However linear birefringence induced by geometry, stress or growth related anisotropy may cause detrimental effects, especially to magneto-optic waveguide-based devices, which require phase matching between Transverse elctric (TE) to transverse magnetic (TM) mode conversion.

2.2.2 Reciprocal and non-reciprocal polarization rotation

In an optically active material with intrinsic helical structure such as tellurium oxide(TeO_2), quartz (α-SiO_2), cinnabar(HgS), amino acids and sugars, the material equation is propagation-direction(k)dependent and is given as:

$$\vec{D} = \hat{\epsilon}\vec{E} + i\epsilon_0 \left(\vec{\mathrm{g}} \times \vec{E}\right) \tag{2.4}$$

where $\vec{E}$ and $\vec{D}$ are the electric field and displacement vectors, $\hat{\epsilon}$ is the dielectric permitivity tensor of the medium, ϵ_0 is the permitivity in free space and $\vec{\mathrm{g}}$ is a pseudovector called gyration vector, which is propagation-direction dependent, i.e. $\mathrm{g}(\vec{k}) = -\mathrm{g}(-\vec{k})$.

So reversal of the propagation direction of the light beam also reverses the sense of the rotation of polarization in these materials, and the rotation is reciprocal in that sense. For the beam propagating in the $\hat{z}$ direction so that $\vec{k} = (0, 0, k)$ and $\vec{\mathrm{g}} = (0, 0, g)$, the above equation (2.4) can be written as

$$\vec{D} = \hat{\epsilon}\vec{E} \tag{2.5}$$

The permitivity tensor now becomes asymmetric with off-diagonal terms and is given as [43]

$$\hat{\boldsymbol{\epsilon}} = \begin{pmatrix} \epsilon_{xx} & i\mathrm{g} & 0 \\ -i\mathrm{g} & \epsilon_{yy} & 0 \\ 0 & 0 & \epsilon_{zz} \end{pmatrix} \tag{2.6}$$

where $\epsilon_{xx} = \epsilon_{yy} = \epsilon_{zz} = \epsilon = \epsilon_0 n^2$ for an isotropic medium of permitivity ϵ and refractive index n in absence of any external magnetizing field. In the presence of external magnetization, $D = \epsilon_0 \boldsymbol{n}^2$, $\boldsymbol{n}$ being the refractive index of medium in magnetic field, (2.5) and (2.6) can be combined to have the eigenvalue equation as,

$$\epsilon_0 \boldsymbol{n}^2 \hat{I} \begin{bmatrix} E_x \\ E_y \\ E_z \end{bmatrix} = \begin{pmatrix} \epsilon & i\mathrm{g} & 0 \\ -i\mathrm{g} & \epsilon & 0 \\ 0 & 0 & \epsilon \end{pmatrix} \begin{bmatrix} E_x \\ E_y \\ E_z \end{bmatrix} \tag{2.7}$$

The solution of this equation will give two circularly polarized normal modes RCP and LCP with eigen vectors $\left[(E_x, \quad \pm iE_y, \quad 0)\right]$ and corresponding eigenvalues as

$$\boldsymbol{n}_{\pm} = \sqrt{\epsilon \pm \mathrm{g}} \tag{2.8}$$

After passing through a length L of the material material under the influence of a magnetic field (B), the two circular polarization components have a relative phase shift:

$$\Delta\phi = \frac{2\pi}{\lambda}\left(n_+ - n_-\right) L = \frac{2\pi}{\lambda}\left(\sqrt{\epsilon + \mathrm{g}} - \sqrt{\epsilon - \mathrm{g}}\right) L \ .$$

As the gyrotropy parameter is a small perturbation, assuming $\mathrm{g} <<< \epsilon$,

$$\sqrt{\epsilon + \mathrm{g}} = \sqrt{\epsilon}\left(1 - \frac{\mathrm{g}}{\epsilon}\right)^{\frac{1}{2}} \approx \sqrt{\epsilon}\left(1 - \frac{1}{2}\frac{\mathrm{g}}{\epsilon} + ...\right),$$

and

$$\Delta\phi = \frac{2\pi}{\lambda}\frac{\mathrm{g}L}{\sqrt{\epsilon}}$$

Then the polarization rotation angle is given as:

$$\theta_P = \frac{1}{2}\Delta\phi = \frac{\pi}{\lambda_0}\frac{\mathrm{g}L}{\sqrt{\epsilon}} = \frac{\pi}{\lambda_0}\frac{\mathrm{g}L}{n} \tag{2.9}$$

In contrast to this optical activity, in magnetic garnet materials like TbGG and YIG, the gyration vector does not dependent on direction of propagation. Rather they do

depend on the direction of magnetization ($\vec{M}$), i.e.

$$\mathrm{g}(\vec{k}) = \mathrm{g}(-\vec{k})$$

$$and$$

$$\mathrm{g}(\vec{M}) = -\mathrm{g}(-\vec{M})$$

as g $\propto M$. In paramagnetic and diamagnetic magneto-optical materials, the polarization rotation also known as Faraday rotation is proportional to the magnetic field B along the direction of propagation and is given as

$$\theta_F = VBL \tag{2.10}$$

where V is called the Verdet constant of the material. In ferro- and ferri-magnetic materials, Faraday rotation is given as,

$$\theta_F = F\left(\frac{M}{M_s}\right)L \tag{2.11}$$

where M_s is the saturation magnetization and F denotes the Faraday rotation coefficient (degree per unit length) The sense of the polarization rotation in these magnetic garnet materials doesn't reverse for the reversal of the direction of propagation. The effect is called non-reciprocal, in other words, the materials break the time reversal symmetry. This is why the Faraday rotation is doubled and not canceled when linearly polarized optical beam passing through the magneto-optic material is reflected into

the material. This non-reciprocal phenomena is the essence of the Faraday rotator-based optical isolators. As shown in figure 2.1 a magneto-optical isolator consists of two polarizers inclined with each other by 45^0 and a Faraday rotator component with length chosen such that it rotates the polarization by 45^0 in one way travel through the rotator. Any reflected light will go further 45^0 rotation in the same sense of rotation so that its polarization axis becomes vertical to the axis of polarization of the first polarizer and the light is blocked from reflecting and interfering to the optical components towards the input sides of this isolator.

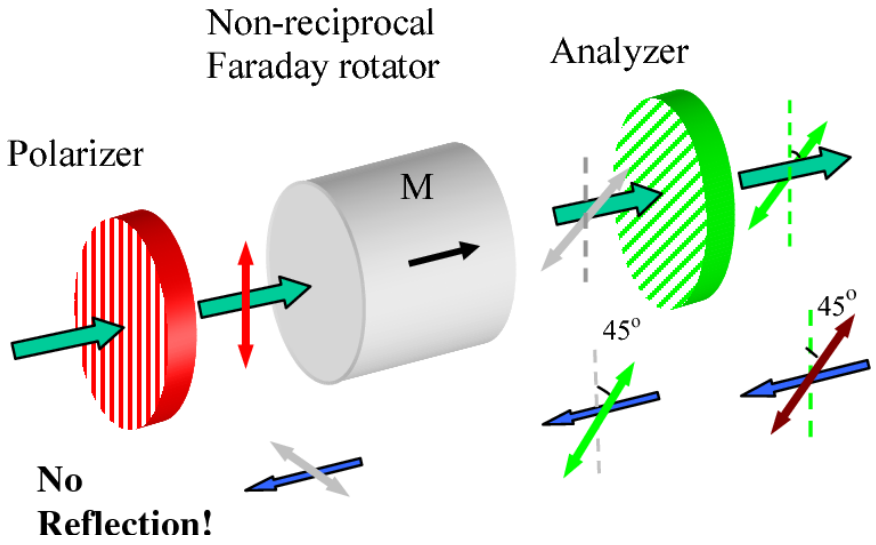

Figure 2.1: Schematic of the magneto-optical Faraday rotator isolator [44]

2.3 Magnet-less magnetic garnets

Magnetic garnet materials are the widely used and investigated MO materials for non-reciprocal devices at telecommunication wavelengths of 1.3 and 1.55 μm near infrared (NIR) because of its highest figure of merit, ratio of the Faraday rotation to the optical loss. However many of these materials grown by Liquid Phase Epitaxy (LPE) ,sputter epitaxy or pulse Laser deposition (PLD) are multi-domain ferrimagnets and require high magnetizing field to maintain at saturation or single domain state to achieve its highest MO activity. This requires external bias permanent magnet such as Samarium cobalt (SmCo)or Neodymium (Nd) magnet to be incorporated into the device and limits its applications where small device size and weight is required. Not only this makes the devices expensive and bulky but also it may effect other nearby components. In the quest for finding right composition of the elemental composition, Brandle, Jr. et al. [18] and Abbott et al. [19] has outlined the different dimension of the conditions and requirements to grow these kind of materials. The results of which is summarized in this section along with some fundamental structural and magnetic properties of these type of materials.

2.3.1 Structural background

MO garnets are rare-earth iron garnets (RIG) with cubic crystals structure. Each unit cell has eight formula units of $R_3Fe_5O_{12}$ and each formula unit has three different lattice sites tetrahedral (a), octahedral (d) and dodecahedral (c) lattice sites. As

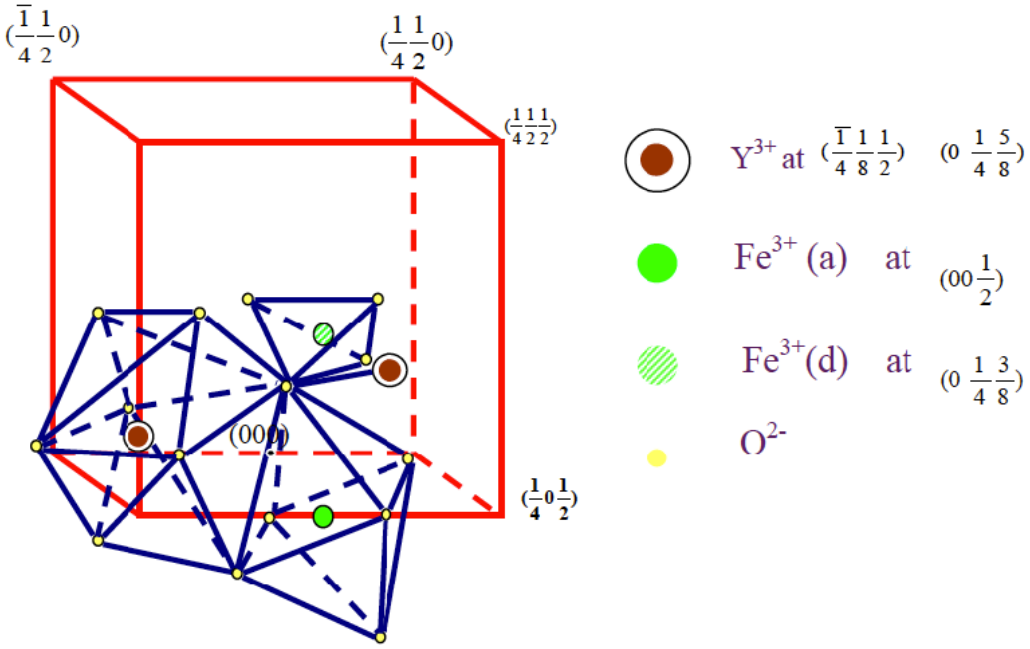

Figure 2.2: YIG formula unit with cations at different sublattices [44]

shown in Fig. 2.2, Fe ions occupy tetrahedral and octahedral sites whereas rare earth ions (yttrium in this figure) occupy the dodecahedral lattice sites. General chemical formula regarding number of ions in different lattice sites can be represented as

$$\left(R^{3+}\right)_3^{\text{dodeca.}} \left(Fe^{3+}\right)_2^{\text{octa.}} \left(Fe^{3+}\right)_2^{\text{tetra.}} O_{12}$$

Each formula unit has three rare earth ions R^{3+}in dodecahedral sites , 2 Fe^{3+} ions in octahedral sites and 3 Fe^{3+} ions in tetrahedral sites. So the saturation magnetization that depends on temperature (T) is given by the contribution from all three lattice sites as

$$4\pi M_s(T) = |M_d(T) - M_a(T) - M_c(T)| \tag{2.12}$$

where M_c, M_d and M_a are the magnetization from dodecahedral, tetralhedral, and octahedral sites, respectively. Since dodechedral sites are occupied with non-magnetic rare earth ions such as yttrium (Y) in YIG, dodecahedral site has no contribution to net magnetization, i.e. $M_c(T) = 0$ and (2.12) simply becomes

$$4\pi M_s(T) = M_d(T) - M_a(T) \tag{2.13}$$

As there are more Fe^{3+} ions in tetrahedral sites than in the octahedral sites, and the magnetization due toFe^{3+}ions in these two different lattice sites is opposite, the net magnetization is along the direction of the tetrahedral sites. This makes YIG ($Y_3Fe_5O_{12}$) ferrimagnetic in nature and this small magnetization provides YIG with a small positive Faraday rotation. However when some of Y^{3+} ions in dodecahedral sites are partially replaced with Bi^{3+}, then it not only monotonically increases the Faraday rotation with Bi substitution but also reverses the direction of rotation. Pure YIG has $+\theta_F = +0.084/\mu m$ while complete substitution of yttrium by Bi (BiIG) yields $-\theta_F = -7.8^0/\mu m$ at 632 nm wavelength. At NIR wavelength of 1310 nm,

the FR value of YIG is $214^0/cm$ where as the highest value of Bismuth substituted (Bi:YIG) is $4300^0/cm$ at 1550 nm [45]. In general, Faraday rotation of magnetic garnets depends on temperature (T), wavelength λ and on sublattice magnetization (M) as

$$\theta_{F,sat.}(\lambda, T) = C(\lambda)M_c(T) + D(\lambda)M_d(T) + A(\lambda)M_a(T) \tag{2.14}$$

Where C, D and A are coefficients that only depend on wavelength.

2.3.2 Elemental substitution for single domain

Normal ferrimagnetic garent materials have multiple domains and high saturation magnetization. Upon application of an external magnetic field greater than or equal to saturation magnetization, all the domains align themselves along the direction of the applied field and essentially form a single domain. However when the magnetic field is removed, the domains take the original random orientation of multi-domain state. The stable condition required for the single domain state is

$$H_k - 4\pi M_s > H_{sat} \ ,$$

where H_k is magnetic anisotropy field, $4\pi M_s$ is saturation magnetization and H_{sat} is saturation magnetizing field [46, 47]. As shown in the hysteresis loop of figure 2.3,

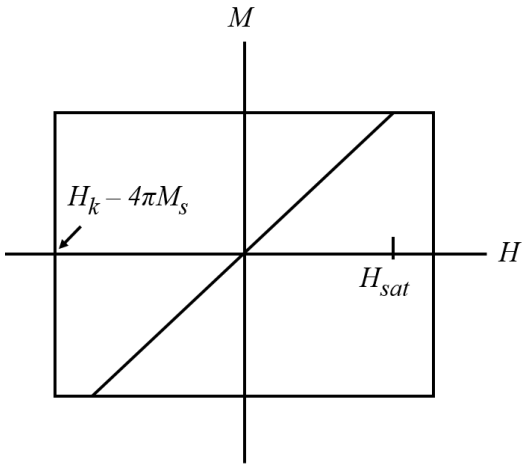

Figure 2.3: Hysteresis loop for a self bias stable condition [46]

after initial saturation, the sample can not be demagnetized until a reverse switching field greater than $H_k - 4\pi M_s$. At the switching field the sample still remains in a single domain state with reverse magnetization. In the chemical formula of the garnet $(Bi_x\ A_{3-x})(Fe_{5-y}C_y)O_{12}$, where A constitutes one or more of the rare earth ions of Y, Ca and elements of atomic number from 57 to 71, C is one or more of the elements Al, Ga, Si, Ge, Mg, Mn and Zr, fraction y is in the range of 0.2 to 2. The fraction and type of elements chosen is governed by the following requirements and constraints:

1. To keep single saturated domain state, the saturation magnetization $4\pi M_s <$ 100 Gauss must be maintained over the typical device operating temperature of -40^0C to 80^0C. At the same time, the switching field H_{switch} or equivalently

coercive field H_c should be $\geq$ 500 Oe at room temperature so that the bias-free MO film is not affected by surrounding conditions while used in an optical circuits. Diamagnetic ions, which preferentially substitutes Fe in tetrahedral site and do not have an inverse relation with temperature of their contribution to saturation magnetization to keep Curie temperature high and transparent in NIR wavelength range, are preferred for replacing iron ions. Ga ions are more suitable in this regard than any others. So Fe ions in tetrahedral sites are replaced with Ga ions. Europium (Eu)and Holmium (Ho) ions of proper concentrations C(Eu) $\leq$ C(Ho) are also candidates for this requirement to reduce the saturation magnetization by doping in dodecahedral sites. Maintaining the Eu-ions concentration less than that of Ho-ions will helps to incorporate more Bi ions by reducing the lattice parameter and closely match with that of the substrate CMZ:GGG.

2. To have a high Faraday rotation, higher Bi-ion doping is preferred. Splitting of excited states of Fe^{3+} ions due to enhanced spin-orbit interaction with Bi substitutions is well accepted theory behind higher MO effect [48, 49]. However a higher substitution of bismuth results into larger lattice parameter, thus, only certain level of Bi substitutions is allowed to keep the lattice parameter closely match with that of the available substrate for good quality crystal growth.

3. The lattice parameter (LP) mismatch between the MO film and the substrate

should be within the range of 0.006 A^0 and 0.012 A^0, i.e.

$$-0.012A^0 \leq \text{LP(film)} - \text{LP(CMZ : GGG)} \leq 0.006A^0$$

where CMZ:GGG $[(Gd_{2.68}Ca_{0.32})\,(Ga_{1.04}Mg_{0.32}Zr_{0.64})\,Ga_3O_{12}]$ is the high quality single crystal substrate material available for LPE growth of MO garnet. Since the substrate has a lattice parameter between 12.486 - 12.510 A^0, the bismuth substitution is constrained to 1.2 per formula unit, i.e. $x < 1.2$. As about 470 μm thick MO material is required for full 45^0 Faraday rotation assuming 0.096^0 μm^{-1} as the highest reported specific FR of LPE grown garnet on CMZ:GGG substrate, the lattice match should be within the above range to maintain the high quality of the film, otherwise dislocations in the crystal and film cracking may cause degradation in the film quality.

2.4 Motivation towards magnetless optical isolator

Optical isolators are the major components in the photonic circuits that are not yet fully developed to provide greater than 30 dB of isolation and less than 1 dB of insertion loss. Because of this a full functioning photonic integated circuit has not been realized. Numerous researcher are devoted in this device that would provide the necessary merits to be used in a on-chip laser by reducing its size. Previous works

on isolators using different designs such as Mach-Zehnder interferrometer (MZI), ring resonators, non-reciprocal mode conversion (NRMC), Quasi-Phase matching (QPM) FR etc. have been able to produce either one of the merits but not the both [11, 22–25, 27, 50–58]. Recent work from MIT group [57] has developed an isolator with 40 dB of isolation and 3 dB of loss. However their device has still more loss than desired in a on-chip isoltor as well as external magnet is still needed to magntize the MO element. Moreover, devices based on ring resonators concept will have low

Table 2.1
Previous works on optical isolators based on different designs and their performances.

Literatures	Device designs	Isolation ratio (dB)	Insertion loss (dB)	Device length (mm)	Need biasing magnets ?
Shintaku et. al.[51]	NRMC[a]	27	8-11	4.1	Yes
Shintaku et. al.[11]	NRMC	24	4.6	3.15	Yes
Shintaku et. al.[50]	NRMC	13.3	6.3-8.1	4.5	Yes
Shoji et. al.[24]	MZI[b]	< 21	> 8	4	Yes
Shoji et. al.[52]	MZI	27	14	0.5	Yes
Shoji et. al.[59]	MZI	30	13	0.5	Yes
Ghosh et. al.[25]	MZI	25	14	0.9	Yes
Ghosh et. al.[53]	MZI	32	22	3	Yes
Zhang et. al.[54]	FR[c]	11	4.6	4	Yes
Huang et. al.[55]	MZI	29	9-11	1	Yes
Huang et. al.[56]	Resonator	32	2.3	0.07	Yes
Bi et. al.[27]	Resonator	19.5	18.2	0.29	Yes
Du et. al.[57]	Resonator	40	3	0.3	Yes
Fujita et. al.[23]	MZI	19	13	8	Yes
Levy et. al.[22]	FR	27	7	3.5	Yes
This work	FR	>30	∼0.5	0.5	NO

[a] NRMC (non-reciprocal mode converter).
[b] MZI (Mach-Zehnder interferrometer).
[c] FR (Faraday rotator).

bandwidth. The Table 2.1 shows the collection of isolators devices and their size and merits. So foremost challenge is to get rid of external magnet to magnetize the MO material. This work is committed towards this goal and we have achieved > 30 dB of isolation and < 1 dB of loss. The details of the work is discussed in the further sections of this chapter.

Liquid-phase-epitaxially-grown bismuth-substituted iron garnet mono-crystal materials are regularly used in technologically-important nonreciprocal photonic components, including optical isolators, circulators and switches. These materials are especially valued for their high-optical quality, particularly low-loss and large Faraday rotations in the infrared telecom wavelength range. Latching Faraday-rotator LPE iron-garnets have the additional remarkable attribute that they do not require bias magnets for their operation. This significant feature makes it possible to greatly reduce rotator device size relative to designs that require an external applied magnetic field. At a 1.55 μm wavelength they typically display 0.43 dB/cm optical absorption and 938 deg/cm Faraday rotation, making them ideal nonreciprocal device materials.

The key to magnetless operation resides in the composition of the garnet. A saturated magnetic state without bias magnets is achieved through maximizing the incorporation of europium (Eu) as discussed in section 2.3.2 in order to reduce the saturation magnetization of the garnet without creating a compensation point [18, 19]. The nominal composition of the garnet is $Bi_X(Eu_ZHo_{1\text{-}Z})_{3\text{-}X}Fe_{5\text{-}Y}Ga_YO_{12}$ per

formula unit. These materials are grown on (111)-oriented single-crystal Ca/Mg/Zr-substituted gadolinium gallium garnet (CMZ-GGG) substrates and their integration into silicon or into other non-compatible platforms has not been demonstrated. As grown, their magnetization axis is normal to the plane of the film (Fig.2.4(a)). Therefore the on-chip integration of these Faraday rotators into alternative platforms requires post-LPE-growth manufacturing to form a new thin-film-plane. Its normal should be perpendicular to the growth direction, as in Fig. 2.4(b). The optical propagation axis must be along the magnetization direction.

This part of the work details the fabrication of such films and their integration

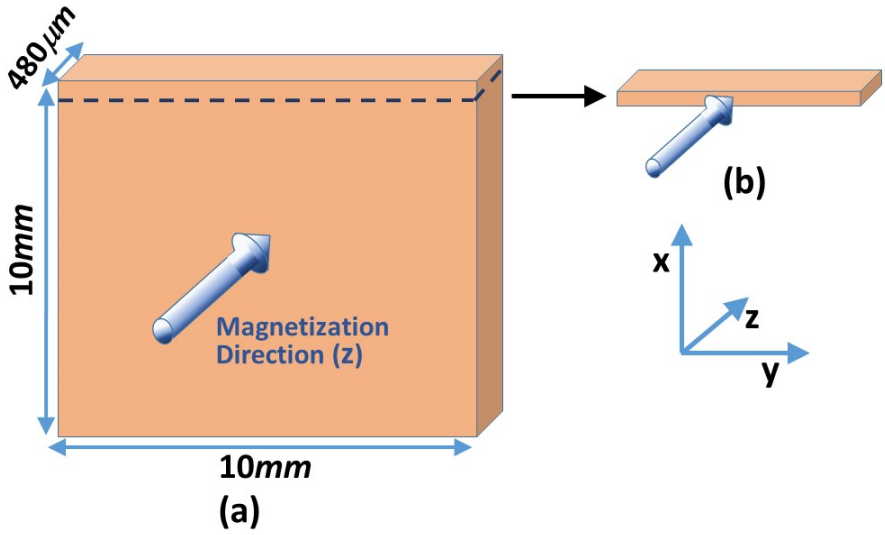

Figure 2.4: Geometry of the latching Faraday rotators. The magnetization direction is normal to the large faces. (Drawing not to scale.)

into silicon-on-insulator (SOI) and other platforms. It is shown that processed films

via mechanical thin-down lapping retain their magnet-less latching character and their original bulk Faraday rotations without re-poling to within experimental error. Film-transfer onto silicon photonic chips by crystal-ion-slicing is also described. This latter technique was originally introduced by Levt et al. for non-latching iron garnets [60] and is here extended to latching materials . Tests show that ion-implanted samples exhibit minimal changes in magneto-optical properties from the bulk, and excellent optical transmission, as detailed below.

2.5 Processing and magneto-optical properties of mechanically processed thin-films

Anti-reflection-coated 480 μm-thick, 10×10 mm^2 latching Faraday-rotator pieces were procured from Integrated Photonics, Inc. These materials retain their magnetization without externally applied magnetic fields for their operation. The pieces were cut to produce 45^0 rotations at normal incidence. Faraday rotation and insertion loss measurements on the as-procured samples at 1.55 μm wavelength performed in our laboratory yielded $44.3^0 \pm 1.3^0$ and 0.02 dB, respectively.Strips measuring 2 $mm \times 10$ $mm \times 480$ μm were cut off from the original pieces, with the magnetization direction along 480 μm-long side. The 2 $mm \times 10$ mm facets

remained anti-reflection-coated on both sides. These strips were crystal-wax-bonded to silicon platforms and the side was thinned down via diamond-film lapping. The finest diamond particles size used for polishing was 0.25 μm. Films of three different thicknesses 11 μm, 50 μm, and 300 μm were produced and measured. Figure 2.5 insets show scanning-electron-microscopy (SEM) micrographs of 11 μm,and 50 μm thick films.

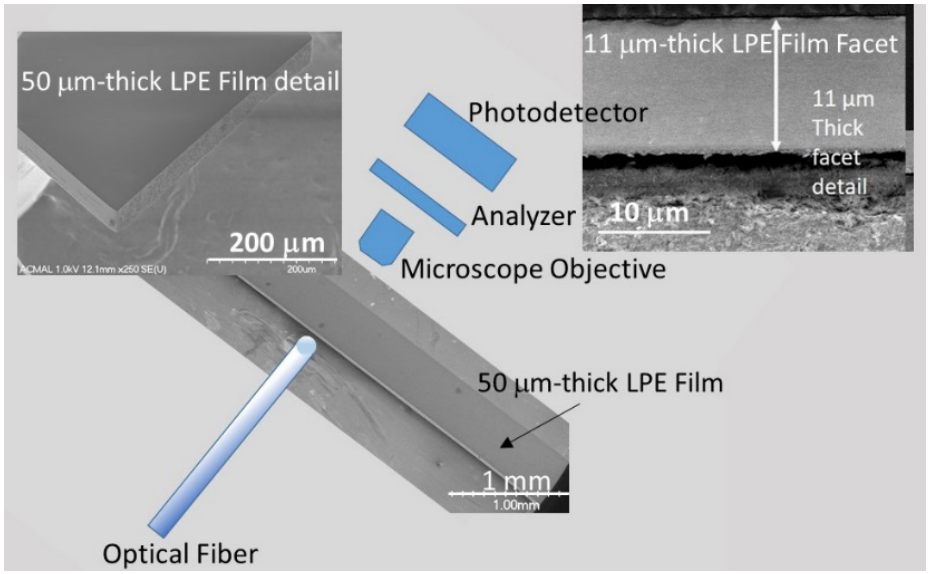

Figure 2.5: 50 μm thick film cross-section SEM images, with schematic depiction of the optical fiber and detection components used for Faraday rotation testing. Inset on the left shows the top side of the 50 μm thick film whereas inset on the right is the cross-section image of 11 μm thick film.

2.6 Measurement Set up

Figure 2.6 depicts the Faraday rotation testing setup used to characterize the processed films. A single mode lensed fiber couples linearly polarized light set by digital polarizer controller (Agilent 11896A) into the Faraday rotator. A 10X microscope objective collimates the beam through sample and is split into two beams by a 60% /40% non-polarizing beam-splitter. A Glan-Thompson polarizer with sub-degree pre-

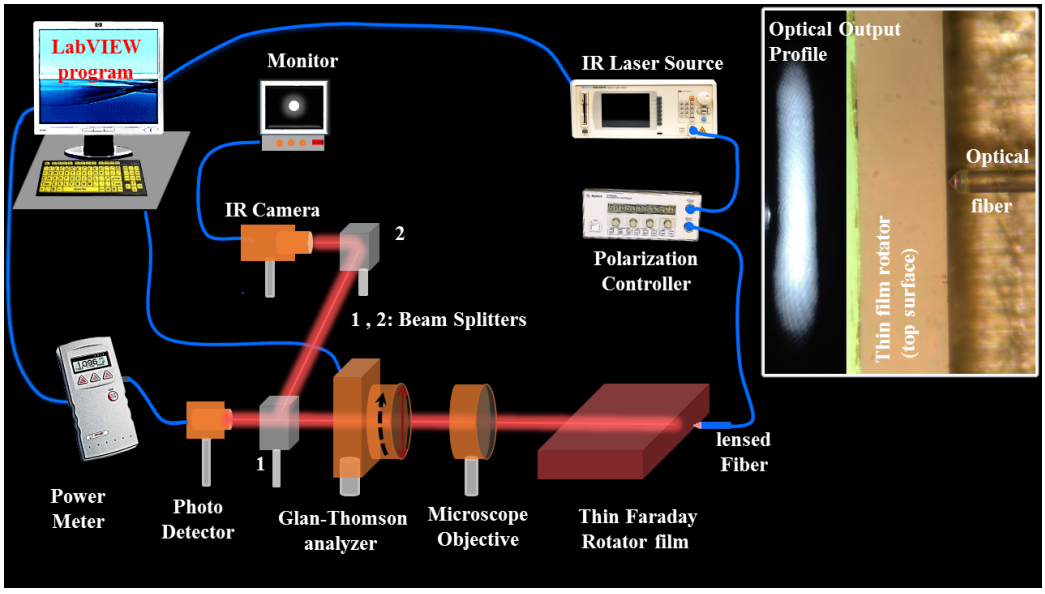

Figure 2.6: Testing set-up for measuring Faraday rotation in the latching iron garnet film samples. The inset shows the diffracted output image from the 11 μm-thick film. It also shows a top view of the lensed fiber tip and the top surface of the film.

cision and a photodetector (Ophir PD300-IR) with nano-Watt (nW) resolution, and 15 Hz sampling rate, is used to analyze one of the beams. The other beam is utilized

to visualize the shape and intensity output profile using infra-red CCD (charge coupled device)camera (Hamamatsu)and a monitor screen. The light is confined along the direction of index variations but diffracts laterally in the film, as evidenced by the output image (Fig.2.6 inset) from the 11 μm-thick sample. Faraday rotations,

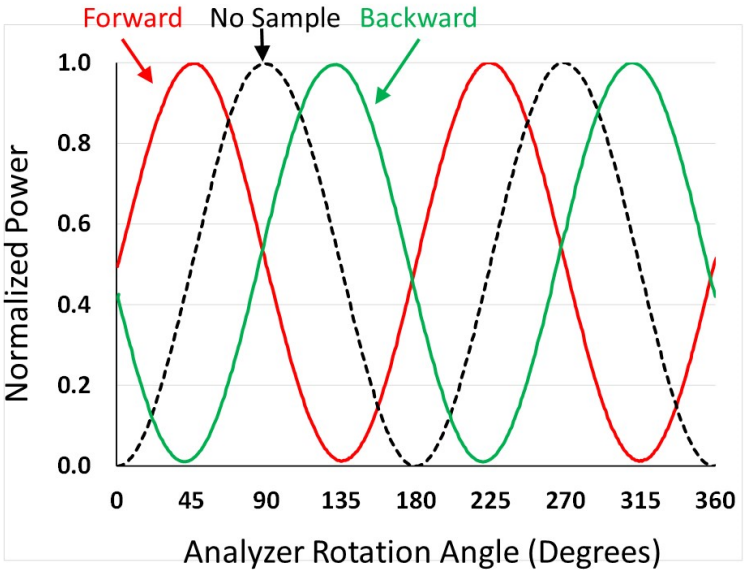

Figure 2.7: 360^0 analyzer rotation scans with and without 11 μm -thick sample in the beam path.

insertion losses and extinction ratios for three mechanically polished films, all without re-poling (re-magnetized), are shown in Table 2.2. Extinction ratios are defined as the power ratios between minimum and maximum transmission powers for the Faraday rotations, in dB. For the purposes of this table, we define Faraday rotation as the direction of the semi-major axis of the rotated polarization ellipse. The rotations are exhibited for opposite propagation directions, where forward propagation is defined in the magnetization direction. Uncertainties correspond to one standard deviation

from the average values of several measurements in each case. Also displayed in the table is the response for the bulk material. The polarization response of the 11 μm -thick film as a function of analyzer angle for one of these measurements is shown in Fig.2.7.

Table 2.2
Faraday rotations(FR), extinction ratios (ER) and insertion losses (IL) for mechanically polished films without re-poling.

Sample	**FW-FR**	**BW-FR**	**ER**	**IL**
Bulk	$44.7^0 \pm 0.9^0$	$44.5^0 \pm 0.6^0$	$-30 \quad dB$	$0.02 \quad dB$
300 μm $-$ thick	$45.2^0 \pm 1.0^0$	$44.3^0 \pm 0.9^0$	$-30 \quad dB$	NA
50 μm $-$ thick	$45.6^0 \pm 0.8^0$	$44.2^0 \pm 0.5^0$	$-30 \quad dB$	NA
11 μm $-$ thick	$46.7^0 \pm 2.1^0$	$41.9^0 \pm 1.9^0$	$-20.5 \pm 2.0 \quad dB$	$0.09 \pm 0.01 \quad dB$

2.7 Mode birefringence and Faraday rotation

Slab waveguides introduce a disparity between transverse-electric (TE) and transverse magnetic (TM) mode indices (linear birefringence) in addition to the existing circular birefringence inherent in the Faraday effect. As a consequence, the output polarization acquires some degree of ellipticy and suffers rotational departures from that of the bulk material. However, it was found that this effect is negligible for 300 μm - and 50 μm -thick films, and is relatively small for 11 μm -thick films.

In the presence of linear birefringence, the otherwise circularly-polarized counter-gyrating normal modes of the Faraday rotator become elliptically polarized, and their phase difference after any given propagation length L changes as well. Given an intrinsic Faraday rotation angle per unit length θ_F and linear birefringence between TE and TM modes $\mathrm{n_{TE}} - \mathrm{n_{TM}}$, the phase mismatch between counter-gyrating elliptical normal modes after a distance L becomes

$$\phi = 2L\sqrt{(\theta_F)^2 + \left[\frac{\pi}{\lambda}\left(n_{TE} - n_{TM}\right)\right]^2} \tag{2.15}$$

where λ is free space wavelength. Taking into account the calculated geometrical birefringence $n_{TE} - n_{TM}$ for an $11 - \mu m$ -thick iron-garnet slab with crystal bond bottom cladding yields the following polarization rotations and extinction ratios for the first four waveguide modes in Table 2.3. These are obtained making use of the calculated phase mismatched from Eq.(2.15). We assume, the film index = 2.35, bottom cladding index = 1.5277, and wavelength of light $\lambda = 1.55\ \mu m$. Notice that the observed $11 - \mu m$ -thick film extinction ratio displayed in Table 2.1 is consistent with the detrimental presence of higher-order modes in the slab waveguide. Other effects such as film-surface roughness and stress birefringence cannot be completely ruled out. A single-mode waveguide (SMW) structure with square cross-section can eliminate detrimental higher order modes as well as geometrical birefringence as the boundary condition for both TE and TM components become the same for square

Table 2.3
Calculated polarization rotations and extinction ratios for the first four waveguide modes of an 11 μm thick iron-garnet slab at $\lambda = 1.55\ \mu m$.

Waveguide Mode	$\mathbf{n_{TE} - n_{TM}}$	**Polarization Rotation**	**Extinction Ratio**
Fundamental	0.000025	45.17^0	-34.0 dB
First	0.000103	45.30^0	-23.7 dB
Second	0.000231	45.50^0	-15.9 dB
Third	0.000414	45.90^0	-11.7 dB

geometry. Fabrication is achievable through additional processing (thinning and patterning)and the SMW geometry should, theoretically, yield extinction ratios higher than -30 dB, as predicted in Table 2.3.

2.8 Polarization rotation tests on slab waveguides formed by ion implantation

Crystal ion slicing proceeds via energetic He-ion implantation into metal oxides [60, 61]. In this work, the ions were accelerated to an energy of 3.5 MeV and deposited at a dose of $5 \times 10^{16} cm^{-2}$. Rapid thermal annealing (RTA) under nitrogen flow for 30 sec. in the temperature range 700^0C to 800^0C produced the best

results. A low refractive-index sacrificial layer due to the implantation forms below the surface that is then etched away to detach the top film from the rest of the sample. This sacrificial layer can act as a cladding layer for slab waveguiding prior to detachment. The Faraday rotation and insertion loss of linearly-polarized

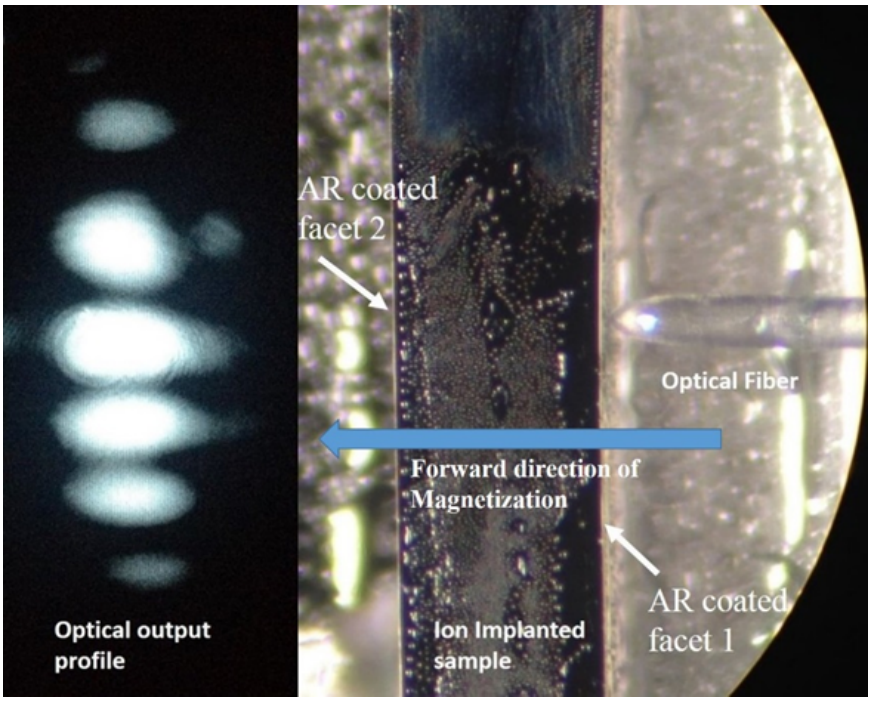

Figure 2.8: Fiber coupling configuration on one of the AR coated facets of the sample (480 μm in length along the direction of propagation) with top polished surface, inset shows the higher order mode profile from the ion implanted planar waveguide structure,(Note: the sacrificial layer formed due to ion implantation has lower index of refraction and serves as a cladding layer of the slab waveguide thus formed.

light passing through these slab waveguides were characterized for different post-implantation rapid-thermal-annealing (RTA) preparation conditions. It was found that the magneto-optic response depended on RTA, approaching bulk material response at higher tested annealing temperatures. The output intensity profile after

propagation is shown in the inset in Fig. 2.8. End-fire coupling (also known as butt coupling) from the lensed fiber onto the anti-reflection (AR) coated facet of the slab waveguide is also shown. A comparison of the magneto-optical response in the ion-implanted slab waveguides with the mechanically-thinned-down films evinces a more pronounced polarization ellipticity and somewhat larger departures from bulk Faraday rotation. These more pronounced departures from bulk behavior in the ion-implanted slabs are consistent with a smaller waveguide thickness and the presence of high-order waveguide modes. Table 2.4 compares the performance in these two types of waveguides. The polarization ellipticity amelioration at higher RTA temperatures, referred to before, is also consistent with implantation-damage repair and segregation of residual crystal defects away from the waveguide core and towards the sacrificial layer. Figure 2.9 shows 360^0 analyzer rotation scans with and without the ion-implanted sample in the beam path, without re-magnetizing with external magnet.

Table 2.5 shows the calculated departures from intrinsic Faraday rotation and power extinction ratios in 8 μm-thick slab waveguides as a result of mode birefringence. These results are consistent with the more pronounced departures as compared to the 11 μm-thick film. Insertion loss data in the ion-implanted slab waveguide was also measured at wavelength and found to be 0.12 ± 0.01 dB, slightly higher than the 0.09 ± 0.01 dB in the unimplanted sample (Table 2.4). We tentatively ascribe this higher optical loss to residual post-anneal implantation-induced lattice damage in the

Table 2.4
Comparison of the magneto-optical responses: Forward(FW) FR, backward (BW) FR, extinction ratio (ER) and insertion loss (IL) of ion-implanted slab waveguides with mechanically-thinned-down films.

WG thickness	FW FR	BW FR	ER dB	IL dB
11μm	$46.7^0 \pm 2.1^0$	$41.9^0 \pm 1.9^0$	-20.5 ± 2.0	0.09 ± 0.01
8μm (implanted)	44^0	40.7^0	-17	0.12 ± 0.01

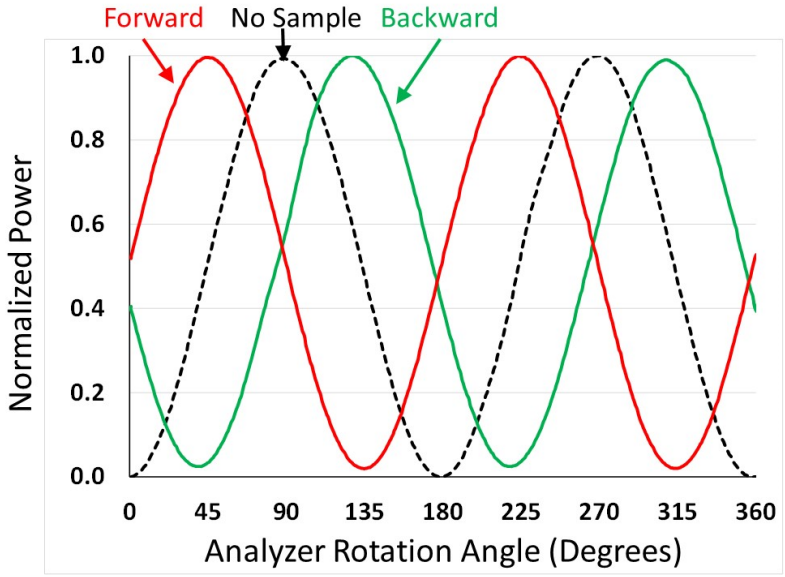

Figure 2.9: 360^0 polarizer rotation scans with and without the sample in the beam path (No external magnetizing field). Data at 1.55 μm wavelength.

core and cladding lattice defects in the optical waveguide.

Table 2.5
Calculated slab waveguide mode polarization-rotation departures from 45^0 (semi-major axis of polarization ellipse) in Faraday rotator due to mode birefringence. Slab and substrate refractive indices are assumed to be 2.35 and 1.95, respectively. Slab thickness is 8 μm .

Waveguide Mode	**Departure from 45^0**	**Extinction ratio**
Fundamental	$\pm 0.4^0$	-28.5 dB
First	$\pm 0.5^0$	-15.9 dB
Second	$\pm 3.4^0$	-9.5 dB
Third	$\pm 10.4^0$	-4.6 dB

2.9 Crystal-ion slicing of magnetless thin-film Faraday rotators

Crystal-ion-slicing involves the ion implantation of energetic light ions to generate a sacrificial damage layer below the sample surface [60, 61]. This induces differential etching that undercuts the top layer when the sample is immersed in phosphoric acid to release the film. Rapid thermal annealing prior to etching repairs residual damage due to the ion trajectories above the sacrificial layer and enhances the differential etch rate with the sacrificial layer. Prior work has shown crystal ion-sliced transfer of magnetic garnet films onto GaAs platforms [60]. Here a similar process was

used to demonstrate the transfer of bias-free latching iron-garnet films onto temporary handle substrates and characterize their Faraday rotation and insertion losses after ion-implantation prior to slicing. Future work will characterize their magneto-optic properties after full transfer. Latching Faraday rotator samples were prepared

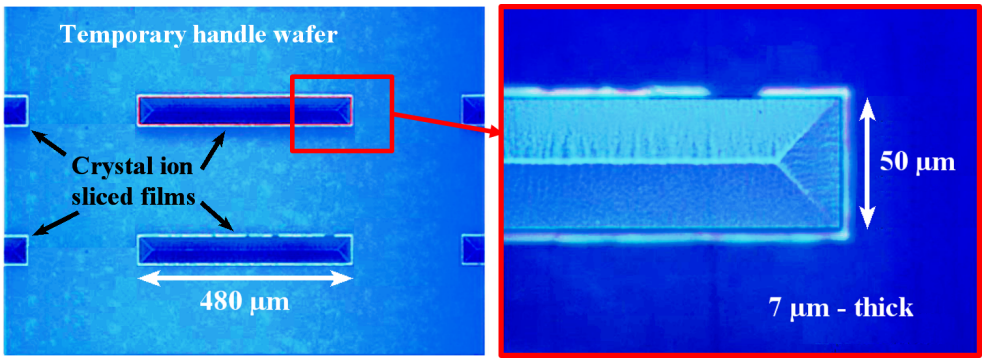

Figure 2.10: Magnetless iron-garnet films on temporary handle substrate after ion slicing (left). Detail on the right panel.

for ion implantation to produce in-plane magnetized crystal-ion-sliced films, with magnetization axis along the propagation direction, as in Fig. 2.4. The as-received 10 $mm \times 10\ mm \times 480\ \mu m$ samples were cut into strips 10 $mm \times 1\ mm \times 480\ \mu m$ using a precision dice polishing process [62]. Strips were then mounted for implantation normal to the 10 $mm \times 480 \mu m$ face in order to form optical slab waveguides for Faraday rotation and absorption loss measurements prior to wet-etch and release of the films. After implant, additional dice polish trenching of the implanted surface was done to form 50 μm wide rectangular features of various lengths from 100 μm to 480 μm . After bonding to a temporary handle wafer, crystal-ion slicing was done by wet etching to transfer the iron garnet films to the handle wafer. Figure 2.10 shows

arrays of transferred films on a temporary handle wafer.

2.10 Transfer to silicon photonic substrates

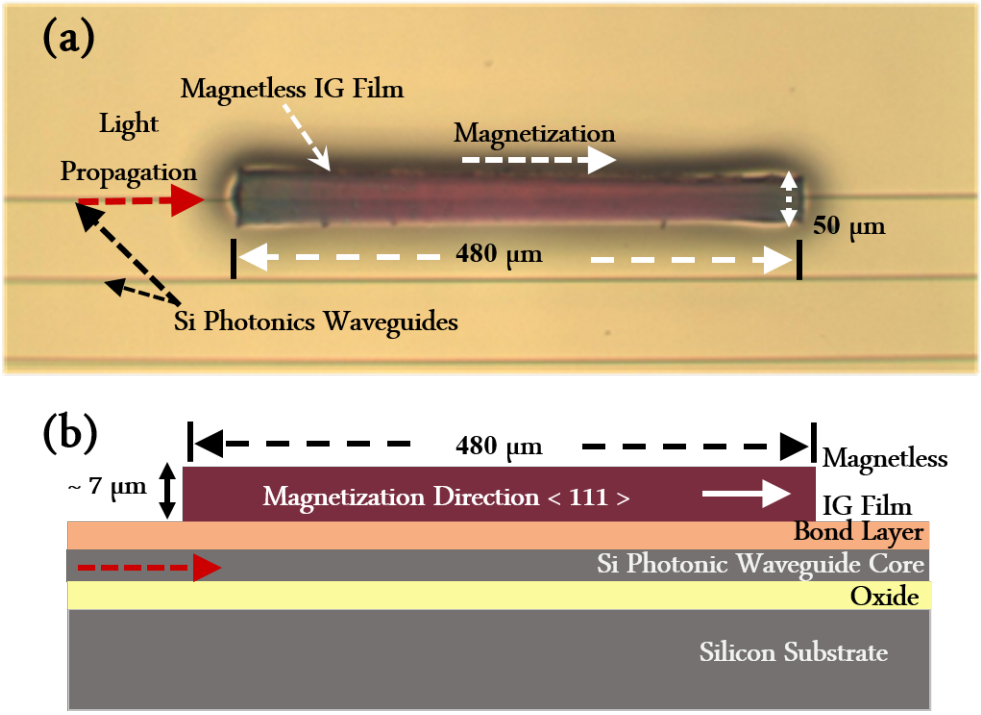

Figure 2.11: Magnetless iron garnet (IG) film bond-align transferred to a silicon photonic substrate (a) top microscope image of bond-aligned film and (b) side view illustration showing the various material layers.

Temporary mounted sliced magnetless iron garnet films of 7 μm thickness were bond-aligned and transferred to silicon photonic substrate by permanent adhesive bonding. An example of a bond aligned film is shown in Fig.2.11. The film may be made to vertically couple to the underlying silicon waveguide by evanescent, reverse taper, grating, or other coupling methods. Alternatively, the film may be aligned and placed

in a pre-milled slot in the silicon photonic substrate.

2.11 Adhesive bonding of polarizers with MO film for full functioning MOI device

Adhesive bonding is a kind of wafer bonding technology in which an intermediate layer of material like UV epoxy, SU-8, Benzocyclobutene (BCB), etc. connects substrates of different type of materials. UV epoxy is often used in fiber optic applications because of its high transparency in IR and NIR spectral ranges and low tamperature curing [63] where as SU-8 and BCB bonding are well established in microelectromechanical systems (MEMS) and nanoelectromechanical systems (NEMS) for stronger bonding and their foundry compatibilty (resistant to numerous acids, alkalines and solvents) [63, 64]. The hardening or curing of the bonding materials is done by applying pressure, UV light exposure, heat treatment, etc. UV epoxy is cured at low temperature 150^0 C where as BCB needs higher temperature $\sim$ 200 to 400^0C. Low outgassing UV epoxy (Epo-Tek 353 ND) and BCB bonding techniques were used in this work to bind two ultrathin PolarCors from Corning [65] at 45^0 angle to each other with MO films sandwiched between them. These ultrathin PolarCor glass polarizers are ~ 30 μm thick and has $>$ 23 dB extinction ratio and $>$ 98% transmission at 1550 nm wavelegnth.

2.11.1 Characterization of MOI with UV epoxy bonded PolarCors polarizers

2.11.1.1 Forward transmission measurements

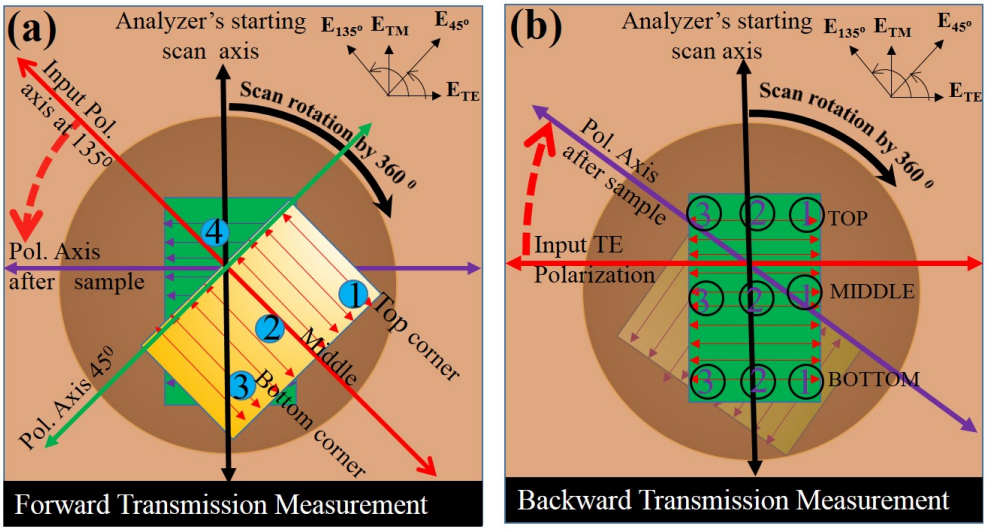

Figure 2.12: Schematic of the front view (a) and backside view (b) of two ultra-thin PolarCors ($2\ mm \times 1\ mm$) bonded on two opposite sides of MO Farady Rotator sample. Numbers inside circles represent different spots on the sample chosen to measure to locate the region where light makes through the sample and both the PolarCor polarizers.

As shown in Fig. 2.12 of the schematic diagram of the two PolarCor polarizers bonded on two opposite sides of the magnet-less MO Faraday rotator at relative inclination of 45^0, different points on the samples (sky blue circular spots) are measured to find out the region where the light actually makes through both the PolarCor polarizers. The spots labeled as "middle and bottom corner" are the ones where both the polarizers

have overlapping regions and light passes through both of them. The other two spots are the ones where light just goes through only one of the two polarizers. Most of the measurements are carried out by making the polarization of the input light parallel to the polarization axis of the front PolarCor polarizer (in this case, the PolarCor film at 45^0 angle). Since the PolarCor film has its axis of polarization parallel to its width (1 mm length side), an input polarization state that makes 135^0 angle to the horizontal direction (See Fig.2.12) is prepared and used as the input state to allow most of the light go through the front polarizer. In addition, the measurements are also taken for other two states of polarization: horizontal (TE) polarization and the polarization axis at 45^0 to the horizontal as shown in Fig. 2.13.

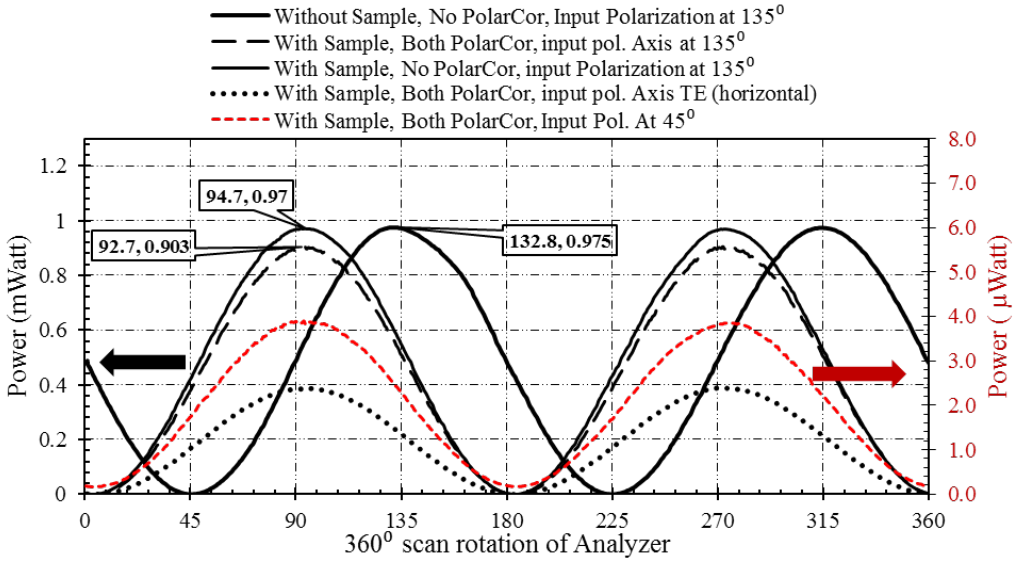

Figure 2.13: Forward power transmission measurement of MO isolator by 360^0 scan rotation of analyzer with different input polarizations conditions as specified in the legend on top of the graph (*note: black colored lines share vertical axis on left side where as red colored line takes vertical axis on right side of the graph)*

Out of 0.97 mWatt of maximum input power (power through sample but with "No PolarCor polarizers"- thinner green solid line in Fig. 2.13 below), 0.903 mWatt power goes through both the PolarCors and the sample resulting in a loss of only about ≈ 0.31 dB. The extinction ratio is > 30 dB.

2.11.1.2 Backward transmission/isolation measurements

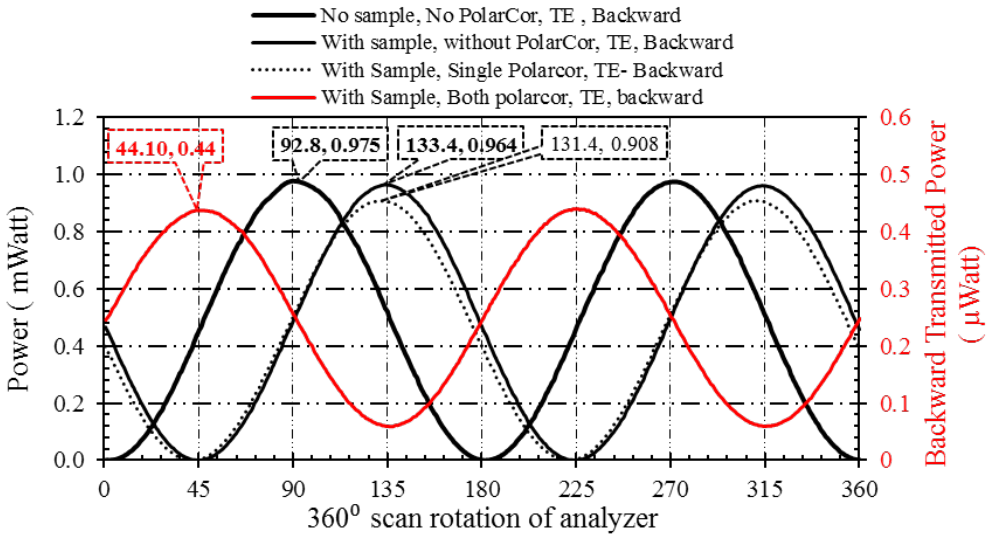

Figure 2.14: Backward Power transmission measurement of MO isolator by 360^0 scan rotation of analyzer with different input polarizations conditions as specified in the legend on top of the graph (*note: black colored lines share left vertical axis where as red colored line takes vertical axis on the right side of the graph)*

For the backward transmission measurement, as shown in the schematic of Fig. 2.12 (b), 9 total different spots (3 spots in the top, middle and bottom region of the vertically placed polarcor) enclosed by circles are considered for the measurements to find the region where the light transmits through both the PolorCors. Only horizontal

input polarization (TE) is used to characterize the performance of the isolator in this case. As shown in the graph of Fig. 4 below, the solid red lines are the measurements in the region with no PolarCors whereas dashed red line corresponds to the spots on the top region where light just goes through the front vertical PolarCor only and misses the backside PolarCor at 45^0. The purple dashed line is the one that goes through both the polarcors and this measurement actually reflects how much light reflects in the backward direction and is used for the calculation of isolation ratio.

2.11.1.3 Isolation ratio and insertion loss Versus wavelength scan

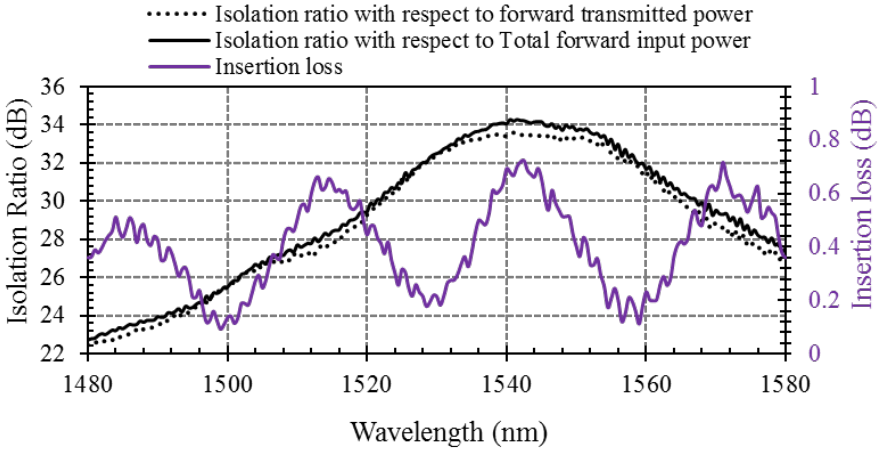

Figure 2.15: Isolation ratio and forward loss as a function of wavelength scan [black colored solid and dashed represent the isolation ratio with reference to total input forward power (No sample, No PolarCor) and forward transmitted power (through sample and both the PolarCors); violet line refers to the insertion loss data].

The wavelength scan from 1480 nm to 1580 nm in steps of 0.5 nm is carried out to measure the forward transmission power for the input polarization at 130^0 and

backward reflected power for TE input polarization from the two opposite sides of the sample as described above. The isolation ratio plotted below shows that the ratio is $> 30\ dB$ for the wavelength between 1522.5 nm to 1564 nm.

2.11.2 Characterization of 250 μm thick (in transverse direction) MOI with BCB bonded PolarCors polarizers

2.11.2.1 Transmission and isolation ratio measurements

These samples were prepared by first bonding the PolarCors polarizers with MO material and then cut with dicing to make pieces of 250 μm in transverse direction (Note: the thickness along the direction of propagation is 480 μm designed to produce 45^0 rotation of polarization. Fig. 2.16 below shows the polarization rotation by a 250 μm thick sample with two PolarCors BCB bonded on two opposite sides. For transmission measurement on this sample, input polarization state at 135^0 angle to the vertical was coupled through the lensed fiber and the analyzer was scanned rotated by 360^0 with vertical polarization axis at the start of scan. The measurement was carried out for both the sides of the device for two cases of forward and backward propagation. The sample rotates by $\sim 45^0$ in opposite directions from the input polarization direction while reversing the side. The insertion loss for 250 μm sample

at 1550 nm wavelength is 1.62 dB and it is less than 2.5 dB for the range of wavelength scanned from 1480 nm to 1580 nm. The isolation ratio at 1550 nm is 25.13 dB and approaches 30 dB towards end of the wavelength scan.

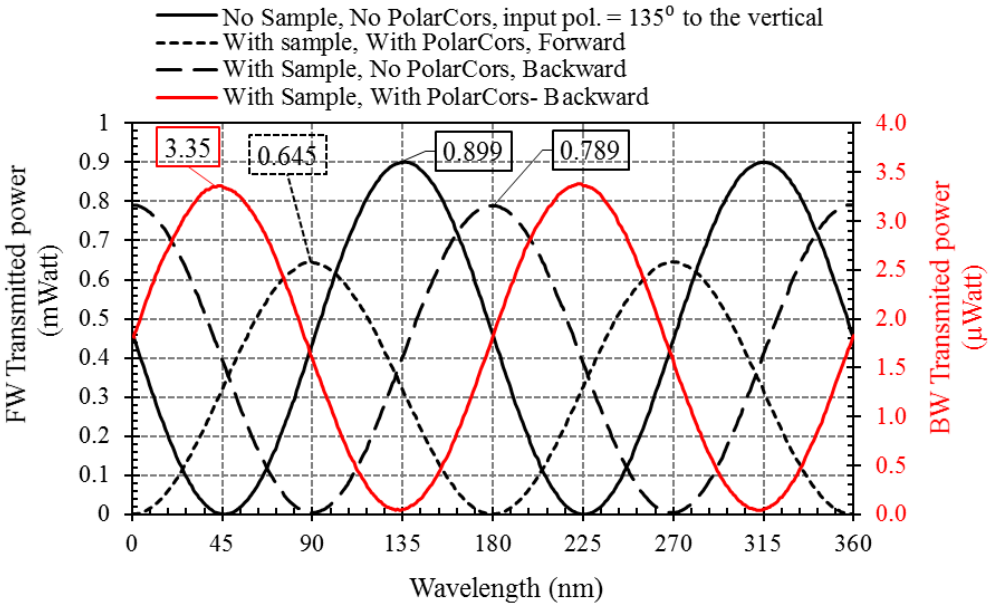

Figure 2.16: Faraday rotation measurement on 250 μm thick sample (rough top and bottom surface resulted from dice cut).

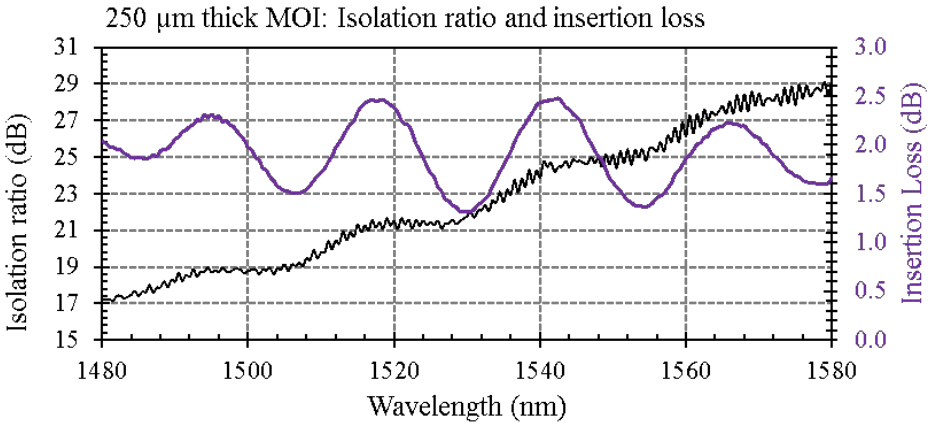

Figure 2.17: Isolation ratio and insertion loss measurements on MOI with BCB bonded PolarCors polarizers.

2.11.3 Transmission and isolation measurements on 60 μm thick MOI device

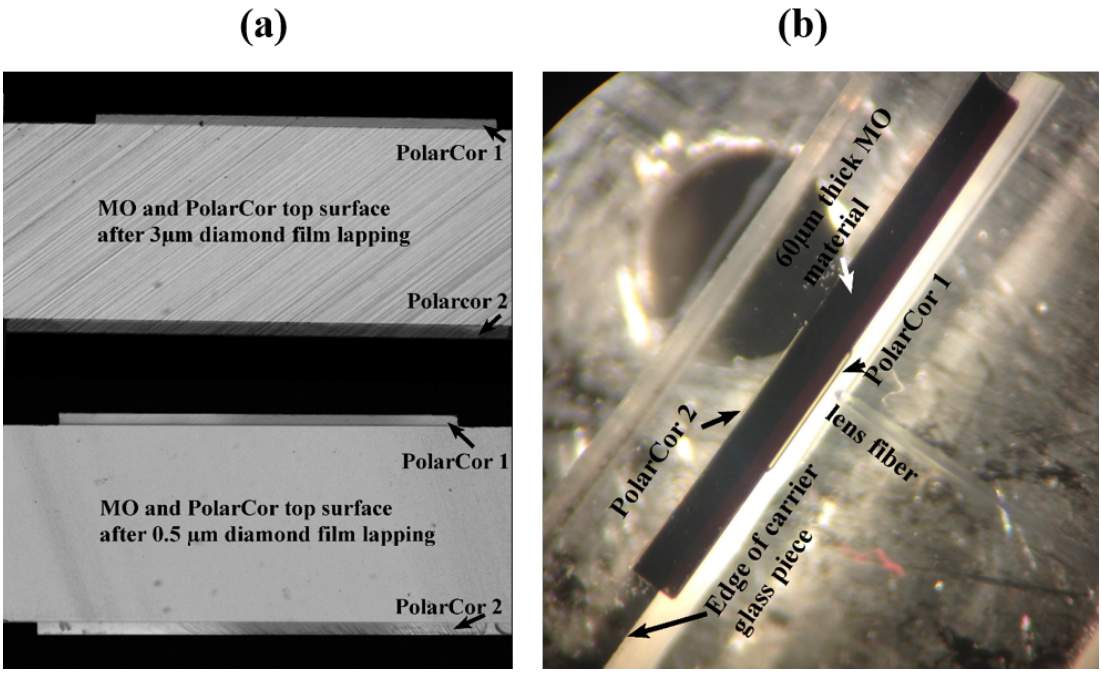

Figure 2.18: MO film BCB bondedwith two PolarCors polarizers (a) Top surface of the MOI device resulted after 3 μm and final 0.5 μm lapping film (b) Lens fiber MOI assembly for the measurement. The MOI device is attached to the edge of the carrier glass piece to bring the fiber within its focal length.

The same sample is bonded onto a thin carrier glass substrate and thinned down to $\sim 60\mu m$ (with thin wax layer, the sample thickness is 63 μm as by 3D optcial profilometer. The diamond lapping films with particles size of 9 μm, 6 μm, 3 μm, 1 μm and finally 0.5 μm were used for thinning and polishing the surface. The optical microscope images of top surface that resulted after lapping with 3 μm and 0.5 μm

films are as shown in Fig. 2.18(a).The thinned-down sample was attached to the edge of the carrier glass piece with some extruding part as shown in Fig. 2.18(b) of the measurement assembly. This allows lens fiber to be brought close enough $\sim 10\mu m$ from the edge of the MOI device to couple the focused spot of input light. To measure the transmission in the opposite direction (backward propagation), the sample was simply re-poled to reverse the magnetization so that the sample does not have to be bonded again with other facet extruding from the glass piece. The analyzer scan rotation measurement of Fig. 2.19 shows that the rotation of polarization by MO material is $\sim 45^0$ in opposite magnetization conditions with reference to the input polarization axis which is 135^0 to the vertical. The insertion loss on this sample is $\sim$

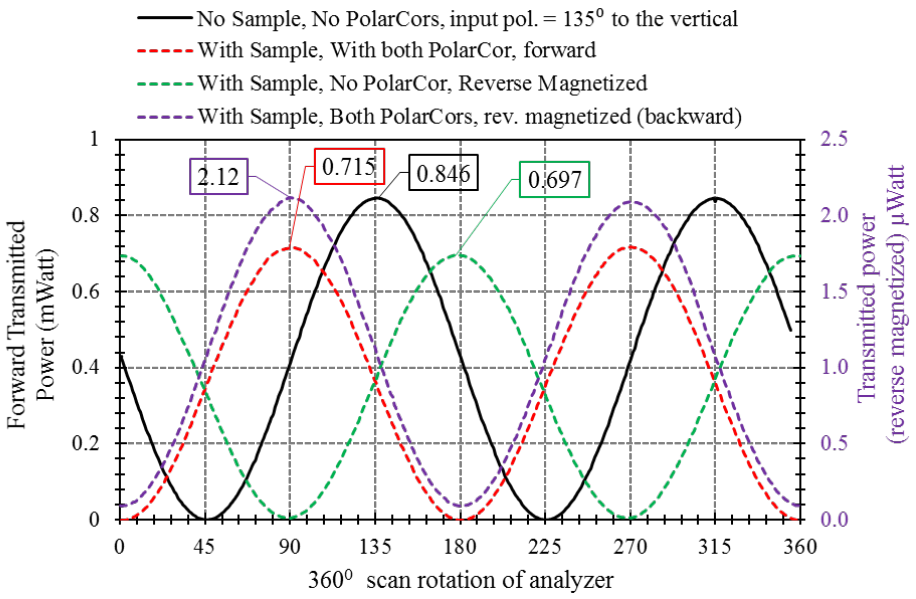

Figure 2.19: 360^0 analyzer rotation characterization on 60 μm thick MOI with BCB bonded PolarCors polarizers at different situations as specified in the legend on top of the graph.(*note: all other lines share left vertical axis except violet colored line which takes right vertical axis on the graph*)

0.63 dB and the isolation ratio is 28.15 dB at 1550 nm. As can be seen in the plot of Fig. 2.20, the insertion loss in the whole wavelength range of 1480 nm to 1580 nm is below 1.2 dB. The isolation ratio exceeds 30 dB at 1580 nm.

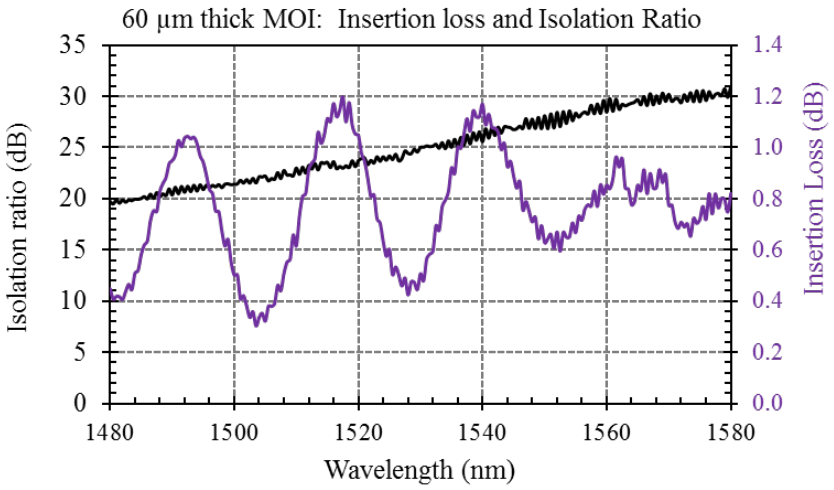

Figure 2.20: Insertion loss and isolation ratio vs. wavelength scan on 60 μm lapped MOI with BCB bonded PolarCor polarizers.

Chapter 3

Topological Su-Schrieffer-Heeger (SSH) array based magneto-optic isolators

3.1 Introduction

The development of on-chip optical isolators for integrated photonic circuits has been actively pursued for several decades now, especially after the introduction of optical fiber telecommunications. Several different designs have been proposed and prototypes implemented [22, 26, 27, 39, 54, 66–73] with different degrees of success. There

are three main criteria that determine the quality of the prototype and its proximity to commercialization or industrial applicability. These criteria consist of the following: isolation ratio, defined as the ratio between the optical-power allowed to exit the device in the backward and forward directions, insertion loss, and footprint. Usually, the figure of merit for these devices is defined as the isolation ratio over insertion loss. But this figure of merit does not encompass the footprint criterion, which in magneto-optic isolator prototypes entails the reduction in size or elimination of the magnetizing element altogether [58].

Magneto-optic systems have been extensively explored because of the nonreciprocal character of the underlying phenomenon. This is a well-established optical isolator technology, used by most commercial devices. Two main operating principles have been explored for on-chip magneto-optic isolators, Faraday rotation [58, 74–76] and the non-reciprocal phase shift effect [27, 54, 77]. Other approaches have also been proposed and studied, such as dynamic non-reciprocity [32], opto-mechanically induced non-reciprocity [78] a non-magnetic method which addresses the elimination of the magnet, and nonlinear techniques [79]. The latter, however, do not provide isolation for arbitrary backward propagating noise [80].

The purpose of the this work is to report on the practical implementation and performance of a novel concept in magneto-optic isolator technology, namely topological edge-state isolators in the optical regime. Topological edge- state phenomena have

been proposed in recent years, and investigated theoretically and experimentally [81–86]. They have been applied in the microwave regime to demonstrate unidirectional propagation in magneto-optical photonic crystals [85]. Here we present on the experimental performance of Su-Shrieffer-Heeger (SSH)-type topological-edge-state structures fabricated in liquid-phase-epitaxy (LPE)-grown bismuth-substituted lutetium iron-garnet (BiLuIG) films.

3.2 Theoretical background

In coupled waveguide arrays when waveguides are in close proximity to each other such that they perturb each other, coupled mode theory (CMT) describes the wave behavior in the perturbed waveguide system [87–89]. Consider the arrays of waveguides as shown in figure 3.1, with inter waveguide coupling constants K_w and K_s for weak and strong coupling between the adjacent waveguides. Then the field amplitudes in waveguides 1 to 7 $[a_1, a_2, a_3, ..., a_7]$ are given by following coupled-mode

equations for loss-less media [38]:

$$\begin{aligned}
i\frac{d\vec{a_1}}{dz} &= \beta\vec{a}_1 + K_w\vec{a}_2 \\
i\frac{d\vec{a_2}}{dz} &= K_w\vec{a}_1 + \beta\vec{a}_2 + K_s\vec{a}_3 \\
i\frac{d\vec{a_3}}{dz} &= K_s a_2 + \beta\vec{a}_3 + K_w\vec{a}_4 \\
&\vdots \qquad\qquad \vdots \qquad\qquad \vdots \\
i\frac{d\vec{a_6}}{dz} &= K_w\vec{a}_5 + \beta\vec{a}_6 + K_w\vec{a}_7 \\
i\frac{d\vec{a_7}}{dz} &= K_s\vec{a}_6 + \beta\vec{a}_7
\end{aligned} \tag{3.1}$$

where β is the propagation constant of each waveguide mode propagating along the z direction.

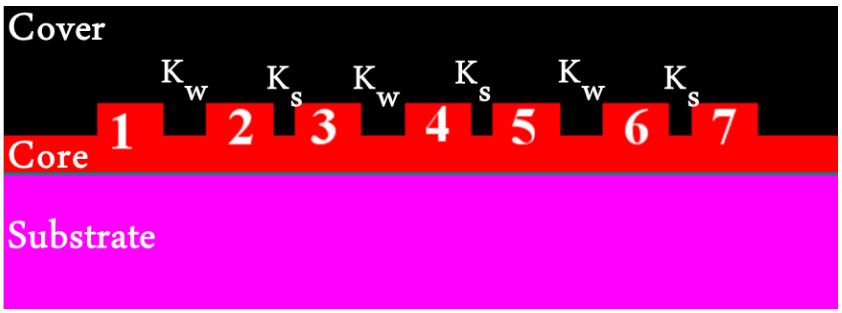

Figure 3.1: Cross-section of an SSH array of 7 waveguides

Concisely above equation can be written as

$$i\frac{d\vec{a_N}}{dz} = H\vec{a} \tag{3.2}$$

where $N = 1, 2, 3, ..., 7$, and the vector $\vec{a} = [\vec{a}_1, \vec{a}_2, ..., \vec{a}_7]^T$ with T : transpose of the matrix, and

$$H = \begin{pmatrix} \beta & K_w & 0 & 0 & 0 & 0 \\ K_w & \beta & K_s & 0 & 0 & 0 \\ 0 & K_s & \beta & K_w & 0 & 0 \\ \vdots & \vdots & \vdots & \vdots & \vdots & \vdots \\ 0 & 0 & K_w & \beta & K_s & 0 \\ 0 & 0 & 0 & 0 & K_s & \beta \end{pmatrix} \tag{3.3}$$

For semi-infinite SSH arrays, the amplitude of the topological edge state can be analytically expressed as [38]

$$\begin{aligned} a_{2m-1} &= (-r)^{m-1}\sqrt{1-r^2} \\ a_{2m} &= 0 \end{aligned} \tag{3.4}$$

where $r = K_w/K_s$ and $m = 1, 2, 3, ...$, with amplitude in even numbered waveguides vanishing. Beacuse of the chiral symmetry of the system, the eigenvalue of the modes take equal and opposite sign with zero mode eigenstate with eignevalue in the midgap of the eigenvalue spectrum. If the array is terminated with the weak coupling bond (waveguide 1 in Fig. 3.1) with total odd number of waveguides in the arrays, then the edge state mode (zero mode) with most of the power localized in terminated waveguide with zero power every even channels and vanishing field amplitude in odd channels, appears. Due to the SSH topological character, the zero mode or edge mode still

persists even when the coupling constants are perturbed from ideal design inevitable due to fabrication error of the device and it is robust against this perturbation.

In the non-reciprocal waveguide structures, the edge mode forces most of the light in the edge waveguide where as in the backward propagation direction, the edge mode is destroyed because of non-reciprocal effect and the eigenvalue of the otherwise midgap edge mode is pushed towards the eignevalue of one of the modes of the array. The power is then no longer localized and distributed to the other waveguides of the arrays isolating the edge waveguide. The principle is utilized here to realize optical isolator and the schematic depiction is shown in Fig. 3.7. However the non-reciprocal phase shift in the backward propagation direction has to be sufficient to change the eigenvalue of the midgap state to match to that of one of the modes of the array. The detail is discussed in Ch. 3.5.

3.3 Non-Reciprocal phase shift (NRPS) in gyrotropic waveguide

Magneto-optic garnet materials show non-reciprocal behavior as discussed in Chapter 2.2. In waveguide media of these materials, forward (FW) and backward(BW) propagating light have different propagation constants upon transverse magnetization

and acquire different phase for the same propagation length. This difference in propagation constant or phase shift is known as the non-reciprocal phase shift (NRPS). This effect arises due to light confinement in a gyrotropic medium lacking in spatial inversion symmetry and is induced by the coupling of longitudinal and transverse electric field components of the polarization rotation caused by the MO material. Many concepts and devices have been proposed both theoretically and experimentally exploiting this NRPS effect over the years on both gadolinium gallium garnet (GGG) and siliocon on insulator (SOI) substrates [39, 59]. Since garnet materials as cover on SOI waveguides offer more NRPS effect, focus these days has been shifted to integrating these materials on silicon platform for both shorter device length as well as silicon on-chip devices. However,Magnetic-garnets on SOI waveguides suffer higher propagation loss 40 dB/cm mainly because of absorption by secondary oxide phase formed during crystal growth processes [57, 90]. Whereas the propagation losses in epitaxially grown single-crystalline CeYIG films on lattice matched substrate is <10 dB /cm [91].

3.3.1 NRPS in Garnet on GGG waveguide media

In gyrotropic waveguides, only the TM mode suffers non-reciprocal phase change for in plane transverse magnetization unless a scheme of compensation wall (a magnetic wall that divides the rib waveguide into two regions of positive and negative Faraday

rotation) is implemented to achieve the non-reciprocal effect in TE mode with out-of plane magnetization [92–95]. Consider the geometry as shown in Fig. 3.2 where

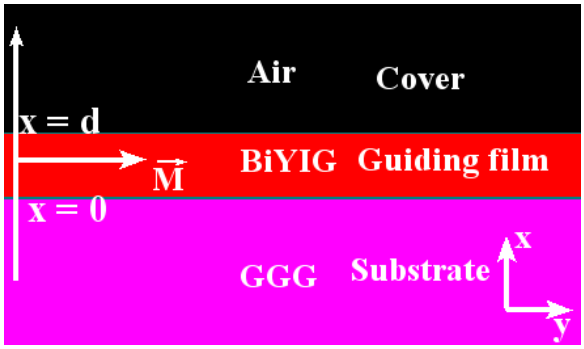

Figure 3.2: Cross-section of an planar Air/BiYIG/GGG waveguide

BiYIG or CeYIG is the waveguiding core layer on GGG substrate, air is the cover layer, and the magnetization is along the transverse direction (perpendicular to the propagation direction but parallel to the film plane). For loss-less isotropic magnetic-garnet layer transversely magnetized, the dielectric tensor is given by,

$$\hat{\boldsymbol{\epsilon}} = \begin{pmatrix} \epsilon_{xx} & 0 & i\epsilon_x z \\ 0 & \epsilon_{yy} & 0 \\ i\epsilon_x z & 0 & \epsilon_{zz} \end{pmatrix} \tag{3.5}$$

Where $\epsilon_{xx} = \epsilon_{yy} = \epsilon_{zz} = \epsilon$ the permitivity of the isotropic medium and $\epsilon_{xz} = \mathrm{g}$ is the magneto-optic gyrotropic parameter and is related to the Faraday rotation angle as $\mathrm{g} \approx 2n\theta_F/k_0$, where $n = \sqrt{\epsilon}$ is the refractive index of medium without magnetization and k_0 is the vacuum wave number. The sign of g only changes if the magnetization is reversed, but is independent of the direction of propagation as discussed in the

previous Chapter 2.2.1. For fundamental TM mode (TM_0), the electric field and magnetic field vectors for the wave propagating in Z direction with the propagation constant β are given as:

$$\begin{aligned} \vec{E} &= (E_x, 0, E_y)\exp[i(\omega t - \beta z)] \\ \vec{H} &= (0, H_y, 0)\exp[i(\omega t - \beta z)] \end{aligned} \tag{3.6}$$

Using Maxwell's equations, the wave equation in $\vec{H_y}$ can be derived as,

$$\frac{\partial^2 H_y}{\partial x^2} + \frac{\partial^2 H_y}{\partial y^2} + \frac{\partial^2 H_y}{\partial z^2} = \frac{n^2}{c^2}\frac{\partial^2 H_y}{\partial t^2} \tag{3.7}$$

Considering the wave amplitude doesn't change in y-direction and optical confinement takes place only in x-direction, i.e., $\frac{\partial H_y}{\partial y} = 0$, Eq.(3.7) can be simplified to

$$\frac{\partial^2 H_y}{\partial x^2} + \left({k_0}^2 \epsilon_{eff} - \beta^2\right) H_y = 0 \tag{3.8}$$

where

$$k_0^2 = \omega^2/c^2, \quad \epsilon_{eff} = \epsilon_{zz} - \epsilon_{xz}^2/\epsilon_{xx} = \epsilon - \mathrm{g}^2/\epsilon$$

The dispersion relation then can be solved using boundary conditions in substrate-core, and core-cover interfaces (also discussed in Chapter 4.2 as [96],

$$d\sqrt{k_o^2\epsilon_{eff}-\beta^2} = tan^{-1}\left[\frac{\epsilon_{eff}}{\sqrt{k_o^2\epsilon_{eff}-\beta^2}}\left(\frac{\sqrt{\beta^2-k_0^2\epsilon_c}}{\epsilon_c}-\frac{\beta \mathrm{g}}{\epsilon\ \epsilon_{eff}}\right)\right] \\ +tan^{-1}\left[\frac{\epsilon_{eff}}{\sqrt{k_o^2\epsilon_{eff}-\beta^2}}\left(\frac{\sqrt{\beta^2-k_0^2\epsilon_s}}{\epsilon_s}+\frac{\beta \mathrm{g}}{\epsilon\ \epsilon_{eff}}\right)\right] \tag{3.9}$$

where ϵ_c, ϵ and ϵ_s are the permitivity of cover (air), film (BiYIG or CeYIG), and substrate layers respectively, and d is the thickness of the guiding MO film. The

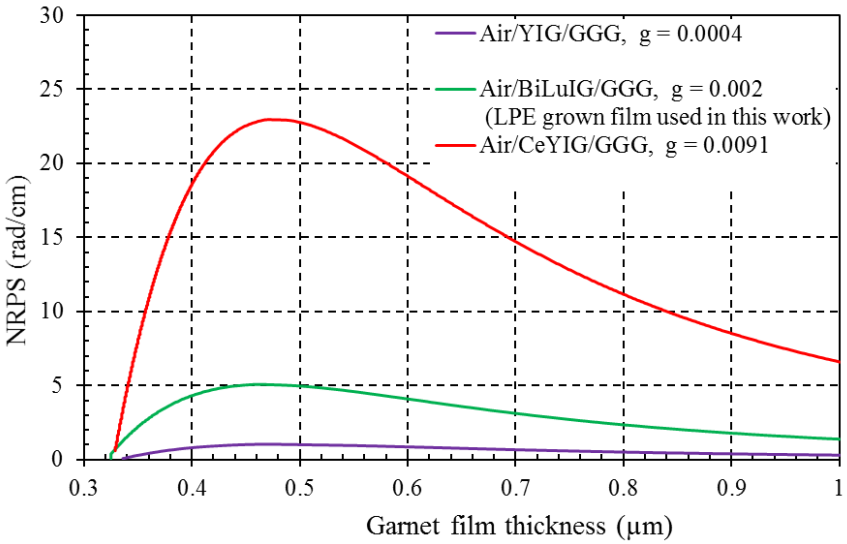

Figure 3.3: NRPS variation with garnet film thickness on Air/Garnet/GGG waveguide with parameters $\lambda = 1.55\mu m$, $n_s = 1.93$, $n_f \sim 2.22$ and $n_c = 1$

.

linear term of propagation constant β has opposite signs for forward $(+\beta)$ and backward propagation$(-\beta)$ propagation direction. SO the solution of the equation results

into different propagation constant for forward ($\beta_{forw.}$) and backward ($\beta_{backw.}$), i.e., $\beta_{forw.} \neq \beta_{backw.}$ propagation for the same thickness of the film. The NRPS is defined as

$$\text{NRPS}\,(\delta\beta) = \beta_{forw.} - \beta_{backw.} = \frac{2\pi}{\lambda}(n_+ - n_-) \tag{3.10}$$

where n_+ and n_- are the effective indices or mode indices of the fundamental (TM_0) mode in FW and BW direction with clockwise and anticlockwise helicities. The plot of (3.9) is as shown in Fig. (3.3) for Air/Garnet/GGG structure as a function of thickness of the guiding film of BiYIG for different values of the gyrotropy parameter that would vary for different amount of Bi/Ce substitution in the YIG garnet sublattices [8–17, 97, 98], and also on different film growth condition as well as the type of substrates chosen for growth. Reported values of the gyrotropy value g in the literature varies from 0.0004 (corresponding to FR of $\sim\ 214^0$ per cm for Pure YIG [67, 98, 99]) to 0.0091, (corresponding to FR value of 4800^0 per cm for CeYIG on GGG substrates [13]). The gyrotropy value of g = 0.002 corresponds to the measured Faraday rotation $938^0/cm$ of the LPE grown BiLuIG ($Bi_{0.64}Lu_{2.23}Fe_{4.2}Ga_{0.8}O_{12}$) garnet film used in this work on CMZ:GGG [$(Gd_{2.68}Ca_{0.32})\,(Ga_{1.04}Mg_{0.32}Zr_{0.64})\,Ga_3O_{12}$] substrate with index of refraction as measured from ellipsometer as 2.22 and 1.93 for film, and substrate, respectively, at 1550 nm wavelength. NRPS is maximum at 0.49 μm thick BiLuIG film. For that reason all the waveguides fabricated in this work were thinned down to about 500 nm from their original thicknesses of 2 μm in the 2 inch wafer.

3.3.2 NRPS in garnet on silicon on insulator (SOI) waveguide media

When a garnet layer is used as the cover layer on silicon (Si), the guiding film and SiO_2 as the substrate (Fig. 3.4), the index contrast is higher between substrate-film and film-cover interface than in the BiYIG ($n \approx 2.22$) on GGG ($n \approx 1.45$) waveguide geometry. The waveguide modes are highly confined in the film region on SOI waveguide because of this high gradient in indices. Similar to above Eq. (3.9),

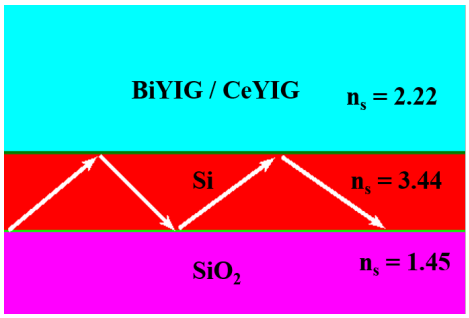

Figure 3.4: Cross-section of an planar Garnet/Si/SiO_2 waveguide

the dispersion relation for TM_0 mode in "Garnet/Si/SiO_2" structure can be derived as [100],

$$d\sqrt{k_o^2\epsilon_f - \beta^2} = tan^{-1}\left[\frac{\epsilon_f}{\sqrt{k_o^2\epsilon_f - \beta^2}}\left(\frac{\sqrt{\beta^2 - k_0^2\epsilon_{eff}}}{\epsilon_{eff}} + \frac{\beta \mathrm{g}}{\epsilon_f\ \epsilon_{eff}}\right)\right] + tan^{-1}\left[\frac{\epsilon_f}{\sqrt{k_o^2\epsilon_f - \beta^2}}\left(\frac{\sqrt{\beta^2 - k_0^2\epsilon_s}}{\epsilon_s}\right)\right] \tag{3.11}$$

The variation of NRPS in Garnet/Si/SiO_2 planar waveguide structures as a function of Si film thickness for different garnet materials on top with three different gyrotropy parameter values 0.0004, 0.002, and 0.0091 (the same values used in the plot of Fig. 3.3 but on SOI substrate) is as shown in Fig. 3.5. The NRPS has its peak value

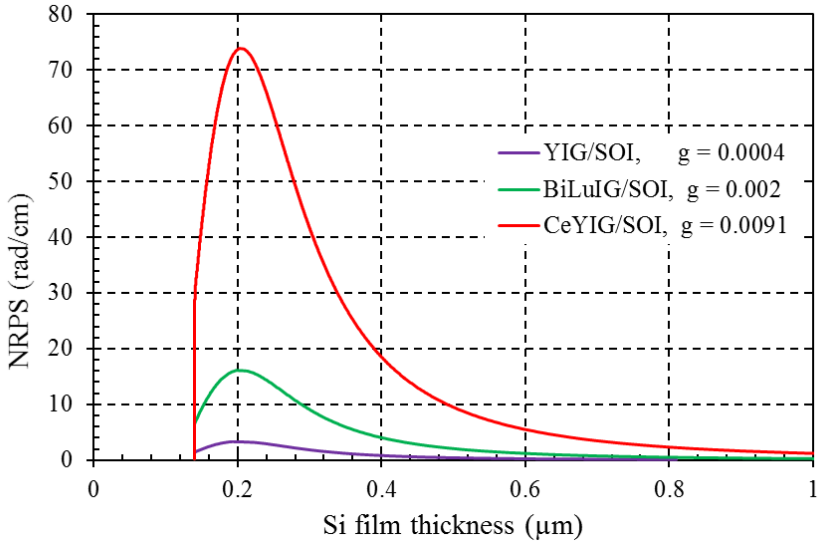

Figure 3.5: NRPS variation with Si thickness on Garnet/Si/SiO_2 planar waveguide with parameters $\lambda = 1.55\mu m$, $n_s = 1.45$, $n_f = 3.47$ and $n_c \sim 2.22$

.

at $\approx 0.2\ \mu m$ Si film thickness and increases linearly with higher gyrotropic values (see inset of Fig.3.13). Notice that the NRPS value in Garnet/Si/SiO_2 structure is about 3× larger than in Air/garnet/GGG for the same gyrotropic material used [100]. However it is used as guiding film in the former and as upper cladding (cover) in the next.

3.4 Magnetization Gradient induced gyrotropic gradient

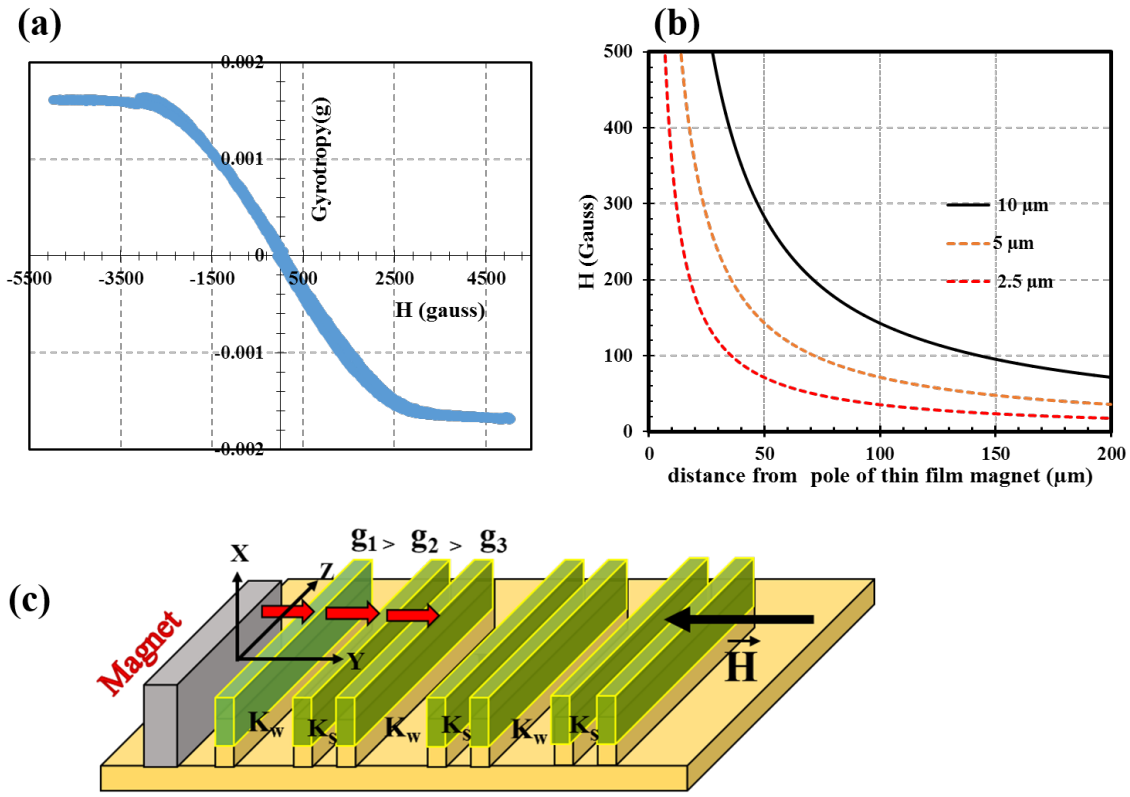

Figure 3.6: Illustration of scheme of achieving gyrotropic gradient with the field due to thin film magnet below saturation magnetization of the garnet material. (a) Hysteresis curve of gyrotropy, linear dependancy with applied field (H) below saturation.(b) Magnetic field variation with distance from pole of a thin film SmCo magnet ($4\pi M_{sat.} = 9000\ Oe$) of three different thicknesses 10 μm, 5 μm and 2.5 μm with steeper field gradient for thinner magnet. (c) schematic of waveguides in the arrays experiencing different gyrotropy because of their positions from the magnet.

Tuning of propagation constants plays crucial role in the system of non-reciprocal

waveguides arrays designed to manipulate light differently in the FW and BW directions of propagation. One way of doing that is by creating the gradient in the magnetic field due a thin film magnet. As the field due to thin-film magnet has almost exponential decay of the field with distance (Fig. 3.6 (b)) [22, 31], the waveguides in the arrays at different distances from the magnet can have different gyrotropic values (see Fig. 3.6 (a)) and thus differnt NRPS, even though they are made up of the same garnet material. This is valid only below the saturation field, above which all are magnetized equally. For example, in Fig. 3.6 (c), the garnet material of waveguide closest to the magnet gets higher g value and others farther away gets lesser g values. Fabricating an integrated thin film magnet closer to the one side of the array or directly on top of edge most waveguide can fully magnetize the waveguide closest to the magnet leaving others partially magnetized. Alternatively, a reverse field can also be applied to nullify the effect in remaining waveguides other than the closest to the thin film magnet. Magnetizing only the edge waveguide or atleast creating high gradient in the gyrotropy value exploiting non-linear decay of field from thin film magnet with distance is one of the design aspects of this work based on topological edge-mode as discussed further in the following sections.

3.5 Design and operating principle of Su-Shrieffer-Heeger (SSH) edge modes-based optical isolator

The proposed device consists of a seven-waveguides array Su-Shrieffer-Heeger (SSH) construction, as depicted in Fig. 3.7. SSH constructions create a topologically protected edge state mid-gap in the photonic band structure generated by the waveguide array [38, 81, 83, 84]. SSH edge states form in the coupled waveguide arrays with alternating strong and weak coupling constants $K_s$and K_w, respectively, (i.e. $K_s > K_w$) and an odd number of waveguide channels [38]. This construction gives rise to a topologically protected normal mode propagating on one edge in the array. The topologically protected state results from the alternating inter-waveguide coupling constants and prevents the light from diverging into the bulk of the array. The ratio K_w/K_s determines the level of protection of the edge state against departures from uniformity in K_s or K_w across the array, or in propagation constants in the individual array channels [81]. The nonreciprocal magneto-optic effect induces a change in propagation constants in the backward direction that destroys the edge state, as discussed theoretically in [38]. Our measurements show that this device delivers < 2 dB of delocalization of optical power from the edge-state, and better

than 25 dB of extinction in the farthermost channel from the edge waveguide, in the three arrays studied. Fig. 3.7 shows schematically the beam propagation structure based on this principle.

The experimental results presented below report the edge-state selectivity corre-

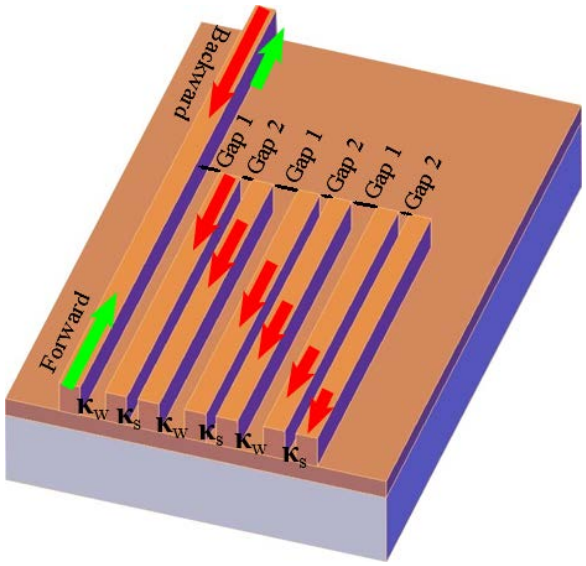

Figure 3.7: Schematic of an SSH array, green arrows indicate the edge mode state during FW propagation where most of the power is localized in edge WG and red arrows represent the bulk mode state for BW reflected light where light undergoes discrete diffraction to the other waveguides

.

sponding to the power reaching the output channel in the forward direction when light is coupled to the edge state channel vs other channels in the SHH array. Spreading of the power in other channels from the edge state can be minimized by engineering metallic optical absorbers as discussed in [38], without affecting the forward output power.

Liquid-phase-epitaxy(LPE)-grown iron-garnet core waveguides on lattice-matched

garnet substrates were used to fabricate the devices reported in this work. These generally generate lower power-absorption losses than through other fabrication techniques [8, 9, 27, 56, 66, 67, 101]. At the same time, they do not deliver as large a nonreciprocal phase shift [30] as sputter- or pulsed-laser-deposited iron garnets on silicon waveguides [102] for two reasons. First, the level of bismuth or cerium substitution, needed to enhance the magneto-optic gyrotropy over that of pure yttrium iron garnet (YIG), is lower in LPE-grown films due to substitutional saturation conditions in the growth melt. Second, having the iron garnet as a cover layer on high-index core films such as silicon, generates a larger NRPS effect as a result of magneto-optic helicity biasing in the evanescent tail. Conclusions about the performance of higher magneto-optic gyrotropy materials are also drawn from our experimental data.

The footprint of the SSH arrays depends on the strength of the magneto-optic gyrotropy parameter in the Bi-substituted iron garnet film, and on the K_w/K_s ratio in the SSH structure. Nonreciprocal power transfer between the two channels in opposite propagation directions is a function of the corresponding nonreciprocal phase shift. A stronger coupling constant between the channels requires a stronger gyrotropy parameter for smaller footprints, full power transfer in the backward direction and optical revival in the edge-state channel in forward propagation. These gyrotropy values range from $\sim$ 0.0003 to 0.002 depending on the level of bismuth substitution in the iron garnet at an 1.55 μm wavelength. Higher values

~ 0.0086 (upto 0.0091 [13]), are attainable in Ce-substituted iron garnets [8, 9, 11, 27].

3.6 Fabrication and device specifications

The topological edge state waveguide arrays were fabricated on LPE-grown films of bismuth-substituted lutetium iron garnet film (Bi:LuIG) with composition $Bi_1Lu_2Fe_{4.3}Ga_{0.7}O_{12}$ on (100) gadolinium gallium garnet (GGG). The schematic of the process flow from thinning the film to e-beam lithography (EBL)steps is shown in 3.8. The iron garnet films were initially etched down to $\sim$ 500 nm-thickness (little more than 490 nm thickness at which NRPS is maximum, see Fig. 3.3 from thick virgin films by wet etching in ortho-phosphoric acid at 150^0 C and cleaned with deionized (DI)water . The etching rate of both ZEP e-beam resist (3.1 nm per minute) and the BiLuIG films (2.6 nm per minute) were first characterized in the Ar ion milling system to find the proper thickness of the resist, as too thick resist may affect on the resolution of the pattern and too thin would not serve as the mask while etching down 250 nm deep. As the desired etch depth was 250 nm, about 350 nm thick ZEP positive e-beam resist was spin coated on the film at spin speed of 4000 rpm (revolution per minute), acceleration of 1500 rad/cm^2 and total time of 45 sec. The resist was then baked at 180^0C for 3 minutes. A 30 nm-thick gold layer was sputter-deposited on top of resist to avoid electron beam charging while writing on the insulating Bi:LuIG

film. Vistec EBPG5000+ e-beam tool was used to write the patterns on the resist with exposure area dose of 150 $\mu C/cm^2$ with 5 nA beam current for which beam spot size is 5 nm. 8 mm long waveguides arrays were formed by the beam through multiple stitching at a writing field of 500 $\mu m \times 500\ \mu m$. After the e-beam exposure, the

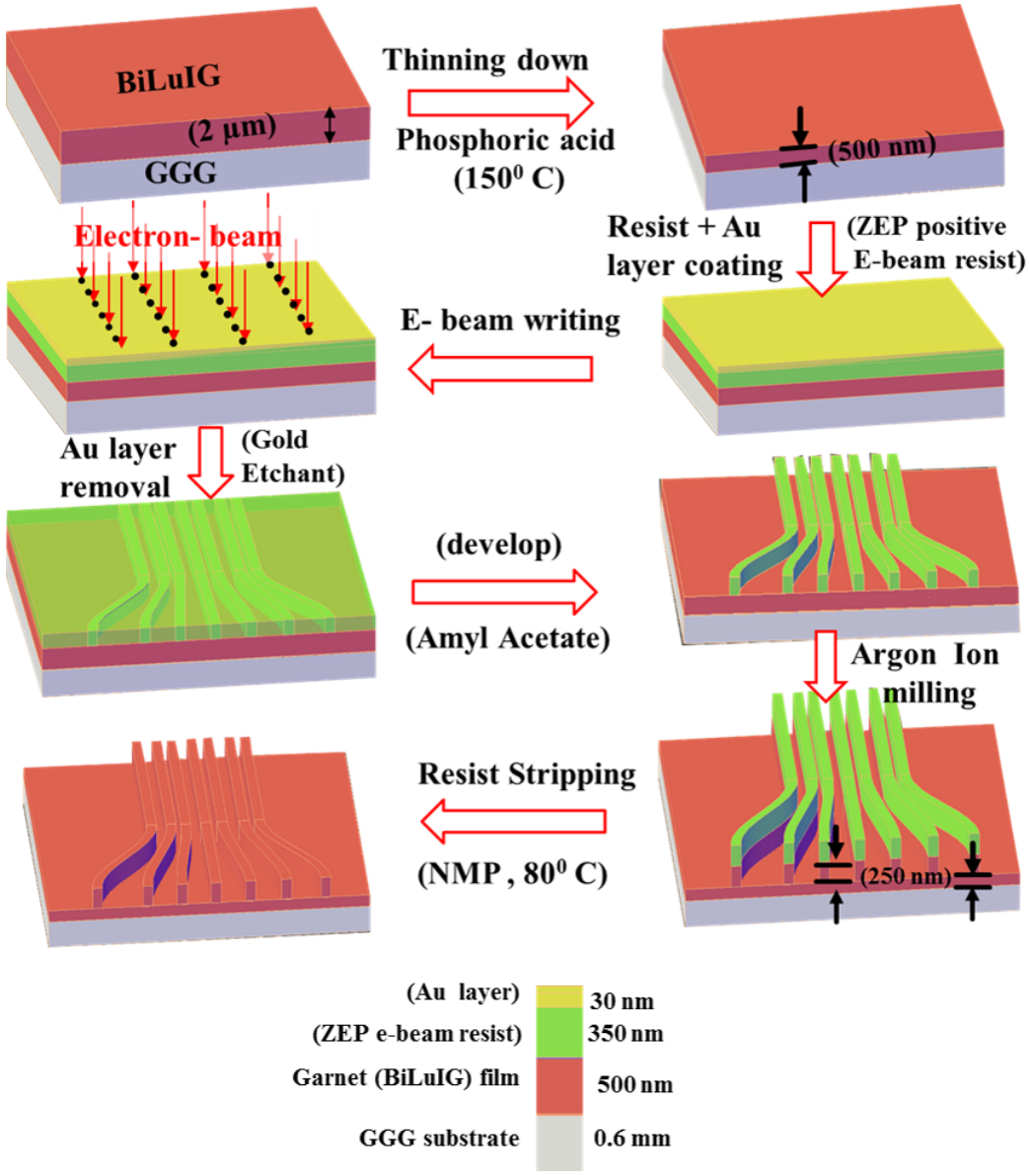

Figure 3.8: SSH array fabrication process flow with electron-beam lithography (EBL).

thin gold layer was removed by wet etching in gold-etchant for 1 minute and rinsed with DI water. The exposed resist was then developed in amyl acetate solution for 1 minute and rinsed with isopropyl alcohol (IPA). These patterns were then transferred into the Bi:LuIG film by argon-ion beam milling (Nanoquest II ion milling system from IntlVac) using slow milling recipe with the following beam parameters; beam Voltage =200 V, Beam current = 70 mA, Accel. Voltage =24 V, and Forward power of plasma = 73 Watt. The sample holder was rotated at 10 rpm and cooled at 6^0 C throughout the process for uniform etching, tilted at 75^0 to the ion beam to prevent re-deposition on the side walls of the resist structure. 225 nm waveguide ridges were obtained after 80-minutes of milling. The remaining resist coating was removed by soaking in N-methyl pyrrolidine (NMP)for half an hour heated to 80^0 C.

The design and fabricated device dimensions are tabulated below in Table 3.1, for

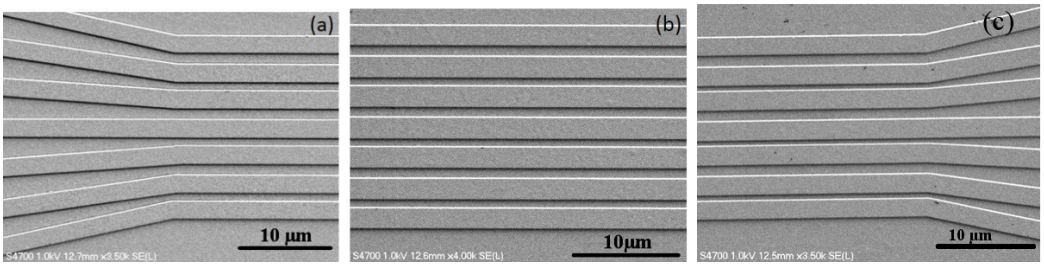

Figure 3.9: SEM images of a fabricated SSH array: (a)and (c) are the input and output regions, and (b) is the coupling region.

each of the arrays studied here. Scanning-electron micrographs (SEM) images of the input and output regions (a) and (c), and the middle coupling region (b) are shown in Fig. 3.9 for one of the arrays. Ancillary input and output channels (Fig.3.9 (a))

were fabricated to facilitate separate coupling and probing of each.

The fabricated channel-waveguide widths depart from the 2 μm design width. Deviations from design are nearly uniform throughout the arrays and less than 100 nm. As we shall see from the performance results below, these departures from device specification do not destroy the topological edge state.

Table 3.1
Dimensions of waveguide's widths and gaps in design and post-fabrication (post-fab.)

WG no.	W/G* (μm)	**SSH array 1**		**SSH array 2**		**SSH array 3**	
		design	post-fab.	design	post-fab.	design	post-fab.
1	W	2	1.772	2	1.786	2	1.762
	G	1	1.127	1.2	1.294	1.2	1.365
2	W	2	1.883	2	1.88	2	1.828
	G	0.8	0.892	0.9	0.973	1	1.112
3	W	2	1.858	2	1.871	2	1.861
	G	1	1.065	1.2	1.257	1.2	1.308
4	W	2	1.895	2	1.89	2	1.713
	G	0.8	0.855	0.9	0.966	1	1.035
5	W	2	1.895	2	1.884	2	1.61
	G	1	1.065	1.2	1.264	1.2	1.122
6	W	2	1.883	2	1.876	2	1.619
	G	0.8	0.917	0.9	0.95	1	0.951
7	W	2	1.821	2	1.851	2	1.741

* W= width of a waveguide, G = Gap between two adjacent waveguides.

3.7 Power selectivity and insertion loss measurements and performances

SSH array structures concentrate most of the propagating optical power in the edge channel corresponding to the topological edge state when light is coupled into that channel. When light is inputted into any of the other channels, they distribute power throughout the whole array, even when coupled into the farthermost channel on the opposite end of the topological structure.

This operation is verified in Fig. 3.10 insets, which shows infrared (IR) CCD camera intensity profile images of the power from the seven output channels captured by the camera for different input locations. Each row corresponds to an input into successive waveguides, with the topological edge-state output inside the red frame at the top of each panel. Images for the three arrays are displayed for TM and TE mode inputs, showing that all the arrays perform as topological edge-state structures for both waveguide modes. Fig. 3.10 plots the experimentally-measured intensity profiles and simulated counterpart results obtained by using beam-propagation method (BPM) simulation of these arrays. It can be seen that the two profiles are quite similar. These BPM simulations confirm that the fabricated arrays perform as expected for topological edge-state structures. Light coupled into the edge waveguide remains confined to the edge, whereas light inputted into other channels produces

beams that diverge throughout the array, as shown in Fig. 3.10.

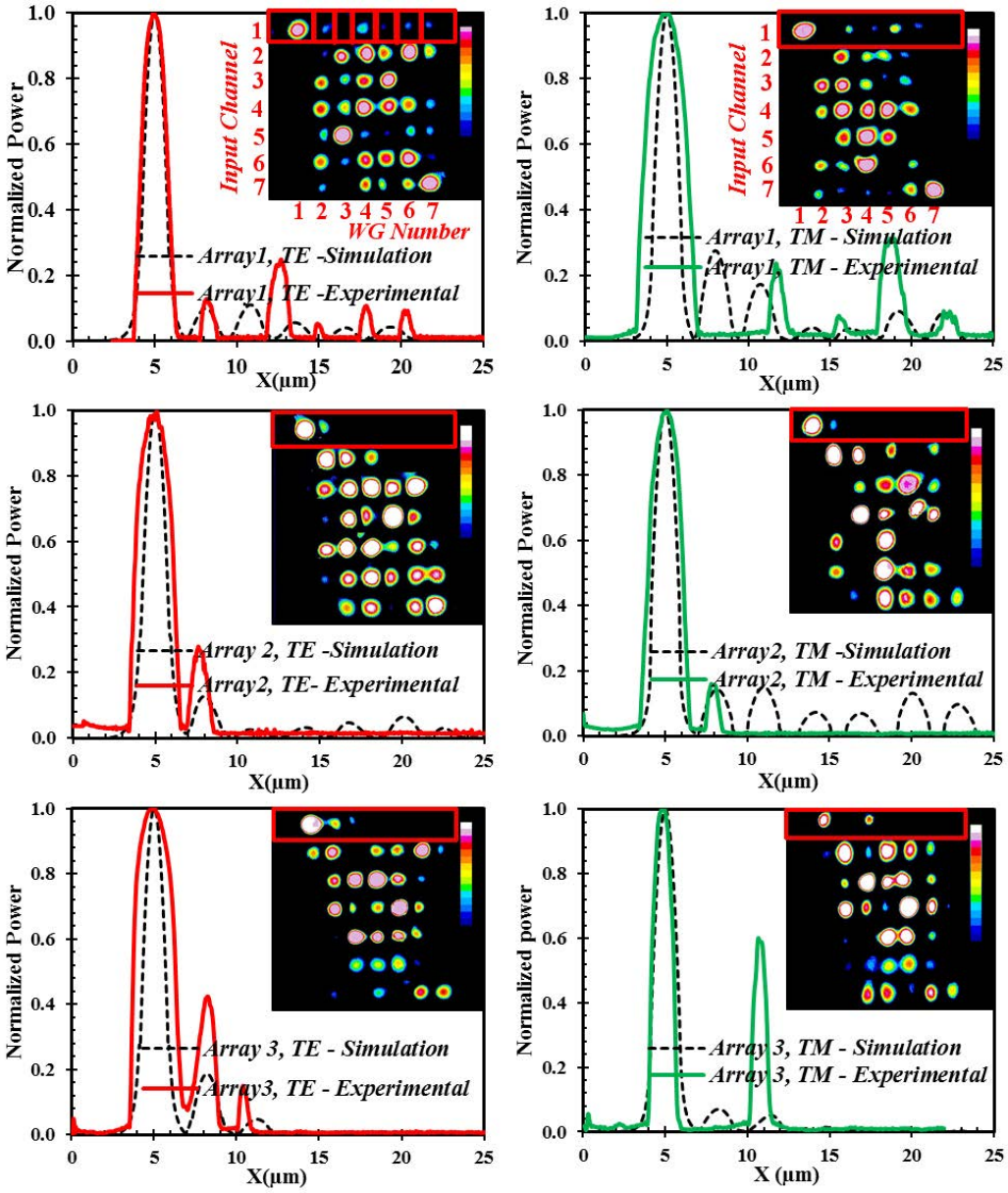

Figure 3.10: Simulation vs experimental normalized output power plot of edge states for three SSH arrays under study for TE and TM modes. Insets are the IR CCD camera intensity profile images of the respective arrays when input light is coupled to WG no. 1 (top row profile enclosed by rectangle- edge state) to WG no. 7 (bottom row profile). Differences between experimental and simulated edge-state intensity profiles are ascribed to fabricated device dimensions deviations from design

BPM-simulated edge-state propagation for the three SSH designs are also shown in Fig. 3.11 (a), (b) and (c). Each simulated waveguide structure is $2\mu m$ wide, 500 nm in ridge height with 250 nm of slab, in agreement with the design, but differing somewhat from the actual fabricated arrays. The coupling coefficients in the SHH model are controlled by the separation between the waveguides. The three SSH arrays studied here are defined by the two different alternating gaps (a) 1 μm and 0.8 μm in array1 (b) 1.2 μm and 0.9 μm in array 2 and (c) 1.2 μm and 1 μm in array 3. The strongest coupling coefficient values in the above arrays are 13.8, 10.4 and 8.0 cm^{-1} respectively.

Isolator-function operation is simulated in Fig. 3.11 (a′), (b′), and (c′) exhibiting almost complete power extinction in the edge waveguide for nonreciprocal phase shifts $\Delta\beta^{nr}$ 26.8 cm^{-1}, 24.1 cm^{-1} and 18.5 cm^{-1}, respectively, in the corresponding edge waveguide. This approximate extinction occurs after 2.5- to 4-mm propagation lengths.

The performance of the topological-edge-state is measured by butt-coupling wavelength light from a lensed optical fiber into polished facets of the topological-edge waveguide. For analytical purposes, light from the fiber is also coupled into each of the other channels, for both TE and TM input modes. Infra-red (IR) charge coupled device (CCD) camera images are also taken of the intensity distribution profiles as shown in Fig. 3.10 insets. These images evince how the light remains at the topological edge or gets dispersed into the other channels, depending on the

coupling, and on each particular array.

In order to characterize the performance of the fabricated structures, the power

Table 3.2
Optical power measurement on three fabricated SSH arrays for both TM and TE modes

Fiber coupled WG No.	TE Mode Total (μWatt)	TE Mode Edge WG 1 dB	TE Mode Edge WG 7 dB	TM mode Total (μWatt)	TM mode Edge WG 1 dB	TM mode Edge WG 7 dB
Array 1 , Measured Power						
1	1.0	**-1.0**	-25.6	3.776	**-1.2**	-21.0
2	3.487	-15.1		2.491	-13.9	
3	2.254	-10.8		2.442	-12.2	
4	4.942	-12.1		10.008	-16.1	
5	3.607	-11.6		12.593	-17.3	
6	3.577	-17.8		4.166	-14.3	
7	3.137	-18.6		0.639	-11.9	
Array 2 , Measured Power						
1	3.603	**-0.1**	-23.0	1.228	**-2.9**	-22.0
2	5.904	-15.0		1.033	-13.5	
3	4.516	-18.1		7.673	-27.2	
4	8.453	-28.1		5.399	-15.2	
5	5.355	-21.7		3.286	-24.1	
6	5.513	-27.6		1.823	-22.4	
7	2.590	-17.1		0.395	-13.3	
Array 3 , Measured Power						
1	1.360	**-0.7**	-28.6	0.932	**-5.3**	-25.8
2	0.566	-6.9		0.364	-1.6	
3	1.217	-15.9		1.010	-13.2	
4	1.090	-21.7		51.095	-14.0	
5	1.223	-22.7		0.505	-11.3	
6	0.029	-21.1		0.025	-0.2	
7	0.655	-19.1		0.078	-23.6	

coming out of the edge state channel (waveguide number 1 in Fig. 3.10) is compared to the incident power, as defined below, for light coupled into channels 1 to 7. This

actually measures the degree of localization of the edge state light when coupled to the edge state channel vs any other channels as input.

Incident power is defined as the sum of the powers coming out of all of the channels in the array. This definition of incident power folds out mode conversion and Fresnel losses at the input facet. It also does not account for optical absorption and scattering losses in the array channels. This configuration also allows us to define insertion loss as the ratio of the light emerging out of topological edge channel divided by the total incident power, as defined above.

Table 3.2 tabulates these results for both TE and TM modes of input excitation.

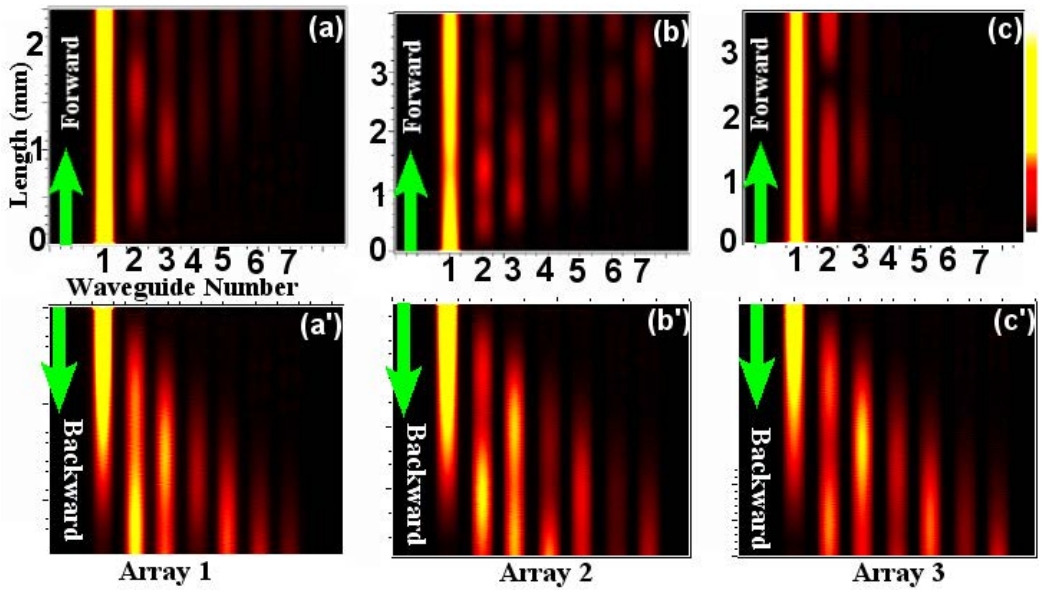

Figure 3.11: BPM simulated topological edge states in three SSH model waveguide arrays for forward and backward propagation; (a), (b) and (c) – forward propagation ; (a′), (b′) and (c′)– backward propagation for the three arrays, respectively

It also tabulates the power emerging from the topological edge channel (waveguide

1) and the opposite outermost channel (waveguide 7) when light is coupled into waveguide 1, and the power in the edge waveguide 1 when the inputted into the other channels 2 to 7. Less than 1 dB of power is distributed among other waveguides in all three arrays in TE modes resulting in up to 28.6 dB of extinction in the outermost channel 7 when the light is mainly localized in the edge mode. In TM mode, the delocalization of the edge mode is below 3 dB in two of the arrays. In array 3, the higher delocalization value (5.3 dB) is attributed to damage to the device during the fabrication process, that also results in relatively lower power transmission compared to other arrays in TM mode. Power extinction in the outermost channel is measured as 25.8 dB in this case. Noticeably there is very low power coming out of the edge

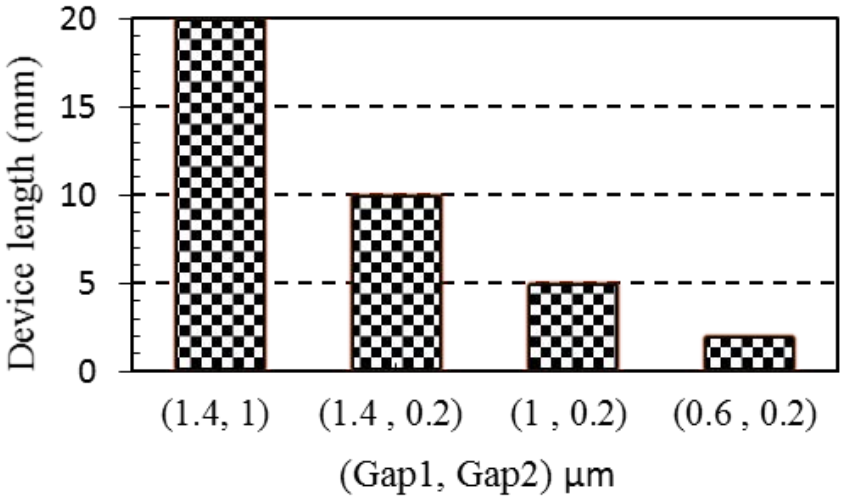

Figure 3.12: Device length for different coupling coefficients as controlled by separation between waveguides: gap1 and gap2 corresponding to the weaker and stronger coupling coefficients K_w andK_s, respectively.

WG 1 in the cases when the input is launched from all other waveguides. This can also be seen clearly from 2nd to 7th row profiles of the output in the insets to

Fig. 3.10. The experimentally measured edge-mode profiles closely resemble their respective BPM intensity profile for both TE and TM modes, also shown in the same figure. This distinctly differentiates topological edge modes from the non-topological modes.

The fabricated SSH arrays studied here are 7 mm long. However the device length can be shortened by increasing the coupling coefficients, thus reducing the distance between the optical channels. Devices can be made sub-mm in length by reducing channel gaps to the shortest limit presently allowable by fabrication techniques, below 100 nm via e-beam lithography and plasma etching. The preservation of power in the edge state channel is highest when the contrast between the values of the coupling coefficients is greatest [101] . So there is a trade off between device length and the localization of edge mode power. As shown in Fig. 3.12 the device length shortens from 20 mm to 10 mm when the inter-channel gap corresponding to is reduced from 1 μm to 200 nm while keeping the other gap at 1.4 μm. The device length gets further reduced to 2 mm when the gap corresponding to is 0.6 μm.

3.8 Challenges

Full implementation of an optical isolator of this type requires $\Delta\beta^{nr} \geqslant K_s$. In our case $\Delta\beta^{nr} = 4 \ \ \text{cm}^{-1}$ while K_s is 26.8 cm^{-1}, 24.1 cm^{-1} and 18.5 cm^{-1} for the

three arrays studied here. So the above condition is not satisfied. To incorporate this into a working optical isolator, the inter-channel gap for would have to be $\geq 1.3\mu m$, requiring a device longer than 20 mm.

Fig. 3.13 plots coupling coefficient as a function of channel separation for the mate-

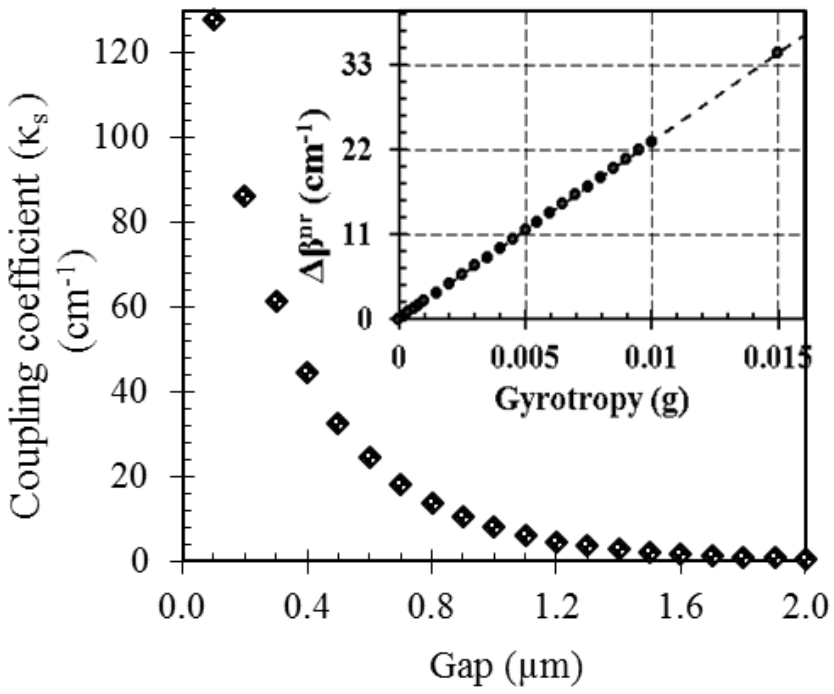

Figure 3.13: Coupling coefficent variation with separation between Bi:LuIG channels. Inset shows the value of magnetic gyrotropy needed for $\Delta\beta(nr \geq K_s$ so that delocalization (isolation function) occurs in the backward direction

rial parameters used in this work. The inset to Fig. 3.13 gives the required gyrotropy parameter of the magneto-optic film needed to produce the non-reciprocal phase shift required to delocalize the light from the edge waveguide for backward propagating light. It can be seen that reducing the coupling coefficient through an increase in

inter-channel separation increases the device length to $>$ 20 mm for a gap greater than 1.3 μm. Conversely, one could attain larger values of with Ce-substituted iron garnets [8] or by utilizing double layers of iron garnets [103] on GGG substrates with as high as 40 cm^{-1}. With Ce-TIG covers on SOI waveguides, values become as large as 70 cm^{-1} [102] and device footprints of $\sim$ 1 mm are feasible.

However magnetic-garnet films deposited on SOI waveguides suffer from higher propagation losses compared to LPE grown garnet core waveguides. Reducing the isolator footprint to the smallest levels allowed by present-day fabrication technologies (sub-100 nm gaps) would produce footprints of $\sim$ 1 mm. This requires iron garnet materials development with correspondingly higher nonreciprocal phase shifts. For example, using 100 nm gaps for stronger coupling requires 128 cm^{-1}, corresponding to gyrotropy parameters of 0.05 (not technologically achieved yet!) for the magneto-optic film.

Topological edge-state devices such as discussed here require the magnetization of the garnet on the edge channel opposite to that of the rest of the array [102]. This calls for localized magnetic fields and relatively large magnetic field gradients near edge [102]. Such conditions could be implemented by depositing a thin ($\sim 10\,\mu m$) samarium-cobalt (SmCo) films with an intermediate buffer layer on top the array [22]. Other options entail thin current carrying conducting wires, as thin as 20 or 30 μm and cannot withstand high enough currents to achieve the required saturation fields, unless superconducting. Tests in our laboratory with 20 μm -thin gold wires

were limited to currents of 0.5 Amps. Alternative electromagnet designs to achieve in plane saturation field with current as small as 0.25 Amps have been discussed by other authors [56].

3.9 Conclusions

We have experimentally measured and analized the degree of localization of edge modes in SSH arrays designed for LPE-grown BiLuIG films on GGG substrate. A high degree of optical localization was observed for both TE and TM input excitations with less than 2 % of optical input power spread in the remaining 6 waveguide channels out of 7 channels in the arrays fabricated. The edge states modes is clearly distinct from the other array modes favouring isolation of the edge channel which is the motivating factor towards realizing this effect in a fulfledged optical isolator. The device length could be reduced to $\sim$ 1 mm by working with the waveguide film-core configuration yielding a high non-reciprocal phase shift.

Chapter 4

Nonreciprocal Electromagnetic Spin-Orbit Coupling in Magneto-optic Materials

4.1 Introduction

[1]The spin-orbit interaction (SOI) of light has been the subject of extensive studies in the last few years [105–115]. Recent experiments have demonstrated strong directional coupling of circularly polarized light (optical spin) in nanophotonic waveguides, where

[1]The material content in this article is published in Nature scientific reports, 7(2017) [104] and reproduced here under the license of creative commons (see appendix B for detail.)

the optical helicity determines the direction of optical flow of the in-coupled light [115]. That is, transversely polarized light acting on nanoparticles on the waveguide cladding can be made to excite beams (optical orbital angular momentum) propagating normal to the incoming wave.

The propagation direction of the guided mode being determined by the helicity of the incoming light. Unidirectional surface-plasmon excitation has also been observed in spatially symmetric structures, the surface wave direction being switchable with the sense of circularly polarized optical excitation [110]. Other studies have demonstrated optical helicoidal beams, where light in a whispering gallery or ring resonator is made to emit waves possessing orbital angular momentum in free space, as illustrated schematically in Fig. 4.1 [111]. Finally, spin-to-orbital angular momentum conversion in tightly focused non-paraxial optical fields in free space has also been demonstrated, where circularly polarized light without a vortex actually exhibits circulating orbital momentum [114].

This type of spin-orbit interaction in optical wave propagation paves the way to spin-controlled photonics. The use of transverse spin angular momentum and the coupling of transversely propagating circularly polarized beams to waveguide and surface plasmon modes permits selective directional addressing of guided light and quantum states, and enriches the store of spin-dependent tools available to integrated and nano-photonics [109–112, 115].

However, the above studies have not addressed the effects of magneto-optic non-reciprocity on optical spin-orbit coupling, nor ways to induce such coupling by magnetic means. The analysis we present here discusses the generation of optical orbital angular momenta induced through magneto-optic spin-orbit coupling. It analyzes the effect of non-reciprocity on spin-induced transverse optical momenta, as well as magnetization tuning and magnetization reversal effects on unidirectionally spin-induced orbital angular momenta normal to the optical spin. It is known that transverse elliptical polarization of a given helicity occurs in the evanescent tail of optical waveguides, that transversely magnetized magneto-optic waveguides evince a nonreciprocal phase shift, and that the Faraday effect rotates the polarization of light. Yet the effect of magneto-optic media on the orbital angular momentum shifts in unidirectionally-coupled light upon transverse optical spin reversal, the effect of Faraday rotation upon spin angular momentum conversion and the nonreciprocal transfer to orbital

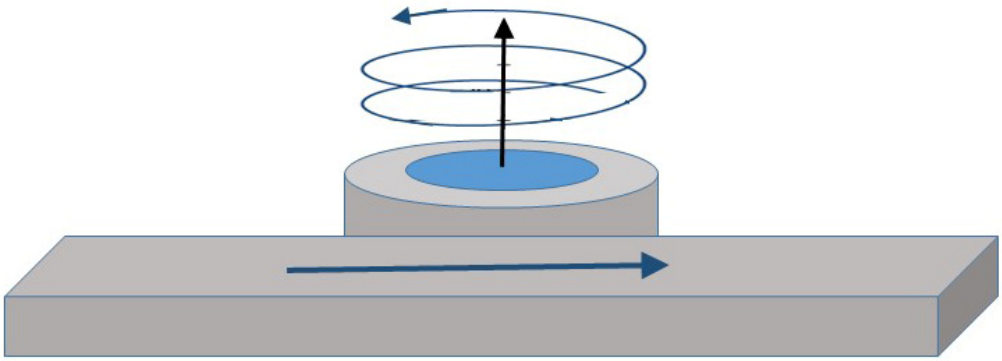

Figure 4.1: Schematic depiction of a micro-ring optical resonator coupled to a feeder waveguide used to emit helicoidal waves possessing orbital angular momentum into free space.

momenta due to electromagnetic spin-orbit coupling, and the magnetic tuning of spin-orbit coupling and its effect on the induced orbital angular momenta have not been addressed. It is these phenomena that are explored in this chapter.

Thus, we address the spin-dependent magnetization control of the propagation direction and induced orbital angular momenta. Circularly-polarized beams of a given helicity evanescently-coupled to an optical waveguides in the presence of a transverse magnetic field to the optical channel, can be made to switch phase-velocity, alter orbital angular momentum, or cancel unidirectional propagation upon magnetic field tuning, reversals or rotations. Transverse optical spin is a physically meaningful quantity that can be transferred to material particles [105–107, 112–115]. This has potentially appealing consequences for optical-tweezer particle manipulation, or to locate and track nanoparticles with a high degree of temporal and spatial resolution [109]. Thus, developing means of control for the transverse optical spin is of practical interest.

We address the latter question for spin and orbital angular momenta, show that their magnitudes and sense of circulation can be accessed and controlled in a single structure, and propose a specific configuration to this end. Explicit expressions for these physical quantities and for the spin-orbit coupling are presented. Moreover, we develop our treatment for nonreciprocal slab optical waveguides, resulting in a different response upon time reversals.

Consider the behavior of evanescent waves in a magnetic garnet cladding on silicon-on-insulator waveguides, as in Fig. 4.3. The treatment we present deals with transverse-magnetic (TM) mode propagation. This allows us to obtain explicit expressions for nonreciprocal transverse spin momenta and angular momenta and to propose a means for magnetically controlling these objects, with potential application to integrated optical vortex beam emitters, optical tweezers and quantum computation [112]. The conversion of transverse-spin to orbital angular momenta through spin-orbit coupling relies on TM to transverse-electric (TE) mode conversion. We show that, in this case, mode conversion via Faraday rotation, channels electromagnetic spin-inducing linear momenta into orbital angular momenta that can then be converted into free-space helicoidal beams.

4.2 Theoretical background

In 1939, F. J. Belinfante introduced a spin momentum density expression for vector fields to explain the spin of quantum particles and symmetrize the energy-momentum tensor [115]. For monochromatic electromagnetic waves in free-space, the corresponding spin linear-momentum density reads

$$\vec{p}_B = \frac{1}{2}\vec{\nabla} \times \vec{s}_B \tag{4.1}$$

with a time-averaged spin angular-momentum density

$$\vec{s}_B = \mathrm{Im}\frac{1}{2\omega}\left(\epsilon_0 \vec{E}^* \times \vec{E}\right) \tag{4.2}$$

ω is the optical frequency and ϵ_0 the permittivity of free-space [108] . The optical spin-angular-momentum density of Eq. (4.2) is derivable from the expression for the total electromagnetic angular momentum in terms of the Poynting vector [116],

$$\int \vec{r} \times \left[\epsilon_0 \mu_0 \vec{E} \times \vec{H}\right] \, d^3 r \tag{4.3}$$

where $\epsilon_0 \mu_0 \vec{E} \times \vec{H}$ is the electromagnetic momentum density, and $\vec{A}$ the vector potential. Upon integration by parts, the integrand in Eq. (4.3) acquires an "intrinsic" term, $\epsilon_0 \vec{E} \times \vec{A}$, independent of radius vector $\vec{r}$ except, implicitly, through the field components. This term is usually associated with the electromagnetic spin density [116] . The remaining term

$$\sum_{i=x,y,z} E_i \left(\vec{r} \times \vec{\nabla}\right) A_i \tag{4.4}$$

corresponds to the orbital angular momentum density. This spin angular momentum, in its transverse electromagnetic form has merited much attention in recent years, as it can be studied in evanescent waves [105–107, 114] . There are fundamental and practical reasons for this. Until recently, the quantum field theory of the electromagnetic field has lacked a description of separate local conservation laws for

the spin and orbital angular momentum-generating currents [8]. Whether such spin-generating momenta, as opposed to the actual spin angular momenta they induce, are indeed observable or merely 'virtual' is of fundamental interest.

Moreover, if the electromagnetic spin and orbital momenta are separable, the question arises as to whether there are any photonic spin-orbit interaction effects. In other words, is it possible to convert electromagnetic spin into orbital angular momentum and vice-versa? Bliokh, Dressel and Nori give a positive answer for non-paraxial fields [114]. Using the conservation laws proposed by these authors, we show here that it is also possible to magnetically induce electromagnetic spinorbit coupling in magneto-optic media. Furthermore, we demonstrate, specifically, that Faraday rotation can be relied upon to convert the transverse spin of evanescent waves in guided light into orbital angular momentum of free-space beams, thus confirming the validity of the Bliokh-Dressel-Nori formulation, and providing a mechanism for free-space optical angular momentum generation and control. We show that the transfer of spin-generating momenta into orbital momenta plays a central role in electromagnetic spin-orbit coupling.

The electromagnetic field-expressions for transverse magnetization (y-direction) and monochromatic TM mode propagation in the z-direction in a slab waveguide are,

$$\vec{E} = (E_x, 0, E_y)\, e^{i(\beta z - \omega t)} \tag{4.5}$$

$$\vec{H} = (0, H_y, 0)\, e^{i(\beta z - \omega t)} \tag{4.6}$$

In magneto-optic media, the off-diagonal components ±g of the dielectric permittivity tensor $\hat{\epsilon}$ parameterize the magneto-optic gyrotropy. Maxwell-Ampere′s and Faraday′s laws in ferrimagnetic media are

$$\vec{\nabla} \times \vec{H} = \epsilon_0 \hat{\epsilon} \frac{\partial \vec{E}}{\partial t} = \epsilon_0 \begin{pmatrix} \epsilon_c & 0 & ig \\ 0 & \epsilon_c & 0 \\ -ig & 0 & \epsilon_c \end{pmatrix} \frac{\partial \vec{E}}{\partial t} = -\epsilon_0 \begin{pmatrix} \epsilon_c & 0 & ig \\ 0 & \epsilon_c & 0 \\ -ig & 0 & \epsilon_c \end{pmatrix} i\omega \vec{E} \tag{4.7}$$

$$\vec{\nabla} \times \vec{E} = -\mu_0 \frac{\partial \vec{H}}{\partial t} = \mu_0 i\omega \vec{H} \tag{4.8}$$

We examine transverse-magnetic (TM) propagation in the slab. Vertical and transverse directions are x, and y, respectively, β is the propagation constant, and the wave equation in the iron garnet is given by

$$\frac{\partial^2}{\partial x^2} H_y + \left[\kappa_0^2 \left(\epsilon_c - \frac{g^2}{\epsilon_c} - \beta^2 \right) \right] H_y = 0 \tag{4.9}$$

with $\kappa_0 = 2\pi/\lambda$ for wavelength λ We get:

$$H_y = H_c\, exp\left(-\gamma_{eff} x\right), \qquad \{\, x > 0 \qquad \text{Top cladding}\} \tag{4.10}$$

$$H_y = H_f\, \cos\left(\kappa_x x + \phi_c\right), \qquad \{\, -d < x < 0 \qquad \text{Core}\} \tag{4.11}$$

$$H_y = H_s\, exp\left[\gamma_s\left(x+d\right)\right], \qquad \{\, x < -d \qquad \text{Substrate}\} \tag{4.12}$$

Where

$$large\gamma_{eff} = \sqrt{\beta^2 - \kappa_0^2 \epsilon_{eff}} \tag{4.13}$$

$$\kappa_x = \sqrt{\kappa_0^2 \epsilon_f - \beta^2} \tag{4.14}$$

$$\gamma_x = \sqrt{\beta^2 - \kappa_0^2 \epsilon_s} \tag{4.15}$$

ϵ_f , and ϵ_s are the silicon-slab and substrate dielectric-permittivity constants, respectively, and d is the slab thickness. Defining

$$\epsilon_{eff} = \epsilon_c - \frac{\mathrm{g}^2}{\epsilon_c} \tag{4.16}$$

as an effective permittivity in the cover layer, and γ_{eff} as the corresponding decay constant in the x-direction, one can find,

$$E_z = i\frac{\mathrm{g}\beta - \epsilon_c \gamma_{eff}}{\omega\epsilon_0\left(\epsilon_c^2 - \mathrm{g}^2\right)} H_y \tag{4.17}$$

$$E_x = \frac{\beta\epsilon_c - \mathrm{g}\gamma_{eff}}{\omega\epsilon_0\left(\epsilon_c^2 - \mathrm{g}^2\right)} H_y \tag{4.18}$$

We treat the standard (electric-biased) formulation of the electromagnetic spin and orbital angular momenta. In the presence of dielectric media, such as iron garnets in the near-infrared range, the expression for 'Minkowski' spin angular momentum

becomes

$$\vec{s}_M = \mathrm{Im}\frac{\epsilon_0\epsilon}{2\omega}\left(\vec{E}^* \times \vec{E}\right) \tag{4.19}$$

The orbital momentum is

$$\vec{p}_O = \mathrm{Im}\frac{\epsilon}{2\omega}\left(\epsilon_0\vec{E}^* \cdot \nabla\vec{E}\right) \tag{4.20}$$

where $\vec{X}\cdot\nabla\vec{Y} = X_x\nabla Y_x + X_y\nabla Y_y + X_z\nabla Y_z$ and ϵ is the relative dielectric permittivity of the medium [114, 117]. This expression is derivable from Eq. (4.4). The transverse Minkowski spin angular momentum, spin momentum and the orbital momentum densities in evanescent nonreciprocal electromagnetic waves, derived from Eq. (4.17), (4.18), (4.19) and Eq. (4.20), are

$$\vec{s}_M = \frac{\epsilon}{\omega^3\epsilon_0}\left(\frac{\epsilon_c\gamma_{eff} - \beta\mathrm{g}}{\epsilon_c^2 - \mathrm{g}^2}\right)\left(\frac{\beta\epsilon_c - \mathrm{g}\gamma_{eff}}{\epsilon_c^2 - \mathrm{g}^2}\right)|H_y|^2\hat{y} \tag{4.21}$$

$$\vec{p}_M = -\frac{\epsilon\gamma_{eff}}{\omega^3\epsilon_0}\left(\frac{\epsilon_c\gamma_{eff} - \beta\mathrm{g}}{\epsilon_c^2 - \mathrm{g}^2}\right)\left(\frac{\beta\epsilon_c - \mathrm{g}\gamma_{eff}}{\epsilon_c^2 - \mathrm{g}^2}\right)|H_y|^2\hat{y} \tag{4.22}$$

$$\vec{p}_O = \frac{\beta\epsilon}{2\omega^3\epsilon_0}\left[\frac{\epsilon_c\gamma_{eff} - \beta\mathrm{g}}{\epsilon_c^2 - \mathrm{g}^2}\right]^2 + \left[\frac{\beta\epsilon_c - \mathrm{g}\gamma_{eff}}{\epsilon_c^2 - \mathrm{g}^2}\right]^2|H_y|^2\hat{y} \tag{4.23}$$

And the ratio

$$\left|\frac{\vec{p}_O}{\vec{s}_M}\right| = \frac{\beta}{2}\left(\frac{\epsilon_c\gamma_{eff} - \beta\mathrm{g}}{\beta\epsilon_c - \mathrm{g}\gamma_{eff}} + \frac{\beta\epsilon_c - \mathrm{g}\gamma_{eff}}{\epsilon_c\gamma_{eff} - \beta\mathrm{g}}\right) \tag{4.24}$$

Re-expressing the transverse Minkowski spin angular momentum and spin momentum

densities in terms of the energy flow $\vec{s}$ gives,

$$\vec{s}_M = \frac{2\epsilon}{\omega^2}\left(\frac{\epsilon_c\gamma_{eff} - \beta \mathrm{g}}{\epsilon_c^2 - \mathrm{g}^2}\right)\left|\vec{S}\right|\hat{y} \tag{4.25}$$

$$\vec{p}_M = -\frac{2\epsilon\gamma_{eff}}{\omega^2}\left(\frac{\epsilon_c\gamma_{eff} - \beta \mathrm{g}}{\epsilon_c^2 - \mathrm{g}^2}\right)\vec{S} \tag{4.26}$$

The time-averaged electromagnetic energy flux (Poyntings vector) in the iron garnet layer is

$$\vec{S} = \frac{1}{2}\mathrm{Re}\left(\vec{E}^* \times \vec{H}\right) = \frac{1}{2}\frac{\beta\epsilon_c - \mathrm{g}\gamma_{eff}}{\omega\epsilon_0\left(\epsilon_c^2 - \mathrm{g}^2\right)}\left|H_y\right|^2\hat{z} \tag{4.27}$$

The nonreciprocal shift normalized to the average spin angular momentum is expressed as follows,

$$\nabla\vec{s}_M = 2\frac{\epsilon_f\left(\epsilon_c\gamma_{eff} - \beta \mathrm{g}\right)_f - \epsilon_b\left(\epsilon_c\gamma_{eff} - \beta \mathrm{g}\right)_b}{\epsilon_f\left(\epsilon_c\gamma_{eff} - \beta \mathrm{g}\right)_f + \epsilon_b\left(\epsilon_c\gamma_{eff} - \beta \mathrm{g}\right)_b} \tag{4.28}$$

Subscripts f and b stand for forward, and backward propagation, respectively. Fig. 4.2 plots the Minkowski transverse spin-angular-momentum-density shift, as a function of silicon slab thickness. Specifically, it shows the normalized shift in the Eq. 4.16 pre-factor,

$$\nabla s_M = \frac{\left[\epsilon\left(\frac{\epsilon_c\gamma_{eff}-\beta \mathrm{g}}{\epsilon_c^2-\mathrm{g}^2}\right)\left(\frac{\beta\epsilon_c-\mathrm{g}\gamma_{eff}}{\epsilon_c^2-\mathrm{g}^2}\right)\right]_{\mathrm{g}} - \left[\left(\frac{\epsilon_c\gamma_{eff}-\beta \mathrm{g}}{\epsilon_c^2-\mathrm{g}^2}\right)\left(\frac{\beta\epsilon_c-\mathrm{g}\gamma_{eff}}{\epsilon_c^2-\mathrm{g}^2}\right)\right]_{-\mathrm{g}}}{\frac{1}{2}\left\{\left[\epsilon\left(\frac{\epsilon_c\gamma_{eff}-\beta \mathrm{g}}{\epsilon_c^2-\mathrm{g}^2}\right)\left(\frac{\beta\epsilon_c-\mathrm{g}\gamma_{eff}}{\epsilon_c^2-\mathrm{g}^2}\right)\right]_{\mathrm{g}} - \left[\left(\frac{\epsilon_c\gamma_{eff}-\beta \mathrm{g}}{\epsilon_c^2-\mathrm{g}^2}\right)\left(\frac{\beta\epsilon_c-\mathrm{g}\gamma_{eff}}{\epsilon_c^2-\mathrm{g}^2}\right)\right]_{-\mathrm{g}}\right\}} \tag{4.29}$$

We observe a moderate, and relatively stable, admixture of minority circularly-polarized component above 0.3 μm thickness. Finally, in order to estimate the

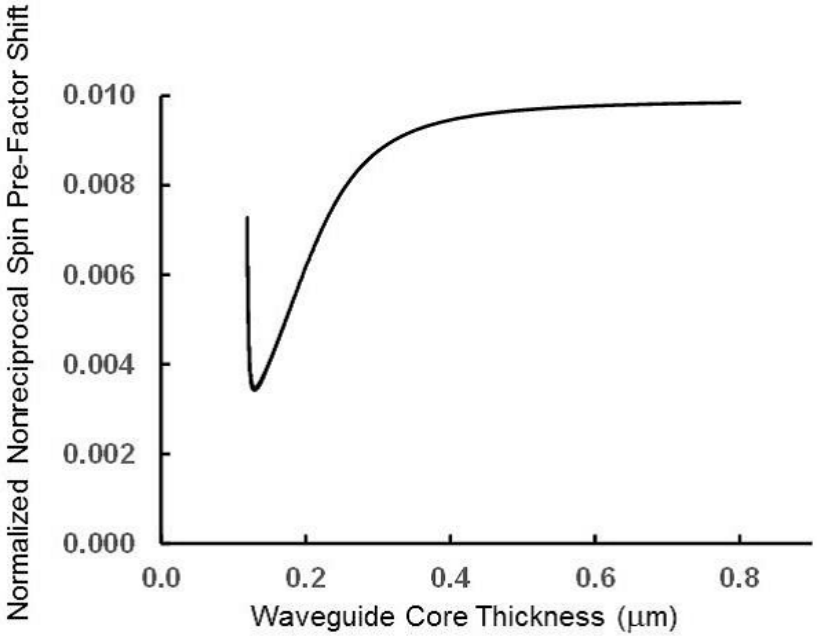

Figure 4.2: Normalized nonreciprocal Minkowski transverse spin-angular-momentum-density prefactor shift as a function of silicon slab thickness for $g = -0.0086$, corresponding to 450^0 degree/cm Faraday rotation of $Ce_1Y_2Fe_5O_{12}$ garnet [11] top cladding on SOI at $\lambda = 1.55\ \mu m$ wavelength.

coupling of circularly polarized light in an elliptical mode, we express the incoming circular polarization as the superposition of elliptical normal modes of opposite helicities, and take the fraction that couples into the same helicity elliptical mode to be the amplitude fraction of the circularly polarized incoming beam that gets coupled in, as follows:

$$E_+ \frac{1}{\sqrt{2}} (\hat{x} + i\hat{z}) = E_{+e} \frac{\hat{x} + ie\hat{z}}{\sqrt{1+e^2}} + E_{-e} \frac{e\hat{x} - i\hat{z}}{\sqrt{1+e^2}} \tag{4.30}$$

This Yields:

$$\left(\frac{E_+ e}{E_+}\right)^2 = \frac{1}{2}\left(\frac{e+1}{1+e^2}\right) \tag{4.31}$$

This expression represents the coupling power from circularly polarized input beam to the elliptical beam of similar helicity and depends on the eccenticity 'e' of the ellipse in the evanescent region.

4.3 Results

4.3.1 Magnetic-Gyrotropy-Dependent Evanescent Waves

The off-diagonal components ± g of the magnetic garnets dielectric permittivity tensor, $\hat{\varepsilon} = \begin{pmatrix} \epsilon_c & 0 & i\mathrm{g} \\ 0 & \epsilon_c & 0 \\ -i\mathrm{g} & 0 & \epsilon_c \end{pmatrix}$ control the magneto-optic response of the structure. The TM mode′s electric-field components in the top cladding are as given in equations 4.17 and 4.18;

$$E_z = i\frac{\mathrm{g}\beta - \epsilon_c \gamma_{eff}}{\omega\epsilon_0(\epsilon_c^2 - \mathrm{g}^2)} H_y \tag{4.32}$$

$$E_x = i\frac{\beta\epsilon_c - \mathrm{g}\gamma_{eff}}{\omega\epsilon_0(\epsilon_c^2 - \mathrm{g}^2)} H_y \tag{4.33}$$

where H_y is the optical magnetic-field, β is its propagation constant in the z-direction, $\gamma_{eff} = \sqrt{\beta^2 - \kappa_0^2\left(\epsilon_c - \frac{g^2}{\epsilon_c}\right)}$ is the decay constant in the (vertical) x-direction, $\kappa_0 = 2\pi/\lambda$, λ is the free-space wavelength, and ϵ_c is the cover-layer′s dielectric-permittivity constant. The other components, $E_y = H_x = H_z = 0$ Notice that these two electric field components are $\pi/2$ out of phase, hence the polarization is elliptical in the cover layer, with optical spin transverse to the propagation direction. In addition, the polarization evinces opposite helicities for counter-propagating beams, as E_z/E_x changes sign upon propagation direction reversal. This result already contains an important difference with reciprocal non-gyrotropic formulations, where $E_z/E_x = -i\gamma/\beta$, and γ the decay constant in the top cladding. Equations 4.32 and 4.33 depend on the gyrotropy parameter g, both explicitly and implicitly through β, and are therefore magnetically tunable, as we shall see below. We emphasize that the magnitude and sign of the propagation constant change upon propagation direction reversal, and separately, upon magnetization direction reversal. The difference between forward and backward propagation constants is also gyrotropy dependent. This nonreciprocal quality of magneto-optic waveguides is central to the proper functioning of certain on-chip devices, such as Mach-Zehnder-based optical isolators [23, 39]. In a dielectric medium, the momentum density expression accounts for the electronic response to the optical wave. Minkowski′s and Abraham′s formulations describe the canonical and the kinetic electromagnetic momenta, respectively [118]. Here we will focus on Minkowskis version, $\vec{p} = \vec{D} \times \vec{B}$, as it is intimately

linked to the generation of translations in the host medium, and hence to optical phase shifts, of interest in nonreciprocal phenomena. $\vec{D}$ is the displacement vector, and $\vec{B}$ the magnetic flux density. Dual-symmetric versions of electromagnetic field

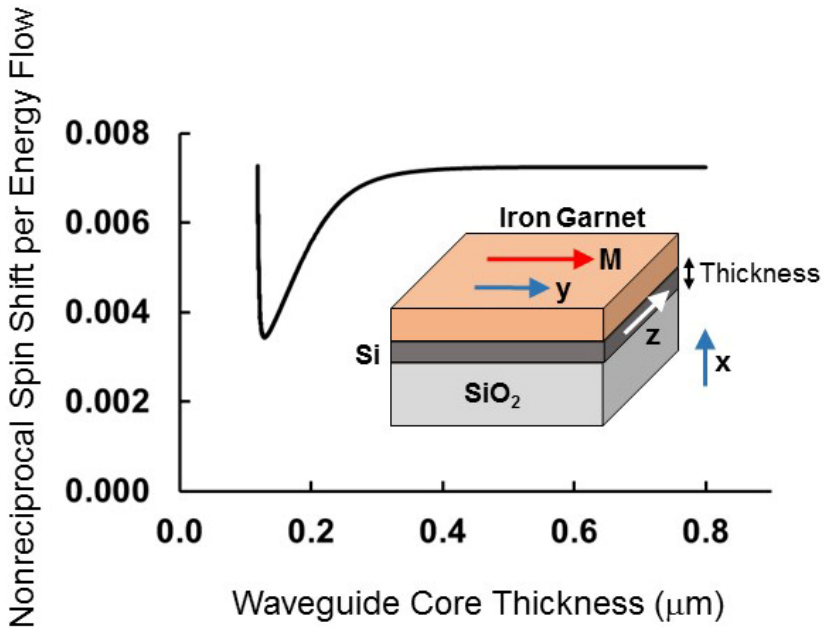

Figure 4.3: Normalized nonreciprocal Minkowski transverse spin-angular-momentum-density shift per unit energy flux as a function of silicon slab thickness for for g=0.0086, corresponding to $Ce_1Y_2Fe_5O_{12}$ garnet top cladding on SOI at wavelength. The inset shows the slab waveguide structure. M stands for the magnetization in the garnet.

theory in free space have been considered by various authors [108, 112, 114, 118]. However, the interaction of light and matter at the local level often has an electric character. Dielectric probe particles will generally sense the electric part of the electromagnetic momentum and spin densities [108, 112, 114, 118]. Hence, we treat the standard (electric-biased) formulation of the electromagnetic spin and orbital angular

momenta. In the presence of dielectric media, such as iron garnets in the near-infrared range, the expression for the Minkowski spin angular momentum becomes

$$\vec{s}_M = \mathrm{Im}\frac{\epsilon_0\epsilon}{2\omega}(\vec{E}^* \times \vec{E}) \tag{4.34}$$

The orbital momentum is

$$\vec{p} = \mathrm{Im}\frac{\epsilon}{2\omega}(\epsilon_0\vec{E}^* \cdot \nabla\vec{E}) \tag{4.35}$$

where ϵ is the relative dielectric permittivity of the medium [114, 117]. In magneto-optic media, the dielectric permittivity ϵ is $\epsilon_c \pm \mathrm{g}$, depending on the helicity of the propagating transverse circular polarization. This is usually a small correction to ϵ_c , as g is two-, or three-, orders of magnitude smaller in iron garnets, in the near infrared range. For elliptical spins, where one helicity component dominates, we account for the admixture level of the minority component in through a weighted average.

4.3.2 Nonreciprocal Transverse Magneto-Optic Spin-Orbit Coupling

In this section we present a formulation for the transverse-spin and orbital angular momentum densities, and nonreciprocal spin-orbit coupling induced by evanescent fields in magneto-optic media. The magnitude and tuning range of these objects in terms of waveguide geometry and optical gyrotropy are expounded and discussed.

We detail the differences in orbital angular momenta between transversely propagating beams induced by circularly-polarized light of opposite helicities. Their unequal response to given optical energy fluxes in opposite propagation directions and to changes in applied magnetic fields are analyzed. And we apply the recently proposed Bliokh-Dressel-Nori electromagnetic spin-orbit correction term to calculate the spin-orbit interaction for evanescent waves in gyrotropic media [114]. Eqs. (4.32) to ((4.35)) yield the following expressions for the transverse Minkowski spin angular momentum, spin momentum and the orbital momentum densities in evanescent nonreciprocal electromagnetic waves:

$$\vec{s}_M = \frac{\epsilon}{\omega^3 \epsilon_0} \left(\frac{\epsilon_c \gamma_{eff} - \beta \mathrm{g}}{\epsilon_c^2 - \mathrm{g}^2} \right) \left(\frac{\beta \epsilon_c - \mathrm{g} \gamma_{eff}}{\epsilon_c^2 - \mathrm{g}^2} \right) |H_y^2| \hat{y} \tag{4.36}$$

$$\vec{p}_O = \frac{\beta \epsilon}{2\omega^3 \epsilon_0} \left[\left(\frac{\epsilon_c \gamma_{eff} - \beta \mathrm{g}}{\epsilon_c^2 - \mathrm{g}^2} \right)^2 + \left(\frac{\beta \epsilon_c - \mathrm{g} \gamma_{eff}}{\epsilon_c^2 - \mathrm{g}^2} \right)^2 \right] |H_y^2| \hat{z} \tag{4.37}$$

These expressions depend on the magneto-optic gyrotropy parameter g and the dielectric permittivity of the waveguide core channel and of its cover layer under transverse magnetization. They yield different values under magnetic field tuning, magnetization and beam propagation direction reversals, and as a function of waveguide core

thickness as discussed below. The propagation constant β is gyrotropy-, propagation-direction-, and waveguide-core-thickness-dependent and this behavior strongly impacts the electromagnetic spin and orbital momenta. Consider now the electromagnetic spin-orbit coupling induced by transversely propagating circularly polarized beams impinging on a gold nanoparticle on the surface of a silicon-on-insulator slab waveguide with Ce-YIG cover layer, as in Fig. 4.1(a). Alternatively, one may examine the response of a magnetic garnet waveguide on gadolinium-gallium garnet substrate and air cover as in Fig. 4.3(b). These configurations are similar to the chiral nanophotonic waveguide arrangement considered in [115], except that we are now dealing with a magneto-optic nonreciprocal system. We assume (but do not prove), that the light emitted by the rotating dipole in the gold nanoparticle couples to the elliptically polarized evanescent tail of the same helicity as the rotating dipole, as was shown in [115] and [110]. The sign of the helicity of the evanescent TM wave locks-in the direction of propagation, resulting in unidirectional spin-orbit coupling. We now explore the difference in unidirectionally-excited orbital momenta and coupling efficiency for opposite helicities in the magneto-optic system, based on Eqs. 4.36 and 4.37. Figure 4.5(a) plots the shift in coupled orbital momentum per unit spin angular momentum, in a slab waveguide for opposite excitation helicities. This quantity is obtained from the difference in ratio of Eqs.4.37 to 4.36, for opposite propagation directions. The result is plotted as a function of magneto-optic gyrotropy. Plotted in the same figure 4.5(b), we also have the coupling efficiency shift for unidirectional propagation

for opposite-helicity circularly polarized excitations. The latter is obtained from the overlap of the circular polarization input to the evanescent tail elliptical polarization, obtained from Eqs. 4.32 and 4.33. Notice that the nonreciprocal orbital momentum shift of the excited unidirectionally-oriented light is significant (0.1%) for typical magneto-optical gyrotropies (0.001 to 0.01) found in the infrared regime in magnetic garnet materials. Even larger shifts (up to 1%) obtain in the visible range. Larger shifts are possible for ferromagnetic metallic materials (plasmonic guiding) possessing significantly larger gyrotropies. These latter effects have yet to be explored both theoretically and experimentally. Consider now the excited nonreciprocal spin angular

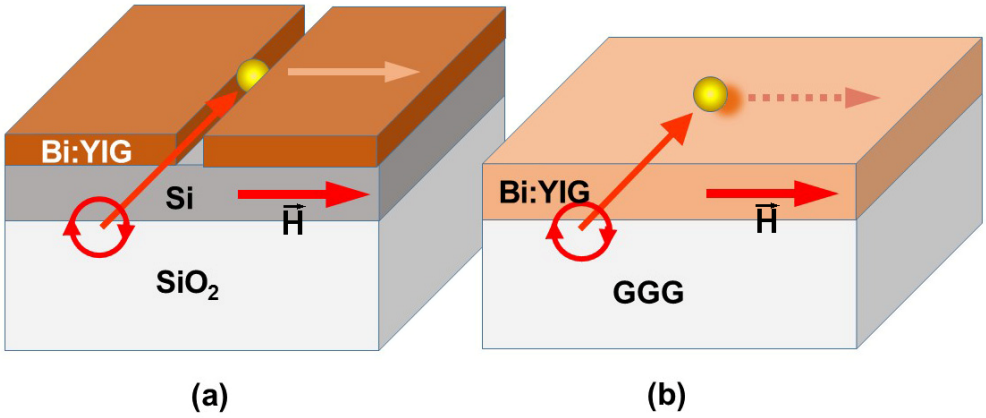

Figure 4.4: Schematic depiction of electromagnetic spin-orbit coupling configuration consisting of a transversely-propagating circularly polarized beam impinging on a gold nanoparticle on (a) the surface of a silicon-on-insulator slab waveguide with bismuth-substituted yttrium iron garnet (Bi:YIG) cover layer, or (b) a Bi:YIG slab waveguide, to produce unidirectional propagation of waveguide modes normal to the incoming beam.

momentum shifts per energy flow ,

$$\vec{s}_M = \frac{2\epsilon}{\omega^2}\left(\frac{\epsilon_c\gamma_{eff} - \beta \mathrm{g}}{\epsilon_c^2 - \mathrm{g}^2}\right)|\vec{S}|\hat{y} \tag{4.38}$$

Figure 4.3 plots the nonreciprocal transverse spin-angular-momentum-density shift per unit energy flux, as a function of silicon slab thickness in an SOI slab waveguide with $Ce_1Y_2Fe_5O_{12}$ garnet top cladding. Calculations are performed for the same electromagnetic energy flux in opposite propagation directions, at a wavelength of 1550 nm, g = -0.0086 . The nonreciprocal shift is normalized to the average spin

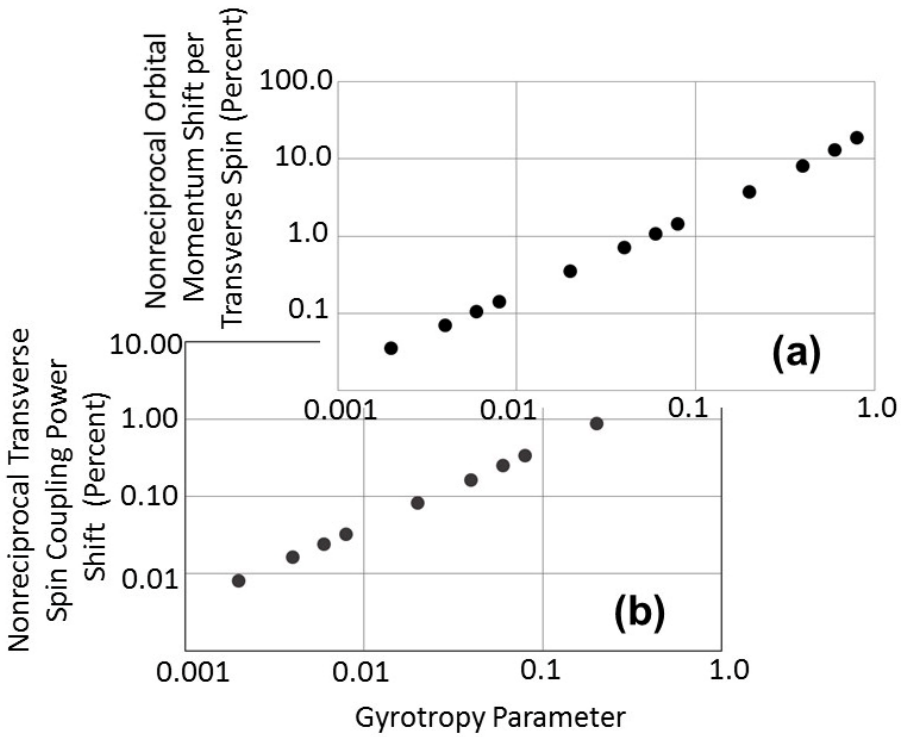

Figure 4.5: Difference in (a) unidirectionally-excited orbital momenta and (b) coupling efficiencies for opposite helicities in the magneto-optic system. (a) plots the shift in coupled orbital momentum per unit spin angular momentum, in a slab waveguide for opposite excitation helicities.

angular momentum. The energy shift evinces a relatively stable value, close to 0.7 % above $0.3\,\mu m$ thickness. Its thickness dependence is a function of the ellipticity of the transverse polarization in the x-z plane. Above $0.3\,\mu m$, the ellipticity ranges from 31.4^0 to 36.9^0, where 45^0 corresponds to circular polarization. In other words, the ellipticity stays fairly constants, with a moderately small admixture of the minority circularly polarized component, ranging from 25 % to 14 %. Below $0.3\,\mu m$, the minority component admixture increases precipitously, reaching 87 % at $0.13\,\mu m$. Magnetization reversals produce the same effect, for the corresponding transverse spin-angular-momentum-density shift.

4.3.3 Magneto Optic Gyrotropy Control of Spin Orbit Effects

The magneto-optic gyrotropy of an iron garnet can be controlled through an applied magnetic field. These ferrimagnetic materials evince a hysteretic response, such as the one displayed in Fig. 4.6 (inset) for 532 nm wavelength in a sputter-deposited film. The target composition is $Bi_{1.5}Y_{1.5}Fe_5O_{12}$. Shown here are actual experimental data extracted from Faraday rotation measurements. Below saturation, the magneto-optic response exhibits an effective gyrotropy value that can be tuned through the application of a magnetic field. These measurements correspond to a $0.5\,\mu m$ -thick film on a

(100)-oriented gadolinium gallium garnet (GGG) substrate. The optical beam is incident normal to the surface, and the hysteresis loop probes the degree of magnetization normal to the surface as a function of applied magnetic field. These data show that the electromagnetic spin angular momentum can be tuned below saturation and between opposite magnetization directions. Figure 4.6 also reveals an interesting feature about the magneto-optic gyrotropy. The normalized nonreciprocal transverse spin-

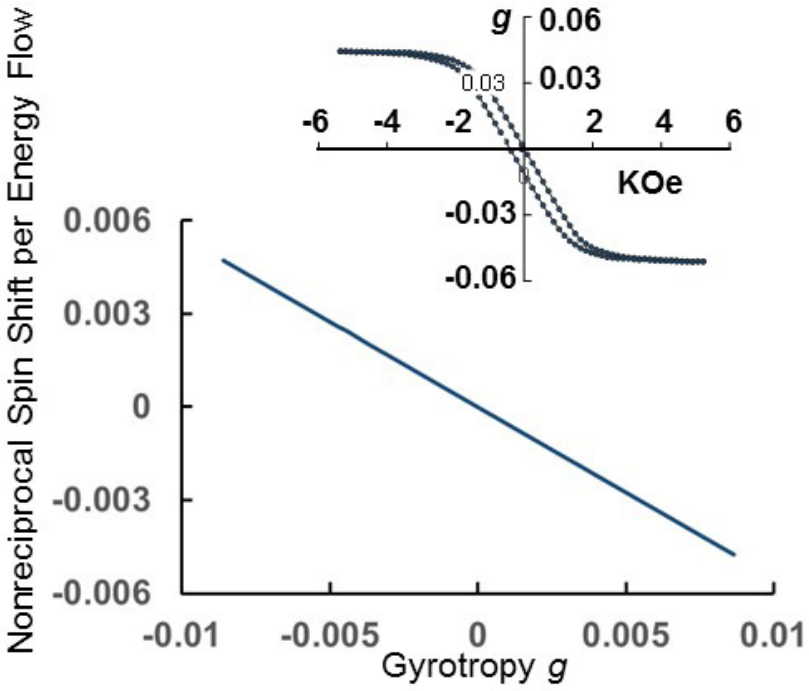

Figure 4.6: Normalized nonreciprocal Minkowski transverse spin-angular-momentum-density shift per unit energy flux as a function of magneto-optical gyrotropy. Data correspond to 0.25 m silicon-slab thickness with $Ce_1Y_2Fe_5O12$ garnet top cladding, wavelength. The inset shows the gyrotropy versus magnetic field hysteresis loop of a magnetic garnet film at $\lambda = 532nm$, sputter-deposited using a $Bi_{1.5}Y_{1.5}Fe_5O_{12}$target.

angular-momentum-density shift per unit energy flux linearly tracks the gyrotropy,

and is of the same order of magnitude as g, although thickness-dependent. Yet, as pointed out before, this thickness dependence reflects the admixture of the minor helicity component in the spin ellipticity. At 0.4 μm, for example, $\nabla \vec{s}_M = 0.0072$ when g = -0.0086. However, the major polarization helicity component contribution to $\nabla \vec{s}_M$ is 84.4% at this thickness, translating into 0.00853 at 100 %. At 0.25 μm, $\nabla \vec{s}_M = 0.00655$ and the major polarization helicity component contribution is 76.2 %, translating into 0.0086 at 100%. We thus re-interpret the magneto-optical gyrotropy as the normalized spin-angular-momentum density shift per unit energy flux. Fig. 4.1 illustrates schematically the induction of free-space vortex beams. The difference in free-space vortex beams orbital angular momenta are therefore apparent from Fig. 4.5, a consequence of the difference induced by coupling light with positive or negative spin helicities into the waveguide. The fact that the magneto-optic gyrotropy can be tuned, as discussed above, means that the magnitude orbital momenta and the phase of the coupled light (and hence the resonance of the coupled light in the resonator), can be tuned to resonate for either positive or negative helicity excitation beams, while at the same time suppressing the excitation of one or the other free-space helicoidal beams. These are novel proposed effects that translate into magnetic control of free-space helicoidal beams for opposite chiralities.

4.3.4 Magnetization-Induced Electromagnetic Spin-Orbit Coupling

Bliokh and co-authors have studied the electromagnetic spin-orbit coupling in non-paraxial optical beams [114]. They find that there is a spin-dependent term in the orbital angular momentum expression that leads to spin-to-orbit angular momentum conversion. This phenomenon occurs under tight focusing or the scattering of light [114]. Here we consider an alternative source of electromagnetic spin-orbit coupling, magnetization-induced coupling in evanescent waves. The time-averaged spin- $\mathrm{Im}\frac{\epsilon\epsilon_0}{2\omega}\left(\vec{E}^* \times \vec{E}\right)_i$, and orbital- $\mathrm{Im}\frac{\epsilon\epsilon_0}{2\omega}\left(\vec{E}^* \cdot (\vec{r} \times \nabla)\,\vec{E}\right)_i$ angular momenta conservation laws put forth in [114] each contain a term, responsible for spin-orbit coupling, in the form

$$\mathrm{Im}\frac{\epsilon\epsilon_0\mu_0}{2\omega}H_j^* E_i. \tag{4.39}$$

We have modified the original expressions to include a dielectric permittivity factor to account for the material response of the medium. The indices i = x, y, z. Expression 4.39 appears with opposite signs in the spin and orbital conservation laws, signaling a transfer of angular momentum from spin to orbital motion. As it stands so far in our treatment, this term equals zero, since the spin points in the y-direction and the electric-field components of the TM wave point in the x- and z-directions. A way to overcome this null coupling and enable the angular momentum transfer is to rotate

the applied magnetic field about the x-axis away from the y-direction, as in Fig. 4.7. This action induces a Faraday rotation about the z-axis, generating a spin-orbit coupling term in the angular momentum conservation laws. An in-plane rotation of the magnetization M to the z-axis will induce TM to TE mode conversion and electromagnetic spin-orbit interaction in the magneto-optic medium [119, 120]. Hence, non-zero electromagnetic field components E_y and H_x, and spin-orbit coupling, are induced in the propagating wave. The spatial non-intrinsic component characteristic of orbital motion emerges in the form of a z-dependence in the angular momentum, embodied in the partial or total evanescence of the major circularly-polarized transverse-spin component as the wave propagates along the guide. In what sense is there an angular momentum transfer from spin to orbital, in this case? As the polarization rotates in the x-y plane due to the Faraday effect, there will be a spatially-dependent reduction in the circulating electric field spin-component of the electromagnetic wave along the propagation-direction. This can be seen as a negative increase in circular polarization with z, i.e., an orbital angular momentum in the opposite direction to the electromagnetic spin. More specifically, the TE mode, with an electric-field component only in the y-direction, carries no transverse spin angular momentum, as per Eq. 4.34. Where does this angular momentum go? It goes into orbital angular momentum, according to Eq. 4.39. This electromagnetic orbital angular momentum (OAM) in the TE mode may be converted into free-space OAM via a helicoidal beam emitter as proposed in [111]. These authors demonstrate an integrated compact vortex beam

emitter through the use of a circular micro-ring or micro-disk optical resonator, as in Fig. 4.1, furnished with an embedded angular grating. The grating partially converts the whispering gallery mode in the micro-ring into free-space radiation. The device is configured to emit vortex beams from quasi-TE light fed into the micro-ring via a straight waveguide bus coupled it. At issue here is not the Faraday rotation per se, but the conversion of transverse spin angular momentum into orbital angular momentum. Finally, we derive an explicit expression for the spin-orbit coupling term.

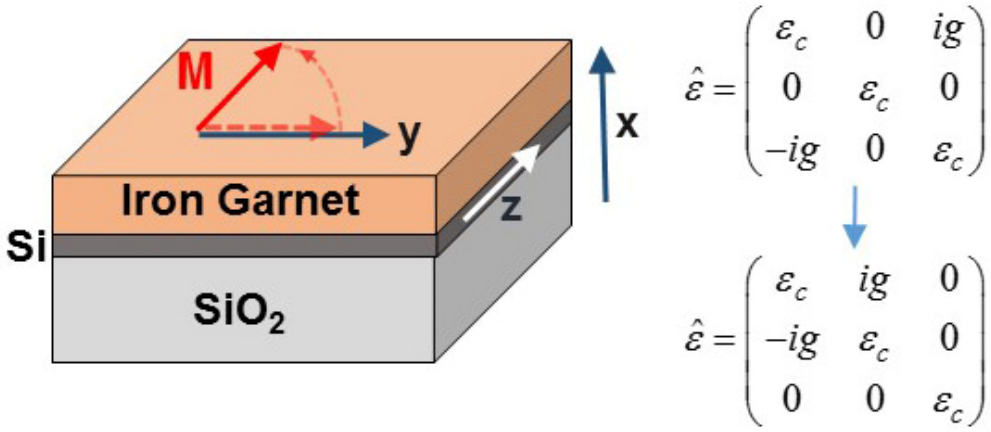

Figure 4.7: Rotated magnetization M generates TM to TE waveguide mode coupling and electromagnetic spin-orbit coupling. The figure also shows the electric permittivity tensor before and after rotation.

We assume that Faraday rotation induces the E_y, H_z terms via TM to TE mode conversion, where $H_z = \dfrac{-i}{\mu_0 \omega} \dfrac{\partial}{\partial x} E_y$, and $E_y = E_{y,0}\, e^{-\gamma_{TE} x} e^{i\beta_{TE} z} \sin(\theta_F z)$. Where $E_{y,0}$ is the electric field amplitude corresponding to full TM to TE conversion, θ_F is the specific Faraday rotation angle, γ_{TE} and β_{TE} are the cover-layer decay constant

and the propagation constant for the TE mode, respectively. For simplicity, we assume no linear birefringence in the waveguide, so $\beta_{TE} = \beta_{TM}$. The spin to orbital angular-momentum coupling term is then

$$\mathrm{Im}\frac{\epsilon\epsilon_0\mu_0}{2\omega}\partial_z\left(H_z^* E_y\right) = \frac{\epsilon\epsilon_0\gamma_{TE}}{2\omega^2}|E_{y.0}^2|\, e^{-2\gamma_{TE}x}\theta_F \sin\left(2\theta_F z\right) \tag{4.40}$$

Hence full angular momentum conversion from transversely-coupled forward (or backward) propagating positive (negative) helicity light in the z-direction upon $\pi/2$ Faraday rotation generates a spin-to orbital momentum transfer $\frac{\epsilon_c\,\epsilon_0}{4\,\omega^2}|E_{y,0}|^2$ in the cover layer.

4.4 Discussion

There are two key findings in this work. A formulation of the interaction between nonreciprocal transverse electromagnetic spin and orbital angular momenta in evanescent waves in magneto-optic media. And a treatment of magnetically induced spin-orbit coupling in electromagnetic waves. Our analysis examines the effect of magneto-optic nonreciprocity on the orbital angular momenta of unidirectional light in nanophotonic waveguide interfaces generated by electromagnetic spin-orbit interaction. We explore

the role of optical chirality on the induced orbital momenta on transversely propagating light and quantify its response to opposite-spin optical excitations. The dependence of induced orbital momenta on magneto-optical gyrotropy is detailed. Additionally, the results presented here provide a means for testing the Bliokh-Dressel-Nori electromagnetic spin-orbit coupling formulation in magneto-optic media [114], and simultaneously, offer a way for magnetically inducing and controlling the electromagnetic spin-orbit interaction. The approach may be used to generate OAM helicoidal beams through spin to orbital angular momentum conversion, and to magnetically tune the production of free space orbital angular momenta via ring resonators. The latter relies on experimental results already demonstrated by X. Cai and co-workers in [111]. Our treatment of the nonreciprocal transverse electromagnetic spin is developed for slab waveguides with magnetic garnet cladding layers. This approach allows for an explicit analytical solution of the spin and orbital momenta and angular momenta that can be experimentally tested via prism-coupling in slab waveguides. As such, it allows for testing the controversial reality of electromagnetic spin momenta, in other words, the reality of the electromagnetic linear momenta that induce transverse spin-angular momenta. The article shows that transverse spin angular momentum in evanescent waves can be magnetically tuned, with possible applicability to nanoparticle optical manipulation, and that it evinces a precisely quantifiable nonreciprocal response in magneto-optic media. Moreover, we demonstrate that the shift in spin angular momentum per unit energy flow upon time or magnetization reversal

corresponds to the magneto-optical gyrotropy. This finding provides a dynamic interpretation of the magneto-optic gyrotropy parameter, and gives a fresh perspective on the source of the nonreciprocal phase shift effect, often used in the design of integrated optical isolators. The thickness dependence of the nonreciprocal transverse-spin-shift upon time or magnetization reversals is found to reflect the admixture of minority circular polarization component in the elliptical spin configuration in evanescent waves. This admixture is very pronounced for thin slabs near cutoff, but wanes and saturates for thicker samples, where the majority circular polarization dominates. Our treatment of electromagnetic spin-orbit coupling also provides a means for magnetically inducing and modulating OAM and free-space helicoidal beams. These can be produced on-chip in magneto-optic waveguides with magneto-optic claddings, thus allowing for compact packaging of vortex-bean sources. Nonreciprocal TE to TM mode conversion in semiconductor waveguides with magneto-optic upper claddings has already been demonstrated [119, 120]. Numerous applications of optical angular momentum and vortex beams have been discussed in the literature. These include their use in optical tweezers [121, 122], optical microscopy [123], and quantum and wireless communications [124, 125].

Chapter 5

Conclusion

5.1 Conclusions

In summary, this dissertation combines work done in three major projects on magneto-optic materials and exploiting their fundamental property that breaks time-reversal symmetry, also known as non-reciprocal effect. In the second chapter, we have carried out experiments on fabrication and characterization of magnetless magneto-optic materials to develop technology towards their integration into silicon photonics as on-chip optical isolators. In particular, the magnetless faraday rotator materials were thinned down by lapping/polishing and crystal-ion-slicing techniques to thicknesses down to 7 μm and their performance was studied against the inevitable birefrigence

effect on thin-film-waveguide-based devices. we have found that the Faraday rotation remains within 2^0 of bulk performance of 45^0 rotation. The extinction ratios of -20 dB was measured with insertion loss as low as 0.09 dB in 11 μm thin films fabricated by lapping. The linear birefringence affects the higher order modes in planar waveguide structure and the extinction ration could be improved by making the guide to support only the fundamental modes. Moreover, the magnetless FR was bonded with UV epoxy and BCB bonding materials and the performance of a complete isolator was also investigated. Greater than 30 dB isolation was measured for the wavelength band between 1522.5 nm to 1564 nm, with 33.7 dB at 1550 nm wavelength and insertion loss < 0.7 dB in the entire C-band of optical telecommunication. With the BCB bonded PolarCors polarizers, $60\mu m$ thin film isolator produced > 25 dB of isolation and $<$ 1dB insertion loss towards the upper end of C-band (1550 to 1580 nm).

In the second project described in chapter 3, experimental demonstration of topological edge state was carried out in SSH model based arrys of 7 waveguides fabricated by e-beam lithography. A high degree of localization of edge modes were observed for both TE and TM modes of of input excitation in waveguides with as little as only 2 % of power spreading towards the remaining waveguides in the array. Different aspects of challenges towards fabricating on-chip isolators was also analyzed . Shorter on-chip isolator devices can be realized based on this model by working in assymetric waveguide structures of high non-reciprocal effect.

Next work in chapter 4 encompasses the theretical study of spin orbit coupling of light in magnet-optic media in planer waveguide structures. It has been found that transverse spin angular momentum in evanescent waves can be magnetically tuned, with possible applicability to nanoparticle optical manipulation, and that it evinces a precisely quantifiable nonreciprocal response in magneto-optic media. Moreover, we demonstrate that the shift in spin angular momentum per unit energy flow upon time or magnetization reversal corresponds to the magneto-optical gyrotropy. This finding provides a dynamic interpretation of the magneto-optic gyrotropy parameter, and gives a fresh perspective on the source of the nonreciprocal phase-shift effect, often used in the design of integrated optical isolators. The thickness dependence of the nonreciprocal transverse-spin-shift upon time or magnetization reversals is found to reflect the admixture of a minority circular polarization component in the elliptical spin configuration in evanescent waves. This admixture is very pronounced for thin slabs near cutoff, but wanes and saturates for thicker samples, where the majority circular polarization dominates.

5.2 Future work

The research work in this dissertation successfully develops the magnetless optical isolator, its miniaturization, and successful transfer to the silicon substrates. The performance of the device is highly promising as it fulfills both requirements for an

optical isolator, i.e. high optical isolation and low loss to be used in an integrated circuit. However integration to the Si waveguide is the ultimate goal to establish its functionality and reliability to be used in an integrated optical circuit. This is something that has not been demonstrated and needs further experimental research work on this aspect.

This dissertation has also successfully demonstrated the topological edge-mode-based localization of the power in the edge waveguide and analyzed different aspects of the challenges and paves the way for further experimental exploration on realizing full functional on-chi optical isolator. Selecting the materials that offers high NRPS and relatively low propagation loss can be experimented to produce ultra-compact integrated isolators.

References

[1] Liu, J.; Sun, X.; Camacho-Aguilera, R.; Kimerling, L. C.; Michel, J. *Optics Letters* **2010**, (35), 679–681.

[2] Rong Sun, Jing Cheng, J. M.; Kimerling, L. *Optics Letters* **2009**, (34), 2378–2380.

[3] Levy, J. S.; Gondarenko, A.; Foster, M. A.; Turner-Foster, A. C.; Gaeta, A. L.; Lipson, M. *Nature Photonics* **2010**, (4), 37–40.

[4] Xu, Q.; Schmidt, B.; Pradhan, S.; Lipson, M. *Nature* **2005**, (435), 325–327.

[5] Yeatman, E. M.; Ahmad, M. M.; McCarthy, O.; Vannucci, A.; Gastaldo, P.; Barbier, D.; Mongardien, D.; Moronvalle, C. *Optics Communications* **1999**, *164*(1-3), 19–25.

[6] Klein, E. J.; Geuzebroek, D. H.; Kelderman, H.; Sengo, G.; Baker, N.; Driessen, A. *IEEE Photonics Technology Letters* **2005**, *17*, 2358–2360.

[7] Little, B. E.; Foresi, J. S.; Steinmeyer, G.; Thoen, E. R.; Chu, S. T.; Haus, H. A.; Ippen, E. P.; Kimerling, L. C.; Greene, W. *IEEE Photonics Technology Letters* **1998**, *10*(4), 549–551.

[8] Gomi, M.; Furuyama, H.; Abe, M. *Journal of Applied Physics* **1991**, *70*(11), 7065–7067.

[9] Onbasli, M. C.; Beran, L.; Zahradnk, M.; Kuera, M.; Anto, R.; Mistrk, J.; Dionne, G. F.; Veis, M.; Ross, C. A. *Scientific Reports* **2016**, *6*, 23640.

[10] Goto, T.; Onbasli, M. C.; Ross, C. A. *Opt.ics Express* **2012**, *20*(27), 28507–28517.

[11] Shintaku, T. *Applied Physics Letters* **1995**, *66*(21), 2789–2791.

[12] Block, A. D.; Dulal, P.; Stadler, B. J. H.; Seaton, N. C. A. *IEEE Photonics Journal* **2014**, *6*(1).

[13] Shintaku, T.; Uno, T.; Kobayashi, M. *Journal of Applied Physics* **1993**, *74*(8), 4877–4881.

[14] Huang, M.; Zhang, S.-Y. *Applied Physics A* **2002**, *74*(2), 177–180.

[15] Lage, E.; Beran, L.; Quindeau, A. U.; Ohnoutek, L.; Kucera, M.; Antos, R.; Sani, S. R.; Dionne, G. F.; Veis, M.; Ross, C. A. *APL Materials* **2017**, *5*(3), 036104.

[16] Erol, M.; Ozturk, Y.; Avgin, I.; Celik, E. *Journal of Physics: Conference Series* **2009**, *153*(1), 012049.

[17] Sun, X. Y.; Du, Q.; Goto, T.; Onbasli, M. C.; Kim, D. H.; Aimon, N. M.; Hu, J.; Ross, C. A. *ACS Photonics* **2015**, *2*(7), 856–863.

[18] Brandle, C. D.; JVincent, J.; Fratello, J.; Steven, J. L. *U.S. Patent No. 5,608,570.* **1997**.

[19] Abbott, R. R.; Fratello, V. J.; Licht, S. J.; Mnushkina, I. *U.S. Patent No. 5,608,570.* **1997**.

[20] Wolfe, R.; Fratello, V. J.; McGlashanPowell, M. *Journal of Applied Physics* **1988**, *63*(8), 3099–3103.

[21] Wolfe, R.; Lieberman, R. A.; Fratello, V. J.; Scotti, R. E.; Kopylov, N. *Applied Physics Letters* **1990**, *56*(5), 426–428.

[22] Levy, M.; Osgood, R. M.; Hegde, H.; Cadieu, F. J.; Wolfe, R.; Fratello, V. J. *IEEE Photonics Technology Letters* **1996**, *8*(7), 903–905.

[23] Fujita, J.; Levy, M.; Osgood Jr, R. M.; Wilkens, L.; Dtsch, H. *Applied Physics Letters* **2000**, *76*, 2158.

[24] Shoji, Y.; Mizumoto, T.; Yokoi, H.; Hsieh, I.-W.; Osgood, R. M. *Applied Physics Letters* **2008**, *92*(7), 071117.

[25] Ghosh, S.; Keyvavinia, S.; Van Roy, W.; Mizumoto, T.; Roelkens, G.; Baets, R. *Optics Express* **2012**, *20*(2), 1839–1848.

[26] Tien, M.-C.; Mizumoto, T.; Pintus, P.; Kromer, H.; Bowers, J. E. *Optics Express* **2011**, *19*(12), 11740–11745.

[27] Bi, L.; Hu, J.; Jiang, P.; Kim, D. H.; Dionne, G. F.; Kimerling, L. C.; Ross, C. A. *Nature Photonics* **2011**, *5*, 758.

[28] Dammann, H.; Pross, E.; Rabe, G.; Tolksdorf, W. *Applied Physics Letters* **1990**, *56*(14), 1302–1304.

[29] Hammer, J. M.; Abeles, J. H.; Channin, D. J. *IEEE Photonics Technology Letters* **1997**, *9*(5), 631–633.

[30] Shintaku, T. *Applied Physics Letters* **1998**, *73*(14), 1946–1948.

[31] Levy, M.; Ilic, I.; Scarmozzino, R.; Osgood, R. M.; Wolfe, R.; Gutierrez, C. J.; Prinz, G. A. *IEEE Photonics Technology Letters* **1993**, *5*(2), 198–200.

[32] Lira, H.; Yu, Z.; Fan, S.; Lipson, M. *Physical Review Letters* **2012**, *109*(3), 033901.

[33] Wolfe, R.; Hegarty, J.; Dillon, J. F.; Luther, L. C.; Celler, G. K.; Trimble, L. E.; Dorsey, C. S. *Applied Physics Letters* **1985**, *46*(9), 817–819.

[34] Wolfe, R.; Fratello, V. J.; McGlashanPowell, M. *Applied Physics Letters* **1987**, *51*(16), 1221–1223.

[35] Wolfe, R.; LeCraw, R. C.; Blank, S. L.; Pierce, R. D. *AIP Conference Proceedings* **1976**, *34*(1), 172–174.

[36] Okamura, Y.; Inuzuka, H.; Kikuchi, T.; Yamamoto, S. *Journal of Lightwave Technology* **1986**, *4*(7), 711–714.

[37] Kumar, P.; Levy, M. *Optics Letters* **2012**, *37*, 3762–3764.

[38] El-Ganainy, R.; Levy, M. *Optics Letters* **2015**, *40*(22), 5275–5278.

[39] Stadler, B. J. H.; Mizumoto, T. *IEEE photonics Journal 6*(1), 1–15.

[40] Levy, M. *IEEE Journal of Selected Topics in Quantum Electronics* **2002**, *8*(6), 1300–1306.

[41] Amnon Yariv, P. Y. *Optical Waves in Crystals: Propagation and Control of Laser Radiation;* John Wiley & sons, 1984.

[42] Saleh, B. E. A. *Fundamental of photonics;* John Wiley & sons, 2007.

[43] Inoue, M.; Levy, M.; Baryshev, A. V. *Magnetophotonics: From Theory to Applications;* Springer, 2013.

[44] Yang, H. *RF-Sputter Fabrication of Magnetic Garnet Thin Filmsand Simulation Modeling For1-D Magnetic Photonic Crystal Waveguide Devices* PhD thesis, **2005**.

[45] Mino, S.; Matsuoka, M.; Tate, A.; Shibukawa, A.; Ono, K. *Japanese Journal of Applied Physics* **1992**, *31*(6R), 1786.

[46] Pulliam, G. R.; Ross, W. E.; MacNeal, B.; Bailey, R. F. *Journal of Applied Physics* **1982**, *53*(3), 2754–2758.

[47] Uchishiba, H.; Tominaga, H.; Obokata, T.; Namikata, T. *IEEE Transactions on Magnetics* **1974**, *10*(3), 480–483.

[48] Wittekoek, S.; Poprna, T. J. A.; Robertson, J. M.; Bongers, P. F. *Physical review B* **1975**, *12*(7).

[49] Dionne, G. F. *Magnetic Oxides;* Springer Science & Business Media, 2010.

[50] Shintaku, T.; Uno, T. *Journal of Applied Physics* **1994**, *76*(12), 8155–8159.

[51] Shintaku, T. *Applied Physics Letters* **1998**, *73*(14), 1946–1948.

[52] Shoji, Y.; Mizumoto, T. *Science and Technology of Advanced Materials* **2014**, *15*(1), 014602.

[53] Ghosh, S.; Keyvaninia, S.; Shirato, Y.; Mizumoto, T.; Roelkens, G.; Baets, R. *IEEE Photonics Journal* **2013**, *5*(3), 6601108–6601108.

[54] Zhang, C.; Dulal, P.; Stadler, B. J. H.; Hutchings, D. C. *Scientific Reports* **2017**, *7*(1), 5820.

[55] Huang, D.; Pintus, P.; Shoji, Y.; Morton, P.; Mizumoto, T.; Bowers, J. E. *Optics Letters* **2017**, *42*(23), 4901–4904.

[56] Huang, D.; Pintus, P.; Zhang, C.; Shoji, Y.; Mizumoto, T.; Bowers, J. E. *IEEE Journal of Selected Topics in Quantum Electronics* **2016**, *22*(6), 271–278.

[57] Du, Q.; Wang, C.; Zhang, Y.; Zhang, Y.; Fakhrul, T.; Zhang, W.; Goncalves, C.; Blanco, C.; Richardson, K.; Deng, L.; Ross, C. A.; Bi, L.; Hu, J. *ACS Photonics* **2018**, *0*(ja), null.

[58] Karki, D.; Stenger, V.; Pollick, A.; Levy, M. *Journal of Applied Physics* **2017**, *121*(23), 233101.

[59] Shoji, Y.; Miura, K.; Mizumoto, T. *Journal of Optics* **2016**, *18*(1), 013001.

[60] Levy, M.; Osgood, R. M.; Kumar, A.; Bakhru, H. *Applied Physics Letters* **1997**, *71*(18), 2617–2619.

[61] Levy, M.; Osgood, R. M.; Liu, R.; Cross, L. E.; Cargill, G. S.; Kumar, A.; Bakhru, H. *Applied Physics Letters* **1998**, *73*(16), 2293–2295.

[62] Jette-Charbonneau, S.; Lahoud, N.; Charbonneau, R.; Mattiussi, G.; Berini, P. *IEEE Transactions on Advanced Packaging* **2008**, *31*(3), 479–483.

[63] Adhesive bonding — Wikipedia, The Free Encyclopedia. Wikipedia contributors. `https://en.wikipedia.org/w/index.php?title=Adhesive_bonding&oldid=869314286`, **2018**.

[64] Niklaus, F.; Andersson, H.; Enoksson, P.; Stemme, G. *Sensors and Actuators A: Physical* **2001**, *92*(1).

[65] Borrelli, N. F.; Grossman, D. G.; Mann, L. G.; Mordarski, J. M. *Corning Polarcors* **2010**.

[66] Dtsch, H.; Bahlmann, N.; Zhuromskyy, O.; Hammer, M.; Wilkens, L.; Gerhardt, R.; Hertel, P.; Popkov, A. F. *Journal of the Optical Society of America B* **2005**, *22*(1), 240–253.

[67] Dulal, P.; Block, A. D.; Gage, T. E.; Haldren, H. A.; Sung, S.-Y.; Hutchings, D. C.; Stadler, B. J. H. *ACS Photonics* **2016**, *3*(10), 1818–1825.

[68] El-Ganainy, R.; Eisfeld, A.; Levy, M.; Christodoulides, D. N. *Applied Physics Letters* **2013**, *103*(16), 161105.

[69] Hideki, Y.; Shun, I.; Yuki, U. *Japanese Journal of Applied Physics* **2010**, *49*(5R), 058002.

[70] Shoji, Y.; Ito, M.; Shirato, Y.; Mizumoto, T. *Optics Express* **2012**, *20*(16), 18440–18448.

[71] Sobu, Y.; Shoji, Y.; Sakurai, K.; Mizumoto, T. *Optics Express* **2013**, *21*(13), 15373–15381.

[72] Shui, K.; Nie, L.; Zhang, Y.; Peng, B.; Xie, J.; Deng, L.; Bi, L. *Optics Express* **2016**, *24*(12), 12856–12867.

[73] Pintus, P.; Huang, D.; Zhang, C.; Shoji, Y.; Mizumoto, T.; Bowers, J. E. *Journal of Lightwave Technology* **2017**, *35*(8), 1429–1437.

[74] Shiraishi, K.; Tajima, F.; Kawakami, S. *Optics Letters* **1986**, *11*(2), 82–84.

[75] Sun, L.; Jiang, S.; Zuegel, J. D.; Marciante, J. R. *Optics Letters* **2010**, *35*(5), 706–708.

[76] Shalaby, M.; Peccianti, M.; Ozturk, Y.; Morandotti, R. *Nature Communications* **2013**, *4*, 1558.

[77] Ishida, E.; Miura, K.; Shoji, Y.; Yokoi, H.; Mizumoto, T.; Nishiyama, N.; Arai, S. *Optics Express* **2017**, *25*(1), 452–462.

[78] Shen, Z.; Zhang, Y.-L.; Chen, Y.; Zou, C.-L.; Xiao, Y.-F.; Zou, X.-B.; Sun, F.-W.; Guo, G.-C.; Dong, C.-H. *Nature Photonics* **2016**, *10*, 657.

[79] Sounas, D. L.; Soric, J.; Al, A. *Nature Electronics* **2018**, *1*(2), 113–119.

[80] Shi, Y.; Yu, Z.; Fan, S. *Nature Photonics* **2015**, *9*, 388.

[81] Blanco-Redondo, A.; Andonegui, I.; Collins, M. J.; Harari, G.; Lumer, Y.; Rechtsman, M. C.; Eggleton, B. J.; Segev, M. *Physical Review Letters* **2016**, *116*(16), 163901.

[82] Kraus, Y. E.; Lahini, Y.; Ringel, Z.; Verbin, M.; Zilberberg, O. *Physical Review Letters* **2012**, *109*(10), 106402.

[83] Meier, E. J.; An, F. A.; Gadway, B. *Nature Communications* **2016**, *7*, 13986.

[84] Schomerus, H. *Optics Letters* **2013**, *38*(11), 1912–4.

[85] Wang, Z.; Chong, Y.; Joannopoulos, J. D.; Soljacic, M. *Nature* **2009**, *461*(7265), 772–5.

[86] Wang, Z.; Chong, Y. D.; Joannopoulos, J. D.; Soljacic, M. *Physical Review Letters* **2008**, *100*(1), 013905.

[87] Okamoto, K. *Fundamentals of Optical Waveguides (Second Edition);* Academic Press, 2006.

[88] Nishihara, H.; Haruna, M.; Suhara, T. *Optical Integrated Circuits;* McGraw-Hill, 1985.

[89] Liu, J. *Photonic Devices;* Cambridge University Press, 2005.

[90] Bi, L.; Hu, J.; Dionne, G. F.; Kimerling, L.; Ross, C. A. *Proc. SPIE 7941, Integrated Optics: Devices, Materials, and Technologies XV* **2011**.

[91] Shintaku, T.; Tate, A.; Mino, S. *Applied Physics Letters* **1997**, *71*(12), 1640–1642.

[92] Popkov, A. F.; Fehndrich, M.; Lohmeyer, M.; Dtsch, H. *Applied Physics Letters* **1998**, *72*(20), 2508–2510.

[93] Bahlmann, N.; Lohmeyer, M.; Dotsch, H.; Hertel, P. *IEEE Journal of Quantum Electronics* **1999**, *35*(2), 250–253.

[94] Wilkens, L.; Trger, D.; Dtsch, H.; Popkov, A. F.; Alekseev, A. M. *Applied Physics Letters* **2001**, *79*(26), 4292–4294.

[95] Zhang, W.; Mu, J.-W.; Huang, W.-P.; Zhao, W. *Applied Physics Letters* **2011**, *98*(17), 171109.

[96] Dotsch, H.; Hertel, P.; Luhrmann, B.; Sure, S.; Winkler, H. P.; Ye, M. *IEEE Transactions on Magnetics* **1992**, *28*(5), 2979–2984.

[97] Wettling, W.; Andlauer, B.; Koidl, P.; Schneider, J.; Tolksdorf, W. *physica status solidi (b)* **1973**, *59*(1), 63–70.

[98] Boudiar, T.; Payet-Gervy, B.; Blanc-Mignon, M.-F.; Rousseau, J.-J.; Berre, M. L.; Joisten, H. *Journal of Magnetism and Magnetic Materials* **2004**, *284*, 77 – 85.

[99] Sung, S.-Y.; Qi, X.; Stadler, B. J. H. *Applied Physics Letters* **2005**, *87*(12), 121111.

[100] Espinola, R. L.; Izuhara, T.; Tsai, M.-C.; Osgood, R. M.; Dtsch, H. *Optics Letters* **2004**, *29*(9), 941–943.

[101] Xin Zhou, You Wang, D. L.; Chong, Y. D. *New Journal of Physics* **2017**, *19*(095002).

[102] Hideki, Y.; Yuya, S.; Tetsuya, M. *Japanese Journal of Applied Physics* **2004**, *43*(8S), 5871.

[103] Wallenhorst, M.; Niemller, M.; Dtsch, H.; Hertel, P.; Gerhardt, R.; Gather, B. *Journal of Applied Physics* **1995**, *77*(7), 2902–2905.

[104] Levy, M.; Karki, D. *Scientific Reports* **2017**, *7*(39972).

[105] Bliokh, K. Y.; Nori, F. *Physical review A* **2012**, *85*, 061801.

[106] Kim, K.-Y.; Lee, I.-M.; Kim, J.; Jung, J.; Lee, B. *Physical Review A* **2012**, *86*, 063805.

[107] Banzer, P. *Journal of the european optical society - rapid publications* **2013**, *8*, 13032.

[108] Barnett, S. M. *Journal of Modern Optics* **2010**, *57*(14-15), 1339–1343.

[109] Friese, M. E. J.; Enger, J.; Rubinsztein-Dunlop, H.; Heckenberg, N. R. *Physical Review A* **1996**, *54*, 1593–1596.

[110] Rodrguez-Fortuo, F. J. *Science* **2013**, *340*, 328–330.

[111] Cai, X. *Science* **2012**, *338*, 363–366.

[112] Aiello, A.; Banzer, P.; Neugebauer, M.; Leuchs, G. *Nature Photonics* **2015**, *9*, 789–795.

[113] Bliokh, K. Y.; Bekshaev, A. Y.; Nori, F. *New Journal Of Physics* **2013**, *15*, 033026.

[114] Bliokh, K. Y.; Dressel, J.; Nori, F. *New Journal Of Physics* **2014**, *16*, 093037.

[115] Petersen, J.; Voltz, J.; Rauschenbeutel, A. *Science* **2014**, *346*, 67–71.

[116] Neugebauer, M.; Banzer, P.; Bauer, T.; Lindlein, N.; Aiello, A.; Marquardt, C.; Korger, J.; Leuchs, G. In *Conference on lasers nad electro-optics*. IEEE, 2012.

[117] Neugebauer, M.; Banzer, P.; Bauer, T.; Lindlein, N.; Aiello, A.; Marquardt, C.; Korger, J.; Leuchs, G. In *2012 Conference on Lasers and Electro-Optics (CLEO)*, pages 1–2, 2012.

[118] Barnett, S. M. *Physical Review Letters* **2010**, *104*, 070401.

[119] Holmes, B. M.; Hutchings, D. C. *Applied Physics Letters* **2006**, *88*, 061116.

[120] Hutchings, D. C. *Ieee Photonics Journal* **2013**, *5*, 6602512.

[121] He, H.; Friese, M. E.; Heckenberg, N. R.; Rubinsztein-Dunlop, H. *Physical Review letters* **1995**, *75*, 826–829.

[122] Simpson, N. B.; Allen, L.; Padgett, M. J. *Journal of Modern Optics* **1996**, *43*, 2485–2491.

[123] Frhapter, S.; Jesacher, A.; Bernet, S.; Ritsch-Marte, M. *Optics Express* **2005**, *13*, 689–694.

[124] Bouchal, Z.; Celechovsk, R. *New Journal of Physics* **2004**, *6*(1), 131.

[125] Mair, A.; Vaziri, A.; Weighs, G.; Zeilinger, A. *Nature* **2001**, *412*, 313–316.

Appendix A

Publications and presentations

Peer-reviewed Journal articles

1. **D. Karki**, V. Stenger, A. Polick, M. Levy, *"Thin-Film Magnet-less Faraday Rotators For Compact Heterogeneous Integrated Isolator"*, Journal of Applied Physics 121, 233101 (2017).

2. M. Levy, **D. Karki**, *"Nonreciprocal Transverse Photonic Spin and Magnetization-Induced Electromagnetic Spin-Orbit Couplin"*, Scientific Reports 7, 39972 (2017).

3. **D. Karki**, R. El-Gananiny, M. Levy, *"Towards High Performing Edge-State Optical Isolator"*, manuscript submitted- under review.

Oral presentations at international conferences

1. **D. Karki**, M. Levy, *"Magnetization-Induced Electromagnetic Spin-Orbit Coupling in Magneto-Optic Media"* Oral presentation, APS March Meeting (2017), Session L47.3.

2. **D. Karki**, V. Stenger, A. Pollick, and M. Levy, *"Thin-Film Magnetless Faraday Rotators for Heterogeneously Integrated On-Chip Optical Isolators"* in Conference on Lasers and Electro-Optics, OSA Technical Digest (online) (Optical Society of America, 2018), paper SF3J.5.

Appendix B

Copyrights and permissions

Permission for Fig. 2.1 and 2.2.

Dolendra Karki <dkarki@mtu.edu> Sun, Nov 25, 2018 at 6:47 PM
To: haichun@gmail.com

Dear Dr Yang,

I would like to use figures 1.1 (Operation principle of an isolator) and 1.4 (Arrangement of cations in a YIG formula unit) from your dissertation. I liked them and would like to reproduce in my PhD dissertation if you permit to do so.

I am looking forward to your reply.

Regards,
Dolendra Karki
Physics Dept., MTU

Haichun Yang <haichun@gmail.com> Mon, Nov 26, 2018 at 6:05 AM
To: Dolendra Karki <dkarki@mtu.edu>

Sure, please go ahead and good luck.

Thanks,
Haichun

Copyright permission from AIP publishing to reproduce contents of chapter 2.

AIP PUBLISHING LICENSE
TERMS AND CONDITIONS

Nov 19, 2018

This Agreement between Michigan Technological University -- Dolendra Karki ("You") and AIP Publishing ("AIP Publishing") consists of your license details and the terms and conditions provided by AIP Publishing and Copyright Clearance Center.

License Number	4472720962830
License date	Nov 19, 2018
Licensed Content Publisher	AIP Publishing
Licensed Content Publication	Journal of Applied Physics
Licensed Content Title	Thin-film magnetless Faraday rotators for compact heterogeneous integrated optical isolators
Licensed Content Author	Dolendra Karki, Vincent Stenger, Andrea Pollick, et al
Licensed Content Date	Jun 21, 2017
Licensed Content Volume	121
Licensed Content Issue	23
Type of Use	Thesis/Dissertation
Requestor type	Author (original article)
Format	Print and electronic
Portion	Excerpt (> 800 words)
Will you be translating?	No
Title of your thesis / dissertation	Magnetless and Topological Edge Mode-Based On-Chip Optical Isolators and Spin-Orbit Coupling in Magneto-Optic Media
Expected completion date	Dec 2018
Estimated size (number of pages)	120
Requestor Location	Michigan Technological University Department of physics, MTU 1400 Townsend Dr Fisher Hall 118 HOUGHTON, MI 49931 United States Attn: Dolendra Karki
Billing Type	Invoice
Billing Address	Michigan Technological University Department of physics, MTU 1400 Townsend Dr Fisher Hall 118 HOUGHTON, MI 49931 United States Attn: Dolendra Karki
Total	0.00 USD

Terms and Conditions

AIP Publishing -- Terms and Conditions: Permissions Uses

AIP Publishing hereby grants to you the non-exclusive right and license to use and/or distribute

Copyright permission and policy for contents of chapter 3.

DorothyDiFranco (APS)
Nov 20, 07:41 EST

Dear Dolendra,

Thank you for writing. Kindly refer to our Copyright FAQ located at https://journals.aps.org/copyrightFAQ.html, specifically:

Q) - "As the author of an APS-published article, may I include my article or a portion of my article in my thesis or dissertation?"

A) - "Yes, the author has the right to use the article or a portion of the article in a thesis or dissertation without requesting permission from APS, provided the bibliographic citation and the APS copyright credit line are given on the appropriate pages."

I hope this is helpful to you.

Sincerely,

Dorothy DiFranco
help@aps.org

License agreement and author copyright policy for contents of chapter 4.